Title

Investigations of the Isotopic Composition of Trace Gases in the Stratosphere and of the Quantum Dynamics of Non-adiabatic Atomic Collisions

Author

Garofalo, Lauren A.

Publication Date

2017

Peer reviewed|Thesis/dissertation

Investigations of the Isotopic Composition of Trace Gases in the Stratosphere and of the Quantum Dynamics of Non-adiabatic Atomic Collisions

by

Lauren Garofalo

A dissertation submitted in partial satisfaction of the

requirements for the degree of

Doctor of Philosophy

in

Chemistry

in the

Graduate Division

of the

University of California, Berkeley

Committee in charge:

Professor Kristie A. Boering, Chair
Professor Ronald C. Cohen
Professor Allen H. Goldstein

Spring 2017

Abstract

Investigations of the Isotopic Composition of Trace Gases in the Stratosphere and of the Quantum Dynamics of Non-adiabatic Atomic Collisions

by

Lauren Garofalo

Doctor of Philosophy in Chemistry

University of California, Berkeley

Professor Kristie A. Boering, Chair

Measurements and analysis of the mixing ratios and isotopic compositions of carbon dioxide (CO_2), nitrous oxide (N_2O), methane (CH_4), and molecular hydrogen (H_2) from whole air samples collected during several NASA suborbital missions are presented. In each case, the global annual mean net isotope flux from the stratosphere to the troposphere, estimated empirically using the correlation between measured isotopic composition and N_2O mixing ratio, is large enough to influence tropospheric isotopic compositions on hemispheric and potentially regional scales, and hence needs to be considered when making "top-down" inferences about the sources and sinks of the gas, including the impact of human activities, from isotope measurements at the surface. For CO_2, in particular, I present and analyze 150 new measurements of $\Delta^{14}C$ of CO_2 collected from aircraft missions in 1997, 2000, 2004, 2012, and 2013, including the first hemispheric-scale $^{14}CO_2$ vertical profiles that extend from the lower or middle troposphere into the lower stratosphere over a wide range of latitudes in the Northern Hemisphere for 2013. To within the uncertainties, the global annual mean net $^{14}CO_2$ fluxes, which are approximately half the global ^{14}C production rates, have not changed between 1997 and 2013, suggesting that stratospheric age spectra are wide enough to damp out variations in the cosmogenic ^{14}C production rate associated with the 11-year solar cycle. This apparent lack of dependence of measured stratospheric $^{14}CO_2$ on the solar cycle simplifies the application of stratospheric $^{14}CO_2$ measurements as a model diagnostic to better understand rates and features of the stratospheric circulation and how they may be shifting over time as climate changes; an acceleration of the stratospheric circulation is predicted by climate models but is not, as of yet, confirmed by observations such as mean ages derived from the time lag between tropospheric and stratospheric concentrations of the gases CO_2 and SF_6 which are increasing in the troposphere. Additionally, these empirical $^{14}CO_2$ isotope fluxes from the stratosphere to the troposphere are needed for carbon cycle studies. For $^{14}CO_2$, as well as for the stable isotope compositions of CO_2, N_2O, CH_4 and H_2, the global annual mean net isotope flux is large enough that stratospheric chemistry, which enriches each gas in its rare, heavy isotopes, and subsequent transport from the stratosphere to the troposphere can interfere with determining the magnitudes of natural and anthropogenic emissions of these gases from surface observations. Overall, the measurements and net isotope fluxes presented here provide much needed constraints on the

isotopic compositions of CO_2, N_2O, CH_4 and H_2 and the transport of these gases, necessary for studies that seek to (1) diagnose changes in the stratospheric circulation and residence times over time, (2) quantify sources and sinks in the biogeochemical cycles of these gases, and/or (3) interpret the large number of isotopic composition measurements made at Earth's surface (e.g., to infer regional and global fossil fuel emissions from $\Delta^{14}CO_2$).

In the field of reaction dynamics, the $O(^1D)$ + Xe electronic quenching reaction was investigated in a crossed beam experiment. Unexpected large-scale oscillations in the differential cross sections, whose shape and relative phase depend strongly on collision energy, were observed for the inelastic scattering products, $O(^3P)$ and Xe. Comparison of the experimental results with time-independent scattering calculations shows qualitatively that this behavior is caused by Stueckelberg interferences, for which the quantum phases of the multiple reaction pathways accessible during electronic quenching constructively and destructively interfere. This investigation into the quantum nature of $O(^1D) \rightarrow O(^3P)$ quenching by Xe provides sensitive new experimental constraints on the Xe–O potential energy curves and their couplings, as well as benchmarks for theoretical treatments of quantum scattering in general.

For my family

Table of Contents

List of figures

List of Tables

Acknowledgements

This dissertation is the product of the support of many people in my life. First, I express my sincerest gratitude to my adviser Professor Kristie Boering who guided me through this strange and wonderful world of atmospheric chemistry and chemical physics. Thank you for your dedication and your lessons in atmospheric science, instrumentation, writing, fostering relationships with colleagues, and many other things that have shaped me as a scientist and as a person. Thank you to the members of my committee, Professors Ronald Cohen and Allen Goldstein, for their thoughtful critiques of this work during my qualifying exam and dissertation. I also thank the collaborators who welcomed me into their labs to pursue science that I could not have done anywhere else – Dr. Thomas Guilderson at Lawrence Livermore National Laboratory and Professor Jr-Min Jim Lin at the Institute of Atomic and Molecular Sciences, Academia Sinica.

I wish to convey my appreciation for current and past members of the Boering group for their support, scientific and otherwise, during graduate school. I especially thank the previous members of our group who laid the foundations for my work by archiving the CO_2 samples and/or isotopic composition data that were used in this dissertation.

I dedicate this dissertation to my family, without whom I would not have been successful in completing this work. Thank you for cheering me on through my struggles and celebrating my triumphs with me over the last few years. I especially thank my parents, Karen and Ric Garofalo, for their unwavering support and encouragement. You have always been my greatest champions and I owe all my accomplishments to you. Lastly, I thank Ryan for his steadfastness and well-timed reminders to balance work with play throughout this difficult but rewarding journey of pursuing our doctorates.

Chapter 1

Introduction and overview

As concentrations of carbon dioxide (CO_2) and non-CO_2 greenhouse gases such as nitrous oxide (N_2O) and methane (CH_4) increase in Earth's atmosphere due to human activity [e.g., *Stocker et al.*, 2013], investigations of their effect on radiative transfer and atmospheric dynamics are important for understanding feedbacks on atmospheric composition and climate. In addition to concentrations, the isotopic compositions of these chemically and/or radiatively important gases can provide complementary and often uniquely mechanistic information that can be used to better predict how the atmospheric composition and/or the atmospheric circulation will change over time. For the trace gases CO_2, N_2O, CH_4, and molecular hydrogen (H_2), processes in the stratosphere – such as photolysis, oxidation, or interactions with thermal neutrons – result in enrichments of the rare, heavy isotopes (D, ^{13}C, ^{14}C, ^{15}N, ^{17}O, or ^{18}O) relative to the corresponding common, light isotopes (H, ^{12}C, ^{14}N, or ^{16}O) in a manner that is distinct from gases emitted at Earth's surface – for instance, those produced by microbial activity or fossil fuel combustion. The characteristic isotopic signatures imparted by stratospheric processes are retained as air returns to the troposphere where they are then altered by biogeochemical processes or simply diluted by mixing with isotopically light gases emitted at Earth's surface. Because the stratosphere makes up only 10% of Earth's atmosphere by mass, and because many of the molecular-level isotope effects in photochemical reactions important in the stratosphere had not yet been measured or predicted, the effect of stratospheric photochemistry and transport to the troposphere on the isotopic compositions of trace gases measured at the surface was often assumed to be negligible in early studies [e.g. *Fung et al.,* 1991]. However, measurements in the stratosphere itself – made possible by improvements of analytical techniques in the 1990s to allow measurements on small air samples [e.g., *Brand*, 1995] – and subsequent modeling and laboratory experiments over the past 20 years have begun to show that chemistry in the stratosphere and its subsequent transport to the troposphere can indeed affect isotopic compositions at the surface for CO_2 [e.g., *Boering et al.*, 2004; *Hoag et al.*, 2005], N_2O [e.g. *Rahn and Wahlen*, 1997; *McLinden et al.*, 2003; *Park et al.*, 2004], CH_4 [*McCarthy et al.*, 2001, 2003], and H_2 [e.g., *Rahn et al.*, 2003], and that the influence of the stratosphere may need to be taken into account when isotope measurements made at the surface are used to infer the magnitudes and distributions of anthropogenic emissions as well as natural sources and sinks of each of these gases.

In this dissertation, I describe the measurement and analysis of the isotopic compositions of several trace gases in the stratosphere and troposphere, including CO_2, N_2O, CH_4, and H_2, with particular focus on a time series of the radiocarbon (^{14}C) content of stratospheric CO_2. I show that, in each case, the global annual mean net isotope flux from the stratosphere to the troposphere can be empirically estimated from the correlation of the isotope measurements with simultaneous measurements of N_2O mixing ratios, combined with independent knowledge of the global N_2O loss rate, based on an understanding of the slope-equilibrium relationships of long-lived tracers in the stratosphere derived by *Plumb and Ko* [1992] and *Plumb* [2007]. In all cases, the fluxes are large enough to affect the isotopic composition of these gases at Earth's surface, thus resolving discrepancies between their isotope and concentration budgets, providing a new tracer of the biogeochemical cycling of the gas, and/or requiring the removal of the stratospheric

component of the isotope variations observed at the surface that may have been previously ignored. The annual mean net isotope fluxes presented and reviewed here are a critical first step in quantifying the influence of transport of stratospheric gases on surface isotope measurements. $^{14}CO_2$ is an inert tracer produced in the lower stratosphere and upper troposphere by galactic cosmic rays, and it is also sensitive to the features of the stratospheric circulation. I show that the net $\Delta^{14}CO_2$ fluxes I derive from measurements I made on samples collected between 1997 and 2013 by stratospheric aircraft – and thus the global $^{14}CO_2$ production rate (which is equal to twice the net $^{14}CO_2$ flux) – do not appear to be sensitive to the 11-year solar cycle in the penetration of cosmic rays into Earth's atmosphere that modulates the instantaneous ^{14}C production rate. Therefore, in addition to providing the net flux of $\Delta^{14}CO_2$ to the troposphere needed for carbon cycle and fossil fuel emission studies, this new time series of stratospheric $^{14}CO_2$ measurements can be more easily applied to diagnosing the rates and characteristics of the stratospheric circulation and how it may be changing as climate changes without the additional complexity of taking solar cycle variations in stratospheric $^{14}CO_2$ levels into account.

In addition to measurements and analysis of the isotopic compositions of stratospheric gases, I also performed crossed beam experiments at the Institute of Atomic and Molecular Sciences (IAMS) at Academia Sinica in Taipei, Taiwan. Several experiments were directed at investigating the underlying chemical physics of unusual isotope effects in ozone formation and the transfer of its anomalous "non-mass-dependent" ^{17}O and ^{18}O enrichments to CO_2, which is relevant for understanding isotopic measurements of stratospheric CO_2 (reviewed, e.g., in Chapter 3). The most fruitful of the experiments I performed at IAMS were crossed beam studies of the dynamics of the relaxation of oxygen in its first electronically excited state, $O(^1D)$, to the ground state, $O(^3P)$, by a noble gas, xenon (Xe). I discovered large and unexpected oscillations in the differential cross sections of the products $O(^3P)$ and Xe; comparison with high-level theoretical calculations revealed these to be a rarely observed quantum interference effect known as Stueckelberg oscillations [*Stueckelberg*, 1932]. In addition to their novelty, these Stueckelberg oscillations offer new experimental constraints on the Xe–O potential energy curves and their couplings, as well as new benchmarks for theoretical treatments of potential energy surfaces and quantum scattering in general.

An overview of the work presented in this dissertation is provided below, along with brief discussions of the results and how they advance their fields.

Chapter 2: Measurements of $^{14}CO_2$ in the stratosphere and free troposphere: Vertical profiles and empirical radiocarbon production rates

Recent work in our group that compared measured $\Delta^{14}CO_2$ from samples collected in the stratosphere to simulated $\Delta^{14}CO_2$ from a global 3D chemical transport model showed that stratospheric $\Delta^{14}CO_2$ is a sensitive and unique diagnostic of stratospheric transport and residence times [*Kanu et al.*, 2016]. Additionally, this work showed that the correlation between $\Delta^{14}CO_2$ and N_2O can be used to empirically estimate the global annual mean net $\Delta^{14}CO_2$ flux from the stratosphere to the troposphere, which is half the global $^{14}CO_2$ production rate by cosmic rays. Therefore, it was concluded that a time series of $\Delta^{14}CO_2$ observations may be useful in monitoring changes in the rate or shape of the stratospheric circulation with changing climate, as

has been predicted by chemistry-climate models [e.g., *Li et al.*, 2012; *Oberländer-Hayn et al.*, 2016]. Such a time series would also provide empirical cosmogenic $^{14}CO_2$ production rates which are needed for carbon cycle studies, including those that use $\Delta^{14}CO_2$ measurements at the surface to infer fossil fuel emissions on regional and global scales [e.g., *Randerson et al.*, 2002; *Levin et al.*, 2003, 2010, 2013; *Riley et al.*, 2008; *LaFranchi et al.*, 2013, 2016; *Graven*, 2015].

In Chapter 2, I present and analyze 150 new measurements of $\Delta^{14}CO_2$ from previously archived and newly collected samples from several NASA science missions spanning the years 1997 to 2013. These measurements, combined with the 54 measurements presented in *Kanu et al.* [2016], comprise the largest set of $\Delta^{14}CO_2$ measurements in the upper atmosphere since the stratosphere purged itself of the ^{14}C produced by atmospheric nuclear weapons testing in the mid-twentieth century. For this new time series, I found that the $^{14}CO_2$ production rates estimated from $\Delta^{14}CO_2$: N_2O correlations show no apparent sensitivity to the 11-year solar cycle, likely because the widths of stratospheric age spectra [e.g., *Andrews et al.*, 2001] are sufficiently large to dampen the sinusoidal variation in the instantaneous ^{14}C production rate associated with the attenuation of cosmic rays by solar activity [e.g., *Jöckel and Brenninkmeijer*, 2002]. This lack of dependence on the solar cycle reduces the complexity of using this new time series of stratospheric $\Delta^{14}CO_2$ measurements as a diagnostic for the rates and characteristics of the stratospheric circulation and how they may be changing over time. While chemistry-climate models predict that an increase in the strength of the stratospheric circulation has already occurred due to ozone depletion and increased radiative forcing [e.g., *Li et al.*, 2008; *Oberländer-Hayn et al.*, 2016], some stratospheric observations, such as mean ages estimated from the time lag of CO_2 and SF_6 measurements in the stratosphere and troposphere [*Engel et al.*, 2009] show no detectable trend. Additional measurements that provide insight into various aspects of the stratospheric circulation are still sparse and yield apparently conflicting interpretations – for example, temperatures [e.g., *Fu et al.*, 2015 vs. *Osso et al.*, 2015], water vapor trends [e.g., *Randel et al.*, 2006 vs. *Wang and Waugh*, 2012], and relationships between other long-lived tracers [e.g., *Ray et al.*, 2010 vs. *Bonisch et al.*, 2011]. Thus, additional constraints from $\Delta^{14}CO_2$ observations are needed to resolve the discrepancies between models and observations and between different observational data that may be sensitive to specific aspects of the stratospheric circulation. A more robust understanding of the stratospheric circulation and its evolution in time will improve predictions of the timing of the recovery of the Antarctic Ozone Hole as well as potential feedbacks between climate and air quality (e.g., transport of stratospheric ozone to the troposphere) [*Butchart*, 2014, and references within].

This large new dataset of $\Delta^{14}CO_2$ measurements also provides an unprecedented 'snapshot' of the vertical distribution of $\Delta^{14}CO_2$ from the mid-troposphere to the lower stratosphere as measured across a wide range of latitudes in the Northern Hemisphere in Summer 2013. These vertical profiles provide important constraints for inverse modeling studies that seek to quantify carbon partitioning between the atmosphere, biosphere and oceans, as well as to infer regional and global fossil fuel emissions from measurements of $\Delta^{14}CO_2$ at the surface in the Northern Hemisphere [e.g., *Basu et al.*, 2016]. In addition to observing the general trends across the Northern Hemisphere in Summer 2013 and from a single vertical profile in Summer 2012 at 35°N, I investigate the origin of significant outliers in two $\Delta^{14}CO_2$ vertical profiles. These outliers yield insights into the influences of long-range transport of air that recently entered the stratosphere in the Asian Monsoon and of short-range convective transport from the surface to

the upper troposphere on the atmospheric composition of the upper troposphere and lower stratosphere (UT/LS). While features of these variations in the origin of air are subtly represented in measurements of other trace gases from these aircraft missions (e.g., O_3, CO, and various hydrocarbons), the deviations in $\Delta^{14}CO_2$ were so large that they could not be overlooked and thus motivated the further investigations presented here.

Chapter 3: The effects of stratospheric chemistry and transport on the isotopic compositions of long-lived gases measured at Earth's surface

Quantitative and mechanistic understanding of the sources and sinks of CO_2 and of other chemically and/or radiatively important gases like CH_4, H_2, and N_2O is needed to understand and predict the magnitudes of climate feedbacks and to inform and facilitate possible mitigation strategies to minimize future emissions. Isotope measurements continue to be an integral part of the efforts to gain a better mechanistic understanding of the sources and sinks of these gases. As noted above, it is now known that various processes in the stratosphere enrich the rare, heavy isotopes in these gases. Transport of these highly enriched gases from the stratosphere to the troposphere, even after dilution with isotopically lighter tropospheric air, can influence surface isotopic compositions and interfere with using surface measurements to infer, for example, the relative magnitudes of natural versus anthropogenic sources of these gases. In Chapter 3, I generalize the method of estimating the global annual mean net isotope fluxes for $\Delta^{14}CO_2$ presented in Chapter 2 to a number of other isotopic species, including δD and $\delta^{13}C$ of CH_4, δD of H_2, $\delta^{18}O$ and $\Delta^{17}O$ of CO_2, and $\delta^{15}N$ and $\delta^{18}O$ of N_2O, and provide evidence that the stratospheric influence on the isotopic compositions of these gases measured at Earth's surface is large enough to warrant consideration in studies that seek to understand the sources and sinks of these gases from surface isotope measurements.

The global annual mean net isotope fluxes from the stratosphere to the troposphere are estimated by exploiting the compact relationship that is known to exist between measurements of any two species in the stratosphere that are long-lived with respect to stratospheric transport – the slope of which is equal to the ratio of their net vertical fluxes [*Plumb and Ko*, 1992; *Plumb*, 2007]. Therefore, with independent knowledge of the net vertical flux of N_2O (which is simply the global N_2O loss rate since 99% of N_2O loss occurs in the stratosphere [*Minschwaner et al.*, 1993]), the net flux of any long-lived tracer can be estimated based on the observed tracer:N_2O slope. This slope-equilibrium approach has been applied to estimating net vertical fluxes of O_3 [*Murphy and Fahey*, 1994; *Olsen et al.*, 2002], NO_y [*Fahey et al.*, 1995], and meteoritic material [*Cziczo et al.*, 2001], as well as the ^{17}O anomaly in CO_2 [*Luz et al.*, 1999; *Boering et al.*, 2004] and N_2O isotopologues [*Park et al.*, 2004]. In this chapter, I reanalyze and synthesize estimates of the global annual mean net isotope fluxes from both new and previously published isotope measurements for CH_4, H_2, CO_2, and N_2O. I update previously reported values based on advances in understanding and compare them to estimates from studies by other research groups, when available. As outlined below, the stratospheric influence is large enough to be detectable at the surface in each case.

Stratospheric CH_4 is highly enriched in ^{13}C and D due to kinetic isotope effects (KIEs) in the oxidation of CH_4 by OH, $O(^1D)$, and Cl atoms [*McCarthy et al.*, 2003; *Rice et al.*, 2003;

Röckmann et al., 2011]. The estimates of the net isotope fluxes from the stratosphere to the troposphere for $\delta^{13}C–CH_4$ and $\delta D–CH_4$ are large enough that, even at steady-state and assuming complete dilution in the troposphere, the perturbation to the tropospheric isotopic compositions are as large as the observed interhemispheric gradients (0.5‰ for $\delta^{13}C–CH_4$ and 10‰ for $\delta D–CH_4$ [*Quay et al.*, 1999]) and the amplitude of the seasonal variation (0.4‰ for $\delta^{13}C–CH_4$ at 60°N [*Quay et al.*, 1999]). Because the interhemispheric gradients and magnitudes and phases of the seasonal cycles are important constraints for 3D models [e.g., *Fung et al.*, 1991; *Hein et al.*, 1997], the stratospheric influence may also need to be considered in global models of methane and its isotopic composition [e.g., *Houweling et al.*, 2017].

Molecular H_2 in the stratosphere is enormously enriched in D due to KIEs in both its source (oxidation of CH_4 to CH_2O followed by photolysis to H_2) and sink (oxidation of H_2 by OH) reactions there [e.g., *Rahn et al.*, 2003]. Similar to the case for the net isotope fluxes of isotopically enriched stratospheric CH_4 to the troposphere, the net flux of δD of H_2 to the troposphere is large enough that, even at steady-state and assuming complete dilution in the troposphere, the perturbation to the troposphere is also as large as the observed interhemispheric gradient in $\delta D–H_2$ of 15‰ [*Gerst and Quay*, 2000].

Stratospheric CO_2 is non-mass-dependently enriched in ^{17}O and ^{18}O [e.g., *Brenninkmeijer et al.*, 1995; *Thiemens et al.*, 1995; *Lammerzahl et al.*, 2002; *Boering et al.*, 2004] due to photochemical transfer of the large and unusual non-mass-dependent KIEs in the ozone formation reaction ($O + O_2 + M \rightarrow O_3$) via isotope exchange between CO_2 and $O(^1D)$ that is produced by O_3 photolysis [e.g., *Yung et al.*, 1997; *Wiegel et al.*, 2013]. For $\delta^{18}O$ of CO_2, the net isotope flux to the troposphere is large enough to include in global models that use measurements of $\delta^{18}O$ of tropospheric CO_2 to estimate gross primary productivity [e.g., *Cuntz*, 2003]. For the ^{17}O anomaly in CO_2 (defined as $\Delta^{17}O = \delta^{17}O – \lambda_{MD} \cdot \delta^{18}O$, where λ_{MD} is the mass dependent relationship ~0.5), the net isotope flux to the troposphere is large enough to sustain a non-zero ^{17}O anomaly in tropospheric CO_2 before the ^{17}O anomaly is completely destroyed by equilibration with liquid water in the leaves of plants while their stomata are open and they are fixing carbon [e.g., *Hoag et al.*, 2005; *Barkan and Luz*, 2012; *Hofmann et al.*, 2016]. In fact, the balance between the stratospheric input and the destruction by the biosphere of the ^{17}O anomaly of CO_2 has been proposed as a tracer of the gross carbon uptake by the biosphere that is independent of the $\delta^{18}O$ of precipitation and leaf water if the net isotope flux from the stratosphere is well-defined [*Hoag et al.*, 2005].

Stratospheric CO_2 is also enriched in ^{14}C due to *in situ* production of radiocarbon by thermal neutrons produced by cosmic rays in the stratosphere and upper troposphere [e.g., *Dutta*, 2016]. I include my results from Chapter 2 in the review in Chapter 3 for completeness, and note the importance of the apparent insensitivity of the net $\Delta^{14}CO_2$ fluxes for a time period that spans ~1.5 solar cycles. These empirical net $\Delta^{14}CO_2$ fluxes will benefit carbon cycle studies, especially now that the natural cosmogenic ^{14}C production rate, and the rates and details of $^{14}CO_2$ transport to the troposphere, are playing an increasingly important role relative to the bomb ^{14}C input in studies of surface $^{14}CO_2$ and its redistribution there [*Randerson et al.*, 2002; *Levin et al.*, 2010] and the use of surface or tower observations to infer regional anthropogenic emissions [e.g., *Riley et al.*, 2008; *Graven et al.*, 2012;

LaFranchi et al., 2013; *Beramendi-Orosco et al.*, 2015; *Graven*, 2015].

Stratospheric N_2O is enriched in ^{15}N and ^{18}O [e.g., *Kim and Craig*, 1993; *Rahn and Wahlen*, 1997; *Toyoda et al.*, 2001; *Röckmann et al.*, 2003; *Park et al.*, 2004]. Laboratory experiments and theoretical calculations [e.g., *Kaiser et al.*, 2002; *Röckmann et al.*, 2003; *Yung et al.*, 2004; *Schmidt et al.*, 2011] have shown that photolysis in the stratosphere – N_2O's primary sink – enriches the remaining N_2O in both ^{15}N and ^{18}O; the tails of the UV absorption cross-sections for the heavy isotopologues ($^{15}N^{14}N^{16}O$, $^{14}N^{15}N^{16}O$, $^{14}N^{14}N^{18}O$) are blue-shifted slightly out of the solar window for N_2O photolysis in the stratosphere relative to the light isotopologue ($^{14}N^{14}N^{16}O$). Indeed, Kim and Craig [1993] used isotope measurements on two archived stratospheric air samples to first suggest that large isotope effects in the stratospheric sink could balance the isotopically light sources to yield the measured isotopic composition of N_2O in the troposphere. The relatively extensive stratospheric observations (referenced above) and quite remarkable agreement with global models [*McLinden et al.*, 2003], including agreement between the net isotope fluxes using the empirical slope-equilibrium approach and the model predictions, means that uncertainties in the sources of N_2O remain the larger uncertainty in the global N_2O budget rather the stratospheric sink, at least on annual time scales.

Thus, for each isotopic species, even if the annual mean net isotope flux from the stratosphere to the troposphere is small compared to other components of the isotope budget, it may not be negligible as previously assumed.

Furthermore, there is now evidence that seasonal and interannual variations at the surface caused by transport from the stratosphere can be much larger than predicted based on simple two-box model dilutions of the global annual mean net isotope flux from the stratosphere into the whole troposphere. For example, annual cycles in the ^{15}N and ^{18}O isotopic compositions of N_2O were measured on archived air collected at Cape Grim Tasmania between 1978 and 2005 [*Park et al.*, 2012] which show the influence of both stratospheric air and ocean upwelling. A large deviation in the ^{15}N isotopic composition was also detected in this Cape Grim dataset during the large El Niño – Southern Oscillation (ENSO) event in 1997–1998, although it was not yet clear if this excursion was driven by changes in ocean upwelling, biomass burning, stratosphere-troposphere exchange (STE) or variations in tropospheric transport [*Park et al.*, 2012]. Thiemens *et al.* [2014] also observed a large deviation in $\Delta^{17}O$ of CO_2 during 1997–1998 in a decade-long time series of measurements at La Jolla, California; they argue that this variation during ENSO was due to enhanced primary productivity but might also be an effect of an ENSO-driven change in STE. Hofmann *et al.*[2016] observed a seasonal cycle in $\Delta^{17}O$ of CO_2 measured in Gottingen, Germany that may be due to the seasonality of STE, fossil fuel burning, or biosphere activity. From these recent observations, it is clear that stratospheric signals (or potentially stratospheric signals) – beyond an annual average signal mixed from the stratosphere into the troposphere – need to be taken into account when isotope measurements at the surface are used to infer local or regional sources of the gases of interest. This accounting for the possible influence of the stratosphere on sub-annual and interannual timescales will require 3D modeling efforts. Such modeling efforts could range from full 3D chemical-transport models (whose annual mean net isotope fluxes from the stratosphere to the troposphere could be directly checked against the values in Chapter 3) to applying "tropospheric mean ages" calculated from a 3D chemical

transport model that are convolved with the empirical net isotope fluxes in Chapter 3 (without having to model the stratospheric isotope compositions themselves).

Finally, I note that quantifying the effect of stratospheric chemistry and transport on measurements at Earth's surface is also of interest for tropospheric ozone. Given both the similarities and differences between ozone and the isotopic compositions of long-lived gases transported from the stratosphere, modeling the influence of the stratosphere on the isotopic compositions of these long-lived gases with distinct stratospheric signals at Earth's surface could aid in separating the stratospheric sources of ozone from its tropospheric sources at a given location for which isotope measurements also exist – in a complementary effort to the extensive modeling and observational studies of stratospheric and tropospheric ozone [e.g., *Hess and Zbinden*, 2013; *Hsu and Prather*, 2014; *Orbe et al.*, 2014; *Yang et al.*, 2016] and other chemical or aerosol tracers [e.g., *Simmonds et al.*, 2013; *Liu et al.*, 2016].

Chapter 4: Electronic quenching of $O(^1D)$ by Xe: Oscillations in the product angular distribution and their dependence on collision energy

In the final chapter of this dissertation, I explore the scattering dynamics of the electronic relaxation of $O(^1D)$ to $O(^3P)$ upon collision with Xe, as investigated in a crossed molecular beam apparatus. These experiments reveal the quantum nature of this non-adiabatic reaction and provide important new constraints on the potential energy curves associated with this reaction as well as benchmarks for theoretical predictions of quantum scattering. Before focusing on the Xe–$O(^1D)$ system, I also participated in experiments to study oxygen atom exchange in the reactions $^{16}O(^3P) + {}^{18}O_2 \rightarrow {}^{18}O(^3P) + {}^{16}O_2$ and $^{18}O(^1D) + C^{16}O \rightarrow {}^{16}O(^3P \text{ or } {}^1D) + C^{18}O$, which have applications for understanding the anomalous non-mass-dependent oxygen isotopic compositions of ozone, stratospheric CO_2, and other oxygen-containing gases in the atmosphere.

For the $^{16}O(^3P) + {}^{18}O_2 \rightarrow {}^{18}O(^3P) + {}^{16}O_2$ reaction, I note that the isotope exchange reaction $^xO(^3P) + {}^yO^zO \rightarrow {}^yO + {}^xO^zO$ occurs on the same potential energy surface as that of ozone formation, for which there are known but still not completely understood large and unusual kinetic isotope effects [e.g., *Gao and Marcus*, 2002; *Mauersberger et al.*, 2005; *Schinke and Fleurat-Lessard*, 2005; *Ivanov and Babikov*, 2013], and for which previous work in our group revealed non-statistical dynamics [*Van Wyngarden et al.*, 2007, 2014]. While Van Wyngarden *et al.* measured the heavy + light-light isotope reaction ($^{18}O(^3P) + {}^{16}O_2 \rightarrow {}^{16}O(^3P) + {}^{18}O^{16}O$), I measured the scattering dynamics of the light + heavy-heavy reaction ($^{16}O(^3P) + {}^{18}O_2 \rightarrow {}^{18}O(^3P) + {}^{16}O_2$) for which the unusually large zero-point-energy isotope effects are the largest (albeit the ones that cancel out in 'isotopically scrambled' systems in bulk photochemistry experiments and the atmosphere [*Gao and Marcus*, 2001; *Feilberg et al.*, 2013].) At the high collision energies that were accessible in the experiment, however, which were limited to energies higher than 5 kcal/mol due to the O atom source from O_2 photolysis at 157 nm and the geometry of the apparatus, the differences in the scattering dynamics for these two isotopically distinct reactions were too small to interpret; nevertheless, the experimental data and its analysis are likely to be used in future comparisons between theory and experiment for this system.

I also participated in the investigation of the dynamics of the oxygen isotope exchange reactions of $O(^1D)$ and $O(^3P)$ with CO [*Estillore et al.*, 2014]. These crossed beam studies were pursued in part to address whether the three-body reaction $O(^3P) + CO + M \rightarrow CO_2$ might produce unusual non-mass-dependent enrichments in CO_2, analogous to those in the three-body ozone formation reaction, as has been argued by Bhattacharya and co-workers to explain the ^{17}O anomaly in CO_2 formed in bulk photochemistry experiments by irradiating CO in the presence of O_2 [*Bhattacharya and Thiemens*, 1989; *Pandey and Bhattacharya*, 2006]. While the dynamics of the O + CO isotope exchange reaction do show some non-statistical behavior in our crossed beam experiments, photochemical kinetics modeling shows that the ^{17}O anomaly in CO_2 in the previous bulk photochemistry experiments can be attributed to ozone formation and subsequent photochemical transfer of oxygen isotopes from O_3 to CO_2 and does not require invoking dynamically-driven non-mass-dependent isotope effects in the $O + CO + M \rightarrow CO_2$ reaction [*Estillore et al.*, 2014].

While preparing for the $O + O_2$ and O + CO crossed beam experiments described above, I serendipitously discovered a quantum scattering effect in the electronic quenching reaction $O(^1D) + Xe \rightarrow O(^3P) + Xe$. As described in Chapter 4, I observed, unexpectedly and for the first time for this system, broad oscillations in the differential cross sections of the inelastically scattered products $O(^3P)$ and Xe, whose shape and relative phase varied dramatically with collision energy. With the help of theoretical calculations, these unusual differential cross sections were attributed to Stueckelberg interferences, a dynamical effect for which the quantum phases of the multiple reaction pathways accessible during a reaction constructively and destructively interfere to produce oscillatory structure in the differential cross section [*Stueckelberg*, 1932]. For the electronic relaxation of $O(^1D)$ by Xe, these interferences occur between the quantum phases of two available reaction pathways on the Xe–O potential energy curves – one in which the curve crossing occurs as the atoms approach and the other as the atoms separate – to produce the oscillations observed in these experiments. Discrepancies between the experimental results and theoretical predictions show how exquisitely sensitive this quantum dynamical effect is to both the subtle details of the underlying potential energy curves, especially in the curve crossing region, as well as to the treatment of collision energy in these calculations. Thus, these new experiments on the electronic quenching of $O(^1D)$ by Xe, and their comparison with theory, provide additional insight and important new constraints on the characteristics of the Xe–O potential energy curves and their couplings as well as new targets for theoretical calculations of potential energy surfaces and quantum scattering in general.

References

Andrews, A. E. et al. (2001), Mean ages of stratospheric air derived from in situ observations of CO_2, CH_4, and N_2O, *J. Geophys. Res.*, *106*(D23), 32295–32314, doi:10.1029/2001JD000465.

Barkan, E., and B. Luz (2012), High-precision measurements of $^{17}O/^{16}O$ and $^{18}O/^{16}O$ ratios in CO_2, *Rapid Commun. Mass Spectrom.*, *26*, 2733–2738, doi:10.1002/rcm.6400.

Basu, S., J. B. Miller, and S. Lehman (2016), Separation of biospheric and fossil fuel fluxes of CO_2 by atmospheric inversion of CO_2 and $^{14}CO_2$ measurements: Observation System Simulations, *Atmos. Chem. Phys.*, *16*, 5665–5683, doi:10.5194/acp-16-5665-2016.

Beramendi-Orosco, L., G. Gonzalez-Hernandez, A. Martinez-Jurado, A. Martinez-Reyes, A. Garcia-Samano, J. Villanueva-Diaz, F. J. Santos-Arevalo, I. Gomez-Martinez, and O. Amador-Muñoz (2015), Temporal and Spatial Variations of Atmospheric Radiocarbon in the Mexico City Metropolitan Area, *Radiocarbon*, *57*(3), 363–375, doi:10.2458/azu_rc.57.18360.

Bhattacharya, S. K., and M. H. Thiemens (1989), New Evidence for Symmetry Dependent Isotope Effects - O+CO Reaction, *Zeitschrift Fur Naturforsch. Sect. A-A, J. Phys. Sci.*, *44*, 435–444.

Boering, K. A., T. Jackson, K. J. Hoag, A. S. Cole, M. J. Perri, M. Thiemens, and E. Atlas (2004), Observations of the anomalous oxygen isotopic composition of carbon dioxide in the lower stratosphere and the flux of the anomaly to the troposphere, *Geophys. Res. Lett.*, *31*, L03109, doi:10.1029/2003GL018451.

Bönisch, H., A. Engel, T. Birner, P. Hoor, D. W. Tarasick, and E. . Ray (2011), On the structural changes in the Brewer-Dobson circulation after 2000, *Atmos. Chem. Phys.*, *11*(8), 3937–3948, doi:10.5194/acp-11-3937-2011.

Brand, W. A. (1995), PreCon: A Fully Automated Interface for the Pre-GC Concentration of Trace Gases on Air for Isotopic Analysis, *Isotopes Environ. Health Stud.*, *31*, 277–284, doi:10.1080/10256019508036271.

Brenninkmeijer, C. A. M., D. C. Lowe, M. R. Manning, R. J. Sparks, and P. F. J. van Velthoven (1995), The ^{13}C, ^{14}C, and ^{18}O isotopic composition of CO, CH_4, and CO_2 in the higher southern latitudes lower stratosphere, *J. Geophys. Res.*, *100*(D12), 26163–26172.

Butchart, N. (2014), The Brewer–Dobson circulation, *Rev. Geophys*, *52*, 157–184, doi:10.1002/2013RG000448.

Cuntz, M., P. Ciais, G. Hoffmann, and W. Knorr (2003), A comprehensive global three-dimensional model of $\delta^{18}O$ in atmospheric CO_2 : 1. Validation of surface processes, *J. Geophys. Res.*, *108*(D17), 4527, doi:10.1029/2002JD003153.

Cziczo, D. J., D. S. Thomson, and D. M. Murphy (2001), Ablation, flux, and atmospheric implications of meteors inferred from stratospheric aerosol., *Science*, *291*, 1772–1775, doi:10.1126/science.1057737.

Dutta, K. (2016), Sun, Ocean, Nuclear Bombs, and Fossil Fuels: Radiocarbon Variations and Implications for High-Resolution Dating, *Annu. Rev. Earth Planet. Sci.*, *44*, 239–275, doi:10.1146/annurev-earth-060115-012333.

Engel, A. et al. (2009), Age of stratospheric air unchanged within uncertainties over the past 30 years, *Nat. Geosci.*, *2*, 28–31, doi:10.1038/ngeo388.

Estillore, A. D., B. Jin, C.-P. Huang, L. Garofalo, M. Smith, Y. T. Lee, J.-J. Lin, and K. A. Boering (2014), Dynamics of the $^{18}O(^1D) + C^{16}O$ reaction by crossed beam methods and implications for non-mass-dependent oxygen isotope effects in bulk photochemistry experiments, in *248th ACS National Meeting*, San Francisco, California.

Fahey, D. W. et al. (1995), Emission Measurements of the Concorde Supersonic Aircraft in the Lower Stratosphere, *Science*, *270*(5233), 70–74, doi:10.1126/science.270.5233.70.

Feilberg, K. L., A. A. Wiegel, and K. A. Boering (2013), Probing the unusual isotope effects in ozone formation: Bath gas and pressure dependence of the non-mass-dependent isotope enrichments in ozone, *Chem. Phys. Lett.*, *556*, 1–8, doi:10.1016/j.cplett.2012.10.038.

Fu, Q., P. Lin, S. Solomon, and D. L. Hartmann (2015), Observational evidence of strengthening of the

Brewer-Dobson circulation since 1980, *J. Geophys. Res. Atmos.*, *120*, 10214–10228, doi:10.1002/2015JD023657.
Fung, I., J. John, J. Lerner, E. Matthews, M. Prather, L. P. Steele, and P. J. Fraser (1991), Three-Dimensional Model Synthesis of the Global Methane Cycle, *J. Geophys. Res.*, *96*(D7), 13033–13065, doi:10.1029/91jd01247.
Gao, Y. Q., and R. A. Marcus (2001), Strange and unconventional isotope effects in ozone formation, *Science*, *293*, 259–263, doi:10.1126/science.1058528.
Gao, Y. Q., and R. A. Marcus (2002), On the theory of the strange and unconventional isotopic effects in ozone formation, *J. Chem. Phys.*, *116*, 137–154, doi:10.1063/1.1415448.
Gerst, S., and P. Quay (2000), The deuterium content of atmospheric molecular hydrogen: Method and initial measurements, *J. Geophys. Res.*, *105*(D21), 26433–26445, doi:10.1029/2000JD900387.
Graven, H. D. (2015), Impact of fossil fuel emissions on atmospheric radiocarbon and various applications of radiocarbon over this century, *PNAS*, *112*(31), 9542–9545, doi:10.1073/pnas.1504467112.
Graven, H. D., T. P. Guilderson, and R. F. Keeling (2012), Observations of radiocarbon in CO_2 at La Jolla, California, USA 1992-2007: Analysis of the long-term trend, *J. Geophys. Res.*, *117*, D02302, doi:10.1029/2011JD016533.
Hess, P. G., and R. Zbinden (2013), Stratospheric impact on tropospheric ozone variability and trends: 1990-2009, *Atmos. Chem. Phys.*, *13*, 649–674, doi:10.5194/acp-13-649-2013.
Hoag, K. J., C. J. Still, I. Y. Fung, and K. A. Boering (2005), Triple oxygen isotope composition of tropospheric carbon dioxide as a tracer of terrestrial gross carbon fluxes, *Geophys. Res. Lett.*, *32*, L02802, doi:10.1029/2004GL021011.
Hofmann, M. E. G., B. Horváth, L. Schneider, W. Peters, K. Schützenmeister, and A. Pack (2016), Atmospheric measurements of $\Delta^{17}O$ in CO_2 in Göttingen, Germany reveal a seasonal cycle driven by biospheric uptake, *Geochim. Cosmochim. Acta*, *199*, 143–163, doi:10.1016/j.gca.2016.11.019.
Houweling, S., P. Bergamaschi, F. Chevallier, M. Heimann, T. Kaminski, M. Krol, A. M. Michalak, and P. Patra (2017), Global inverse modeling of CH_4 sources and sinks: An overview of methods, *Atmos. Chem. Phys. Discuss.*, *17*, 256–256, doi:10.5194/acp-17-235-2017.
Hsu, J., and M. J. Prather (2014), Is the residual vertical velocity a good proxy for stratosphere-troposphere exchange of ozone?, *Geophys. Res. Lett.*, *41*, 9024–9032, doi:10.1002/2014GL061994.
Ivanov, M. V, and D. Babikov (2013), On molecular origin of mass-independent fractionation of oxygen isotopes in the ozone forming recombination reaction, *PNAS*, *110*, 17708–17713, doi:10.1073/pnas.1215464110.
Jöckel, P., and C. A. M. Brenninkmeijer (2002), The seasonal cycle of cosmogenic ^{14}CO at the surface level: A solar cycle adjusted, zonal-average climatology based on observations, *J. Geophys. Res.*, *107*(D22), 4656, doi:10.1029/2001JD001104.
Kaiser, J., T. Röckmann, and C. A. M. Brenninkmeijer (2002), Temperature dependence of isotope fractionation in N_2O photolysis, *Phys. Chem. Chem. Phys.*, *4*, 4420–4430, doi:10.1039/b204837j.
Kanu, A. M., L. L. Comfort, T. P. Guilderson, P. J. Cameron-Smith, D. J. Bergmann, E. . Atlas, S. Schauffler, and K. A. Boering (2016), Measurements and modeling of contemporary radiocarbon in the stratosphere, *Geophys. Res. Lett.*, *43*(3), 1399–1406, doi:10.1002/2013GL058740.
Kim, K.-R., and H. Craig (1993), Nitrogen-15 and Oxygen-18 Characteristics of Nitrous Oxide: A Global Perspective, *Science*, *262*(5141), 1855–1857.
LaFranchi, B. W. et al. (2013), Constraints on emissions of carbon monoxide, methane, and a suite of hydrocarbons in the Colorado Front Range using observations of $^{14}CO_2$, *Atmos. Chem. Phys.*, *13*, 11101–11120, doi:10.5194/acp-13-11101-2013.
LaFranchi, B. W. et al. (2016), Strong regional atmospheric ^{14}C signature of respired CO_2 observed from a tall tower over the midwestern United States, *J. Geophys. Res. Biogeosciences*, *121*, 2275–2295, doi:10.1002/2015JG003271.
Lämmerzahl, P., T. Röckmann, C. A. M. Brenninkmeijer, D. Krankowsky, and K. Mauersberger (2002), Oxygen isotope composition of stratospheric carbon dioxide, *Geophys. Res. Lett.*, *29*(12), 1582,

doi:10.1029/2001GL014343.
Levin, I., B. Kromer, M. Schmidt, and H. Sartorius (2003), A novel approach for independent budgeting of fossil fuel CO_2 over Europe by $^{14}CO_2$ observations, *Geophys. Res. Lett.*, *30*(23), 2194, doi:10.1029/2003GL018477.
Levin, I., T. Naegler, B. Kromer, M. Diehl, R. J. Francey, A. J. Gomez-Pelaez, L. P. Steele, D. Wagenbach, R. Weller, and D. E. Worthy (2010), Observations and modelling of the global distribution and long-term trend of atmospheric $^{14}CO_2$, *Tellus*, *62B*, 26–46, doi:10.1111/j.1600-0889.2009.00446.x.
Levin, I., B. Kromer, and S. Hammer (2013), Atmospheric $\Delta^{14}CO_2$ trend in Western European background air from 2000 to 2012, *Tellus B*, *65*, 20092, doi:10.3402/tellusb.v65i0.20092.
Li, F., J. Austin, and J. Wilson (2008), The strength of the Brewer-Dobson circulation in a changing climate: Coupled chemistry-climate model simulations, *J. Clim.*, *21*, 40–57, doi:10.1175/2007JCLI1663.1.
Li, F., D. W. Waugh, A. R. Douglass, P. A. Newman, S. E. Strahan, J. Ma, J. E. Nielsen, and Q. Liang (2012), Long-term changes in stratospheric age spectra in the 21st century in the Goddard earth observing system chemistry-climate model (GEOSCCM), *J. Geophys. Res. Atmos.*, *117*, D20119, doi:10.1029/2012JD017905.
Linz, M., R. A. Plumb, E. P. Gerber, and A. Sheshadri (2016), The relationship between age of air and the diabatic circulation of the stratosphere, *J. Atmos. Sci.*, *73*, 4507–4518, doi:10.1175/JAS-D-16-0125.1.
Liu, H. et al. (2016), Using beryllium-7 to assess cross-tropopause transport in global models, *Atmos. Chem. Phys.*, *16*, 4641–4659, doi:10.5194/acp-16-4641-2016.
Luz, B., E. Barkan, M. L. Bender, M. H. Thiemens, and K. A. Boering (1999), Triple-isotope composition of atmospheric oxygen as a tracer of biosphere productivity, *Nature*, *400*, 547–550, doi:10.1038/22987.
Mauersberger, K., D. Krankowsky, C. Janssen, and R. Schinke (2005), Assessment of the ozone isotope effect, in *Advances in Atomic, Molecular, and Optical Physics,* eds by B. Bederson and H. Walther (Elseview Academic, San Diego) Vol 50, pp. 1–54.
McCarthy, M. C., P. Connell, and K. A. Boering (2001), Isotopic fractionation of methane in the stratosphere and its effect on free tropospheric isotopic compositions, *Geophys. Res. Lett.*, *28*(19), 3657–3660, doi:10.1029/2001GL013159.
McCarthy, M. C., K. A. Boering, A. L. Rice, S. C. Tyler, P. Connell, and E. Atlas (2003), Carbon and hydrogen isotopic compositions of stratospheric methane: 2. Two-dimensional model results and implications for kinetic isotope effects, *J. Geophys. Res.*, *108*(D15), 4461, doi:10.1029/2002JD003183.
McLinden, C. A., M. J. Prather, and M. S. Johnson (2003), Global modeling of the isotopic analogues of N_2O: Stratospheric distributions, budgets, and the ^{17}O–^{18}O mass-independent anomaly, *J. Geophys. Res.*, *108*(D8), 4233, doi:10.1029/2002JD002560.
Minschwaner, K., R. J. Salawitch, and M. B. McElroy (1993), Absorption of solar radiation by O_2: Implications for O_3 and lifetimes of N_2O, $CFCl_3$, and CF_2Cl_2, *J. Geophys. Res.*, *98*(D6), 10543–10561, doi:10.1029/93JD00223.
Murphy, D. M., and D. W. Fahey (1994), An estimate of the flux of stratospheric reactive nitrogen and ozone into the troposphere, *J. Geophys. Res.*, *99*(D3), 5325–5332, doi:10.1029/93jd03558.
Oberländer-Hayn, S. et al. (2016), Is the Brewer-Dobson circulation increasing or moving upward?, *Geophys. Res. Lett.*, *43*, 1772–1779, doi:10.1002/2015GL067545.
Olsen, M. A., A. R. Douglass, and M. R. Schoeberl (2002), Estimating downward cross-tropopause ozone flux using column ozone and potential vorticity, *J. Geophys. Res. Atmos.*, *107*(D22), 4636, doi:10.1029/2001JD002041.
Orbe, C., M. Holzer, L. M. Polvani, D. W. Waugh, F. Li, L. D. Oman, and P. A. Newman (2014), Seasonal ventilation of the stratosphere: Robust diagnostics from one-way flux distributions, *J. Geophys. Res. Atmos.*, *119*, 293–306, doi:10.1002/2013JD020213.

Osso, A., Y. Sola, K. Rosenlof, B. Hassler, J. Bech, and J. Lorente (2015), How robust are trends in the Brewer-Dobson circulation derived from observed stratospheric temperatures?, *J. Clim.*, *28*, 3024–3040, doi:doi: 10.1175/jcli-d-14-00295.1.

Pandey, A., and S. K. Bhattacharya (2006), Anomalous oxygen isotope enrichment in CO_2 produced from O+CO: Estimates based on experimental results and model predictions, *J. Chem. Phys.*, *124*, 234301, doi:10.1063/1.2206584.

Park, S. et al. (2012), Trends and seasonal cycles in the isotopic composition of nitrous oxide since 1940, *Nat. Geosci.*, *5*, 261–265, doi:10.1038/ngeo1421.

Park, S. Y., E. L. Atlas, K. A. Boering, P. Sunyoung, E. L. Atlas, K. A. Boering, S. Y. Park, E. L. Atlas, and K. A. Boering (2004), Measurements of N_2O isotopologues in the stratosphere: Influence of transport on the apparent enrichment factors and the isotopologue fluxes to the troposphere, *J. Geophys. Res.*, *109*, D01305, doi:10.1029/2003JD003731.

Plumb, R. A. (2007), Tracer interrelationships in the stratosphere, *Rev. Geophys.*, *45*, RG4005, doi:10.1029/2005RG000179.

Plumb, R. A., and M. K. W. Ko (1992), Interrelationships between mixing ratios of long lived stratospheric constituents, *J. Geophys. Res.*, *97*(D9), 10145–10156.

Quay, P., J. Stutsman, D. Wilbur, A. Snover, E. Dlugokencky, and T. Brown (1999), The isotopic composition of atmospheric methane, *Global Biogeochem. Cycles*, *13*, 445–461, doi:10.1029/1998gb900006.

Rahn, T., and M. Wahlen (1997), Stable isotope enrichment in stratospheric nitrous oxide, *Science*, *278*(5344), 1776–1778, doi:10.1126/science.278.5344.1776.

Rahn, T., J. M. Eiler, K. A. Boering, P. O. Wennberg, M. C. McCarthy, S. Tyler, S. Schauffler, S. Donnelly, and E. Atlas (2003), Extreme deuterium enrichment in stratospheric hydrogen and the global atmospheric budget of H_2, *Nature*, *424*(6951), 918–921, doi:10.1038/nature01917.

Randel, W. J., F. Wu, H. Vomel, G. E. Nedoluha, and P. Forster (2006), Decreases in stratospheric water vapor after 2001: Links to changes in the tropical tropopause and the Brewer-Dobson circulation., *J. Geophys. Res.*, *111*, D12312, doi:10.1029/2005jd006744.

Randerson, J. T., I. G. Enting, E. A. G. Schuur, K. Caldeira, and I. Y. Fung (2002), Seasonal and latitudinal variability of troposphere $\Delta^{14}C$: Post bomb contributions from fossil fuels, oceans, the stratosphere, and the terrestrial biosphere, *Global Biogeochem. Cycles*, *16*(4), 1112, doi:10.1029/2002GB001876.

Ray, E. A. et al. (2010), Evidence for changes in stratospheric transport and mixing over the past three decades based on multiple data sets and tropical leaky pipe analysis, *J. Geophys. Res.*, *115*, D21304, doi:10.1029/2010JD014206.

Rice, A. L., S. C. Tyler, M. C. McCarthy, K. A. Boering, and E. Atlas (2003), Carbon and hydrogen isotopic compositions of stratospheric methane: 1. High-precision observations from the NASA ER-2 aircraft, *J. Geophys. Res.*, *108*(D15), 4460, doi:10.1029/2002JD003042.

Riley, W. J., D. Y. Hsueh, J. T. Randerson, M. L. Fischer, J. G. Hatch, D. E. Pataki, W. Wang, and M. L. Goulden (2008), Where do fossil fuel carbon dioxide emissions from California go? An analysis based on radiocarbon observations and an atmospheric transport model, *J. Geophys. Res.*, *113*, G04002, doi:10.1029/2007JG000625.

Röckmann, T., J. Kaiser, and C. A. M. Brenninkmeijer (2003), The isotopic fingerprint of the pre-industrial and the anthropogenic N_2O source, *Atmos. Chem. Phys.*, *3*, 315–323.

Röckmann, T., M. Brass, R. Borchers, and A. Engel (2011), The isotopic composition of methane in the stratosphere: high-altitude balloon sample measurements, *Atmos. Chem. Phys.*, *11*, 13287–13304, doi:10.5194/acp-11-13287-2011.

Schinke, R., and P. Fleurat-Lessard (2005), The effect of zero-point energy differences on the isotope dependence of the formation of ozone: A classical trajectory study, *J. Chem. Phys.*, *122*, 94317, doi:10.1063/1.1860011.

Schmidt, J. A., M. S. Johnson, and R. Schinke (2011), Isotope effects in N_2O photolysis from first principles, *Atmos. Chem. Phys.*, *11*, 8965–8975, doi:10.5194/acp-11-8965-2011.

Simmonds, P. G. et al. (2013), Interannual fluctuations in the seasonal cycle of nitrous oxide and chlorofluorocarbons due to the Brewer-Dobson circulation, *J. Geophys. Res. Atmos.*, *118*, 10694–10706, doi:10.1002/jgrd.50832.

Stocker, T. F., D. Qin, G.-K. Plattner, M. Tignor, S. K. Allen, J. Boschung, A. Nauels, Y. Xia, V. Bex, and P. M. Midgley (Eds.) (2013), *IPCC, 2013: Climate Change 2013: The physical science basis. Contribution of Working Group I to the Fifth Assessment Report of the Intergovernmental Panel on Climate Change*, Cambridge University Press, New York, NY, USA.

Stueckelberg, E. C. G. (1932), Theory of inelastic collisions between atoms, *Helv. Phys. Acta*, *5*, 369–423.

Thiemens, M. H., T. Jackson, E. C. Zipf, P. W. Erdman, and C. Vanegmond (1995), Carbon-dioxide and oxygen-isotope anomalies in the mesosphere and stratosphere, *Science*, *270*(5238), 969–972, doi:10.1126/science.270.5238.969.

Thiemens, M. H., S. Chakraborty, and T. L. Jackson (2014), Decadal $\Delta^{17}O$ record of tropospheric CO_2: Verification of a stratospheric component in the troposphere, *J. Geophys. Res. Atmos.*, *119*, 6221–6229, doi:10.1002/2013jd020317.

Toyoda, S., N. Yoshida, T. Urabe, S. Aoki, T. Nakazawa, S. Sugawara, and H. Honda (2001), Fractionation of N_2O isotopomers in the stratosphere, *J. Geophys. Res.*, *106*(D7), 7515, doi:10.1029/2000JD900680.

Wang, L., and D. W. Waugh (2012), Chemistry-climate model simulations of recent trends in lower stratospheric temperature and stratospheric residual circulation., *J. Geophys. Res. Atmos.*, *117*, D09109, doi:10.1029/2011JD017130.

Wiegel, A. A., A. S. Cole, K. J. Hoag, E. L. Atlas, S. M. Schauffler, and K. A. Boering (2013), Unexpected variations in the triple oxygen isotope composition of stratospheric carbon dioxide, *PNAS*, *110*(44), 17680–17685, doi:10.1073/pnas.1213082110.

Van Wyngarden, A. L., K. A. Mar, K. A. Boering, J. J. Lin, Y. T. Lee, S.-Y. Lin, H. Guo, and G. Lendvay (2007), Nonstatistical behavior of reactive scattering in the $^{18}O+^{32}O_2$ isotope exchange reaction, *J. Am. Chem. Soc.*, *129*(10), 2866–2870, doi:10.1021/ja0668163.

Van Wyngarden, A. L. et al. (2014), The non-statistical dynamics of the $^{18}O+^{32}O_2$ isotope exchange reaction at two energies, *J. Chem. Phys.*, *141*, 64311, doi:10.1063/1.4892346.

Yang, H., G. Chen, Q. Tang, and P. Hess (2016), Quantifying isentropic stratosphere-troposphere exchange of ozone, *J. Geophys. Res. Atmos.*, *121*, 3372–3387, doi:10.1002/2015JD024180.

Yung, Y. L., A. Y. T. Lee, F. W. Irion, W. B. DeMore, and J. Wen (1997), Carbon dioxide in the atmosphere: Isotopic exchange with ozone and its use as a tracer in the middle atmosphere, *J. Geophys. Res.*, *102*(D09), 10857–10866, doi:10.1029/97jd00528.

Yung, Y. L., M. C. Liang, G. A. Blake, R. P. Muller, and C. E. Miller (2004), Evidence for O-atom exchange in the $O(^1D)+N_2O$ reaction as the source of mass-independent isotopic fractionation in atmospheric N_2O, *Geophys. Res. Lett.*, *31*, L19106, doi:10.1029/2004GL020950.

Chapter 2

Measurements of $^{14}CO_2$ in the stratosphere and free troposphere: Vertical profiles and empirical radiocarbon production rates

Abstract

Measurements and analyses of the vertical distribution of $\Delta^{14}CO_2$ in the troposphere and lower stratosphere are presented that provide much needed constraints on the spatial and temporal distribution of $^{14}CO_2$ necessary to (1) monitor the stratospheric circulation and stratospheric residence times, (2) quantify the partitioning of carbon between the atmosphere, biosphere, and oceans, and (3) infer regional and global fossil fuel emissions from the large number of $\Delta^{14}CO_2$ measurements made at Earth's surface. Measurements of $\Delta^{14}CO_2$ were performed on 150 whole air samples collected by NASA aircraft (ER-2, DC-8, and WB-57) from flight campaigns in 1997, 2000, 2004, 2012, and 2013. Correlations between $\Delta^{14}CO_2$ and N_2O mixing ratios in the stratosphere are used to estimate global annual mean net $^{14}CO_2$ fluxes between the stratosphere and the troposphere, which are approximately half of the global ^{14}C production rates. To within the uncertainties, these isotope fluxes have not changed between 1997 and 2013, suggesting that stratospheric age spectra are likely wide enough to damp out variations in the ^{14}C production rate caused by the 11-year solar cycle. A lack of dependence on the solar cycle simplifies the use of stratospheric $\Delta^{14}CO_2$ measurements as a tracer of stratospheric transport to detect and monitor possible changes in the stratospheric circulation and residence times due to increases in radiative forcing from greenhouse gases, as well as to quantify the transport of $^{14}CO_2$ from the stratosphere to the troposphere necessary for carbon cycle studies.

2.1 Introduction

Radiocarbon is formed in the lower stratosphere and upper troposphere by nuclear spallation reactions between nitrogen nuclei and thermal neutrons, which are created by galactic cosmic rays and by atmospheric nuclear weapons testing in the mid-twentieth century. The massive injection of ^{14}C into the stratosphere from atmospheric nuclear weapons detonation, and its redistribution throughout the atmosphere, has been used in the past to determine key characteristics of the stratospheric circulation [e.g., *Hall and Waugh*, 2000; *Jackman et al.*, 1991; *Johnston*, 1989; *Kinnison et al.*, 1994; *Park et al.*, 1998; *Prather and Remsberg*, 1993]. Now, however, the distribution of $^{14}CO_2$ in the stratosphere is determined by natural ^{14}C production by cosmic rays, in addition to transport within the stratosphere and transport from the stratosphere to the troposphere. Recently, we showed that $^{14}CO_2$ observations are a sensitive diagnostic of the stratospheric circulation in models [*Kanu et al.*, 2016], complementary to, e.g., mean ages from SF_6 and CO_2 measurements, and likely to more directly reflect residence times in the lower stratosphere [e.g., *Hall and Waugh*, 2000; *Waugh and Hall*, 2002; *Kjellström et al.*, 2000; *Prather and Remsberg,* 1993]. A time series of $^{14}CO_2$ observations may thus prove useful in detecting a change of the stratospheric circulation due to increased radiative forcing by greenhouse gases and ozone depletion as predicted by chemistry-climate models [e.g., *Li et al.*, 2008; *Oberländer-Hayn et al.*, 2016]. In *Kanu et al.* [2016], we also demonstrated that $\Delta^{14}CO_2$ measurements from 2003–2005, combined with simultaneous measurements of N_2O mixing

ratios, can be used to empirically estimate the global ^{14}C production rate by cosmic rays. We noted that a time series of $^{14}CO_2$ observations that span a solar cycle could be used to test the dependence of stratospheric $^{14}CO_2$ levels on solar activity.

Here, we present 150 measurements of $\Delta^{14}CO_2$ in the Northern Hemisphere from newly collected as well as archived CO_2 samples from 1997, 2000, 2004, 2012, and 2013. This dataset substantially increases the number of measurements available to investigate the stratospheric circulation and the natural ^{14}C production rate, as mentioned above, as well as to provide vertical constraints on the $^{14}CO_2$ distribution in the troposphere needed for studies of carbon partitioning among its various reservoirs and top-down estimates of fossil fuel emissions [e.g., *Basu et al.*, 2016; *Graven et al.*, 2015; *Levin et al.*, 2003, 2010; *Turnbull et al*., 2011; *Randerson et al.*, 2002]. First, we use the $\Delta^{14}CO_2$ measurements and their correlation with N_2O mixing ratios to empirically estimate the global annual mean net $\Delta^{14}CO_2$ flux from the stratosphere to the troposphere and the global ^{14}C production rate for each year that samples are available and then discuss their relevance for monitoring rates and characteristics of the stratospheric circulation. Second, we present vertical profiles of $\Delta^{14}CO_2$ from the lower or middle troposphere into the lower stratosphere covering a range of latitudes. The many profiles show a general increase in $\Delta^{14}CO_2$ with altitude, while two profiles show interesting deviations from this trend; we interpret these nonconformities with the help of simultaneous measurements of other tracers and back trajectory calculations.

2.2 Methods

Whole air samples were collected aboard the NASA ER-2, WB-57F, and DC-8 aircraft as part of the POLARIS [*Newman et al.*, 1999], SOLVE [*Newman et al.*, 2002], Pre-AVE [*Schoeberl et al.*, 2008], DC3 [*Barth et al.*, 2015], and SEAC4RS [*Toon et al.*, 2016] campaigns, described in more detail below. The whole air samples were analyzed for more than 50 trace gas mixing ratios by gas chromatography/mass spectrometry (GC-MS). For a subset of these samples, CO_2 was cryogenically extracted, stored in flame-sealed glass ampoules, then, graphitized and measured for $\Delta^{14}C$ by accelerator mass spectrometry (AMS).

For the POLARIS and SOLVE missions, samples were collected by the NCAR Whole Air Sampler (WAS) [*Flocke et al.*, 1999; *Schauffler et al.*, 1998] on a NASA ER-2 aircraft. The POLARIS samples that were archived and measured for $\Delta^{14}CO_2$ were collected between 3° and 90°N and between 11 and 21 km in September 1997; the SOLVE samples for which $\Delta^{14}CO_2$ measurements are reported here were collected between 25° and 75°N and between 11 and 20 km and in January–February 2000. The Pre-AVE samples were collected by the WAS on the NASA WB-57F aircraft between 1°S and 38°N and between 10 and 19 km in January 2004. At NCAR or University of Miami (UM), the mixing ratios of ~50 species were measured by gas chromatography-mass spectrometry or gas chromatography-flame ionization detection (GC-FID), with limits of detection of better than 2 ppt for non-methane hydrocarbons and 0.1 pptv for other species [*Flocke et al.*, 1999]. For POLARIS, N_2O mixing ratios were measured *in situ* by the ATLAS [*Podolske and Loewenstein*, 1993] and ALIAS [*Webster et al.*, 1994] instruments. If both ATLAS and ALIAS measurements were available, the ATLAS measurement was used for analysis here. For SOLVE, N_2O mixing ratios were measured *in situ* by the ATLAS instrument and in the whole air samples by gas chromatography with electron capture detection (GC/ECD)

[*Schauffler et al.*, 2003]. If WAS measurements were not available for a sample, ATLAS measurements were used. For pre-AVE, N_2O mixing ratios were measured by GC/ECD.

For the DC3 mission, samples measured for $\Delta^{14}CO_2$ were collected by UC Irvine's WAS on the NASA DC-8 aircraft from a single ascent at 35°N from 1 to 12 km on 21 May 2012. Sample canisters were shipped back to UC Irvine and analyzed by gas chromatography (GC) for ~50 trace gas mixing ratios within 1 week of collection, with precisions between 1 and 5% [*Schroeder et al.*, 2014]. High time resolution (1s) *in situ* measurements of water vapor, O_3, and CO are also used in the analysis of this flight. Water vapor was measured by near-infrared laser hygrometry [*Diskin et al.*, 2002; *Podolske et al.*, 2003], CO mixing ratios by mid-infrared tunable diode laser absorption spectroscopy (DACOM) [*Sachse et al.*, 1991; 1987], and O_3 by chemiluminescence [*Ryerson et al.*, 1998].

For the SEAC4RS mission, samples from 11 individual vertical profiles between 16° and 50°N and between 5 and 21 km were collected by the WAS instrument on a NASA ER-2 aircraft in August and September 2013. Trace gas mixing ratios were measured at UM by GC/MS, with limits of detection better than 0.1 ppt [*Flocke et al.*, 1999; *Schauffler et al.*, 2003]. High time resolution (1s) *in situ* measurements of O_3 were obtained by UV photometry [*Gao et al.*, 2012], water vapor by tunable diode laser spectrometry [*Sargent et al.*, 2013; *Weinstock et al.*, 1994], and CO (±7.25 ppb), CO_2 (± 0.04 ppm), and CH_4 (± 0.25 ppb) by cavity ring-down spectroscopy [e.g., *Werner et al.*, 2017]. N_2O mixing ratios were not available for the SEAC4RS samples, so we use the tight correlation between N_2O and CH_4 mixing ratios measured for all the other missions in this study to estimate the N_2O mixing ratio for each SEAC4RS sample (Figure 2.S1) using the measured CH_4 mixing ratio as a proxy.

After trace gas concentration measurements at NCAR, UM, or UC Irvine, the samples were shipped to UC Berkeley where CO_2 was cryogenically separated from the whole air samples by slowly flowing the sample through a series of five liquid nitrogen (LN_2) traps and then sequentially replacing the LN_2 with ethanol-LN_2 slushes at –75°C to separate CO_2 from water [e.g., *Boering et al.*, 2004; *Wiegel et al.*, 2013]. The purified CO_2 was then flame-sealed in a glass ampoule. Samples containing greater than 15 μmol CO_2 were split into 2 or 3 aliquots of 10–20 μmol each for separate analyses of radiocarbon and, for some samples, $\delta^{13}C$, $\delta^{17}O$, and $\delta^{18}O$ of CO_2 [e.g., *Boering et al.*, 2004; *Wiegel et al.*, 2013].

At the Lawrence Livermore National Laboratory Center for Accelerator Mass Spectrometry (LLNL-CAMS), the purified CO_2 was reduced to graphite by catalytic reduction by Fe in H_2 and then pressed into aluminum targets, and the radiocarbon content was measured [e.g., *Graven et al.*, 2012a; b]. The values reported here are $\Delta^{14}C$ for geochemical samples with corrections for fractionation and age of the sample, as defined in Stuiver and Polach [1977], and have a precision of 1.5 to 2‰.

A brief summary of the method for estimating the global annual mean net flux of $^{14}CO_2$ as has been described previously by Kanu *et al.* [2016] is provided here. The slope of a compact relationship between two tracers that are long-lived with respect to vertical and quasi-horizontal transport is equal to the ratio of their net vertical fluxes [*Plumb and Ko*, 1992; *Plumb*, 2007]. Thus, the slope of the measured $\Delta^{14}CO_2$:N_2O correlation and an independent estimate of the net

vertical flux of N_2O – which is simply the global N_2O loss rate – can be used to estimate the net vertical flux of $\Delta^{14}CO_2$. This approach has also been used to estimate net vertical fluxes of $\Delta^{17}O$ of CO_2 [*Luz et al.*, 1999; *Boering et al.*, 2004], of N_2O isotopologues [*McLinden et al.*, 2003; *Park et al.*, 2004], and of O_3 [*Murphy and Fahey*, 1994]. The longer expression reported in Kanu *et al.* [2016] can be simplified to Equation (1) because the difference in CO_2 mixing ratios for air entering and leaving the stratosphere is much less than 1% and so the terms including the explicit air mass fluxes between the stratosphere and troposphere (see *Kanu et al.* [2016] and Section 3.2.1) cancel.

$$\text{Global Net } \Delta^{14}CO_2 \text{ flux} = -\,m \cdot (L+G_{strat}) \cdot [CO_2] \qquad (1)$$

In Equation (1), $[CO_2]$ is the mixing ratio of carbon dioxide (at, e.g., the tropical tropopause; see *Andrews et al.* [2001]), L is the global loss rate of N_2O (4.5×10^{11} mol N_2O yr^{-1} from *Minschwaner et al.* [1993]; *Prather and Ehhalt* [2001]), G is the stratospheric growth rate (1.1×10^{10} mol N_2O yr^{-1}, which is 10% of the tropospheric growth rate [*Denman and Brasseur*, 2007]), and *m* is the observed slope of the $\Delta^{14}CO_2$:N_2O correlation, which is described in more detail in the following paragraph. We note that the global annual mean net $\Delta^{14}CO_2$ flux in Equation (1) is equivalent to the stratospheric portion of the natural cosmogenic ^{14}C production rate [*Kanu et al.*, 2016]. Assuming that half of the ^{14}C production occurs in the stratosphere [*Masarik and Beer*, 1999; 2009], the global annual mean ^{14}C production rate is then equal to twice the global annual mean net $\Delta^{14}CO_2$ flux [*Kanu et al.*, 2016].

In this work, the slope of the $\Delta^{14}CO_2$:N_2O correlation for samples above the lapse-rate tropopause and with N_2O mixing ratios greater than 250 ppb was determined by a Williamson-York bivariate fit which takes uncertainties in both the x and y data into account [*Cantrell*, 2008]. Whether a sample was collected above or below the lapse-rate tropopause was determined for each flight by a microwave temperature profiler [*Denning et al.*, 1989] for all but the pre-Ave flights. For the pre-Ave mission, samples with O_3>100 ppb were used in the regression in lieu of measured tropopause heights. In addition, a sample from the SEAC4RS mission that was collected above the tropopause but had anomalously low radiocarbon was excluded from the regression; *in situ* and whole air sample GC-MS measurements of other trace gases suggest that this air had recently entered the stratosphere, and the likely origin of this sample will be discussed further in Section 2.3.3.

2.3 Results and Discussion

The 150 aircraft measurements presented here span a 16-year time period and, for 2013, are the first hemispheric-scale $^{14}CO_2$ vertical profiles that extend from the lower or middle troposphere into the lower stratosphere over a wide range of latitudes in the Northern Hemisphere. Vertical profiles of $\Delta^{14}CO_2$ from aircraft flights in 1997, 2000, 2004, 2012, and 2013, along with data from balloon flights in 2003, 2004, and 2005 [*Kanu et al.*, 2016] are shown in Figure 2.1(a). For any given time period, $\Delta^{14}CO_2$ generally increases with altitude, especially above the tropopause, as expected for a long-lived species that is produced in the upper troposphere and stratosphere. In Figure 2.1(b), plotting $\Delta^{14}CO_2$ versus the long-lived tracer N_2O reduces the variability further, as expected for two long-lived tracers [e.g., *Plumb,* 2007], resulting in a more compact relationship for each time period. Figures 2.1(a) and 2.1(b) both

show that the decrease of 5–10‰ yr^{-1} in tropospheric $\Delta^{14}CO_2$ associated with fossil fuel emissions [e.g., *Graven et al.*, 2012a] propagates into the stratosphere, as discussed for the balloon profiles in Kanu *et al.* [2016]. Figure 2.2 shows $\Delta^{14}CO_2$ measurements as a function of altitude and latitude for all the samples collected during the SEAC4RS mission (N_{total} = 84) in August and September 2013.

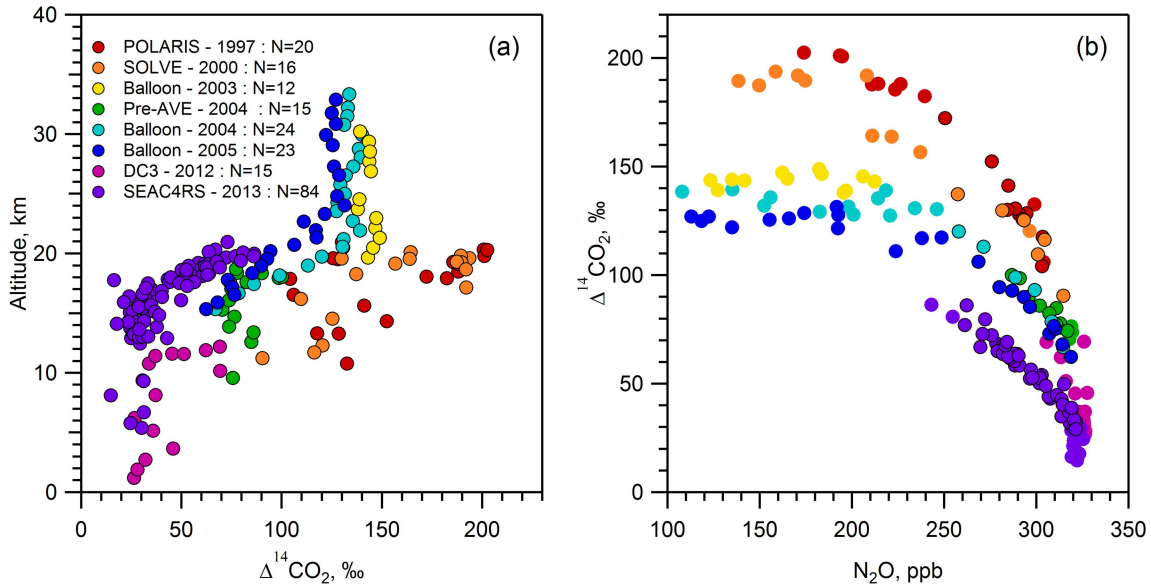

Figure 2.1 (a) Vertical profiles of $\Delta^{14}CO_2$ for POLARIS, SOLVE, pre-AVE, balloon flights in 2003, 2004, and 2005 [*Kanu et al,* 2016], DC3, and SEAC4RS. (b) Measurements of $\Delta^{14}CO_2$ versus simultaneous measurements of N_2O. In (b), stratospheric data points for which 250<N_2O<320 ppbv are outlined in black and were used to determine the slope of the $\Delta^{14}CO_2$: N_2O relationship for calculating the global annual mean net $\Delta^{14}CO_2$ flux from the stratosphere to the troposphere and the global ^{14}C production rate.

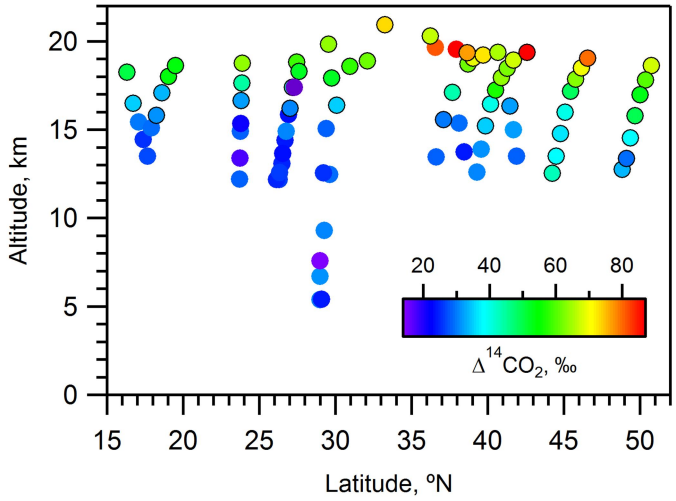

Figure 2.2 Measurements of $\Delta^{14}CO_2$ (on the color scale) as a function of altitude and latitude for SEAC4RS (2013). As in Figure 2.1(b), stratospheric data points for which 250<N_2O<320 ppbv are outlined in black and were used to determine the slope of the $\Delta^{14}CO_2$: N_2O relationship.

2.3.1 $\Delta^{14}CO_2$:N_2O correlations, net $\Delta^{14}CO_2$ fluxes, and ^{14}C production rates

The inverse relationship between stratospheric $\Delta^{14}CO_2$ and N_2O shown in Figure 2.1(b), is highly correlated for each sampling period, as expected for species that are long-lived with respect to vertical and quasi-horizontal transport [e.g., *Plumb 2007*]. Figure 2.1(b) shows that there are roughly three regimes with respect to N_2O mixing ratio: $N_2O \geq$ ~320 ppb, consisting of tropospheric air or air that has very recently entered the stratosphere; 250 ppb < N_2O < 320 ppb, where $\Delta^{14}CO_2$ versus N_2O shows a roughly linear relationship; and N_2O < 250 ppb, where $\Delta^{14}CO_2$ increases curvilinearly then plateaus or decreases slightly as N_2O mixing ratios decrease. For the balloon datasets, $^{14}CO_2$ levels appear to transition smoothly between these N_2O regimes, but the SOLVE and arguably the POLARIS data show discontinuous increases of ~20 to 30‰ in $\Delta^{14}CO_2$ for samples with N_2O < ~200 ppbv. For the SOLVE samples, the measured relationships between potential temperature (θ), CFC-11, and N_2O (shown in Figure 2.3) reveal that the samples with N_2O<~200 ppbv were collected in the polar vortex while those with N_2O>~200 ppbv were collected outside the vortex; the discontinuity at ~200 ppbv is especially distinct because one sample with N_2O=207 ppbv was collected inside the vortex at 71.7°N at a potential temperature of ~400K (with high $\Delta^{14}CO_2$) while the other sample with N_2O = 210 ppbv was collected outside the vortex at 40.6°N at a potential temperature of 502K. As *Plumb* [2007] illustrates, the descent of air in the vortex and subsequent mixing creates a third regime of long-lived tracer-tracer relationships that reflect a different set of transport histories than those in the isolated tropics and in the well-mixed midlatitudes. As Plumb cautions, these different relationships are created by different transport and mixing histories and not necessarily local production or loss (i.e., chemical, or, for ^{14}C, nuclear) processes. Indeed, this bifurcation in tracer:tracer relationships at ~180–210 ppbv is seen in the correlations of N_2O with CFC-11 and a number of other long-lived tracers (e.g., Figure 2.3(c) for SOLVE and 2.3(d) for POLARIS for CFC-11:N_2O and in *Plumb* [2007] and references therein for CFC-11:N_2O and many other tracers such as HF) as well as for N_2O isotopic compositions [e.g., *Park et al.*, 2004] which are also driven by transport, not local production or loss. These relationships driven by descent in the winter/spring vortex can persist in the lower stratosphere at high latitudes through the summer when transport is weak, as observed during the POLARIS mission even in September [e.g., *Newman et al.,* 1999]; in fact, this is why air with N_2O<200 ppbv can be sampled at aircraft altitudes (below 21 km) – air with much lower N_2O from much higher altitudes descended in the polar vortex and, sampled in vortex remnants, has not entirely mixed into the background extratropical air. Thus, while it might be tempting to attribute the ~20 to 30‰ enhancement in measured $\Delta^{14}CO_2$ for N_2O<200 ppbv for the SOLVE and POLARIS samples to higher production rates of $^{14}CO_2$ at high latitudes, the similar discontinuities in the potential temperature and CFC-11 relationships versus N_2O for SOLVE and for the CFC-11 and N_2O relationship for POLARIS indicate that the primary driver of these discontinuities is the influence of the descent of much older air with higher $^{14}CO_2$ levels from higher altitudes (where, in fact, the instantaneous ^{14}C production rate is slower than at low altitudes) in the polar vortex.

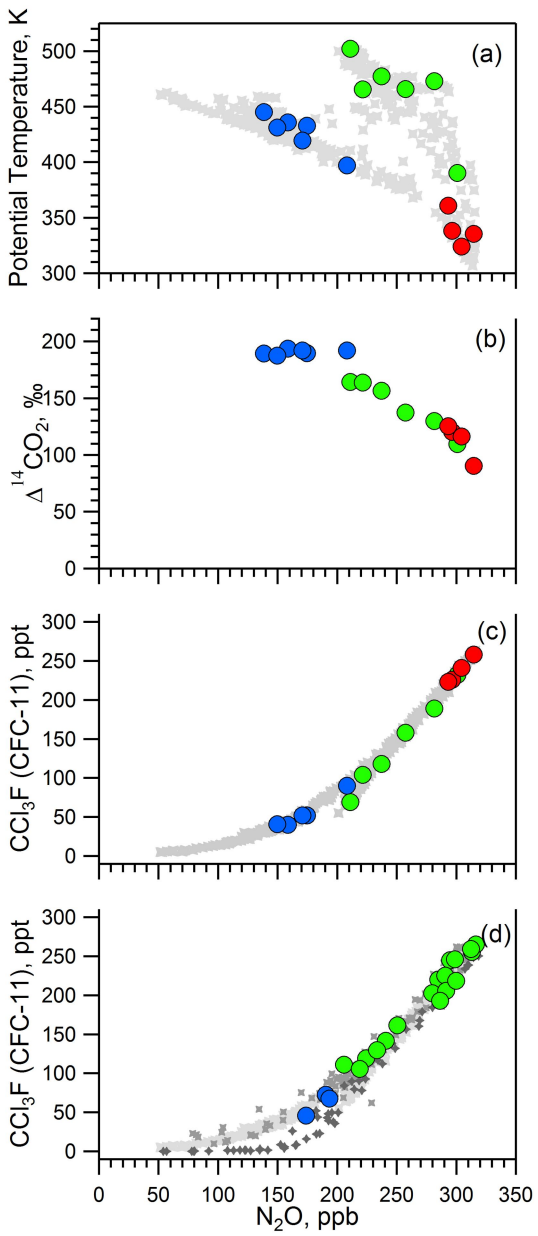

Figure 2.3 Scatter plots of (a) potential temperature, (b) $\Delta^{14}CO_2$, and (c) CCl_3F (CFC-11) versus N_2O for all SOLVE whole air samples (gray) and for SOLVE whole air samples for which $\Delta^{14}CO_2$ was measured (color). The potential temperature:N_2O relationships for SOLVE in (a) clearly separate the air samples into vortex air (blue), extra-vortex/midlatitude air (green) or mixed/non-definitive (red) [see *Greenblatt et al.*, 2002], which is consistent with the measured CFC-11:N_2O correlations showing vortex samples (blue) falling on the concave side of the extra-vortex samples (green). [e.g., see *Plumb*, 2007] (d) CFC-11 versus N_2O for all SOLVE (light gray x), POLARIS (medium gray x), and midlatitude (34°N) balloon (dark gray +) whole air samples along with POLARIS whole air samples for which $\Delta^{14}CO_2$ was measured (color). Although the POLARIS samples shown here were collected in August and September, the CFC-11:N_2O relationships show that the influence of air that had descended from higher altitudes in the polar vortex the previous spring is still apparent for N_2O<200 ppbv and thus had lower N_2O mixing ratios and higher $\Delta^{14}CO_2$ relative to that for midlatitude air.

While the low N_2O regime yields insight into differences in transport histories between middle stratospheric air and air that has descended and mixed out of the polar vortex and was sampled in the lower stratosphere, the linear regime of the $\Delta^{14}CO_2$:N_2O relationship (250<N_2O< 320 ppbv) reflects the fact that $\Delta^{14}CO_2$ and N_2O are in "slope-equilibrium" in the extratropics where quasi-horizontal (isentropic) transport is much faster than vertical (diabatic) transport and thus their slope is equal to the ratio of their global net vertical fluxes [e.g., *Plumb and Ko, 1992*; *Plumb*; 2007]. As described in the Methods section and in *Kanu et al.* [2016], the slope of the $\Delta^{14}CO_2$:N_2O relationship for N_2O > 250 ppb for each sampling period was used to empirically estimate the global annual mean net $\Delta^{14}CO_2$ flux from the stratosphere to the troposphere and the global ^{14}C production rate using an independent estimate of the global net vertical flux of N_2O. The results for 1997, 2000, 2004, and 2013 are given in Table 2.1 and shown in Figure 2.4. To within the uncertainties of the regressions, the annual global mean $\Delta^{14}CO_2$ fluxes and the ^{14}C production rates over the 16-year sampling period are similar to each other and to those estimated from the balloon flights in 2004 and 2005 [*Kanu et al.*, 2016]. In the following discussion, we use this extensive new dataset to examine the robustness of our estimates for the global annual mean $\Delta^{14}CO_2$ fluxes and the global ^{14}C production rates and then whether an 11-year cycle in ^{14}C production rates can be discerned.

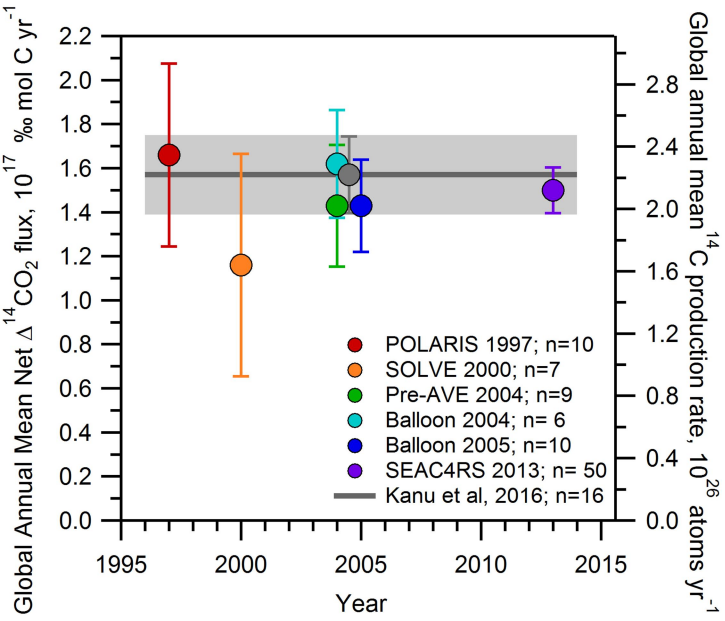

Figure 2.4 The global annual mean net flux for $\Delta^{14}CO_2$ (primary y-axis) and the global ^{14}C production rate (secondary y-axis) estimated by Equation (1) and the observed $\Delta^{14}CO_2$:N_2O relationship as a function of year. The error bars represent the 2σ uncertainty from the $\Delta^{14}CO_2$:N_2O regression. Known and estimated systematic uncertainties that we expect to be constant across these datasets are not included in this plot, such as the 25% uncertainty in the N_2O loss rate, a possible range for the fraction of ^{14}C produced in the stratosphere of 0.5 to 0.65, and a conservative estimate for the effect of the transport of ^{14}CO to the troposphere before it is fully oxidized to stratospheric $^{14}CO_2$ of <5% (see text).

Table 2.1 Global annual mean net $\Delta^{14}CO_2$ fluxes and ^{14}C production rates

Campaign	Year	$\Delta^{14}CO_2$ flux,* 10^{17} ‰ mol C yr^{-1}	^{14}C Production rate, 10^{17} ‰ mol C yr^{-1}	^{14}C Production rate, 10^{26} atoms yr^{-1}
POLARIS	1997	1.66 ± 0.41	3.31 ± 0.83	2.34 ± 0.59
SOLVE	2000	1.16 ± 0.51	2.31 ± 1.01	1.64 ± 0.72
AVE	2004	1.43 ± 0.28	2.86 ± 0.55	2.02 ± 0.39
Balloon 2004-2005	2004/2005	1.57 ± 0.17	3.14 ± 0.35	2.22 ± 0.24
SEAC4RS	2013	1.50 ± 0.11	3.00 ± 0.22	2.13 ± 0.15

* Errors are the 2σ uncertainty in the slope of the $\Delta^{14}CO_2$:N_2O relationship used in Equation (1). The overall uncertainty, including known and estimated systematic errors, is ± 30%.

The large number of stratospheric samples and their wide-ranging distribution from 16° to 50°N from the SEAC4RS mission (Figure 2.2) allows us to test the robustness of the slope-equilibrium approach for calculating the global annual mean net $\Delta^{14}CO_2$ fluxes. While the derivation by *Plumb and Ko* [1992] assumed that the two long-lived tracers had to be in slope-equilibrium globally, Plumb [2007] has shown that the net global fluxes can be obtained from the slope of two tracers in the relatively well-mixed extratropics (even though in general the tropical tracer: tracer relationships are different). Indeed, he notes that the ability to obtain an accurate slope from observations may be more limiting than the assumptions underlying the global net flux derivation. Of the 84 total samples from the SEAC4RS mission, 50 of them were collected above the tropopause and had N_2O mixing ratios greater than 250 ppbv. Figure 2.5 shows the net $\Delta^{14}CO_2$ fluxes resulting from each of the 8 individual vertical profiles (colored circles) and those resulting from binning the samples into various latitude ranges (black circles). Although there is more scatter in the fluxes derived from individual profiles – most likely due to noise from fewer samples – there is no significant latitude dependence. These results also support our model test in *Kanu et al.* [2016] in which we used modeled values for $\Delta^{14}CO_2$ and N_2O in a 3D Chemical Transport Model and were able to derive the global ^{14}C production rate implemented in the model from the $\Delta^{14}CO_2$:N_2O slope.

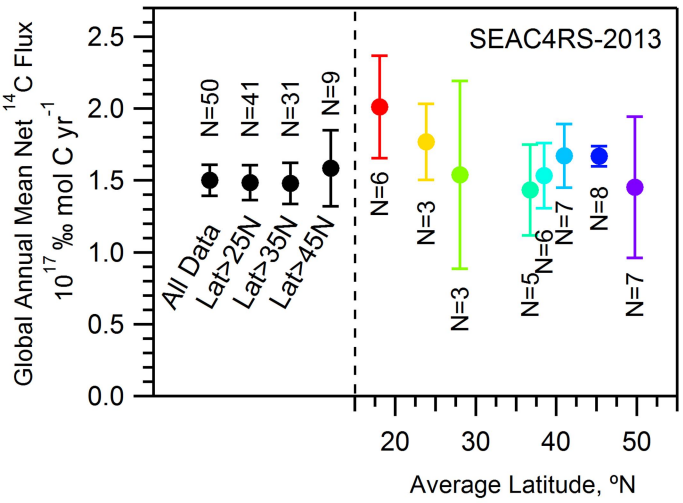

Figure 2.5 Global annual mean net $\Delta^{14}CO_2$ fluxes estimated from all SEAC4RS stratospheric data with 250<N_2O, from subsets of this SEAC4RS data based on latitude, and from individual aircraft vertical profiles, as labeled. The fluxes for individual ascents and/or descents are plotted against the average latitude of that particular vertical profile. According to Plumb [2007], robust ratios of the global net vertical fluxes of long-lived tracers can be derived from their tracer-tracer relationships even from regional-scale observations in the well-mixed extratropics. Here, there is good agreement between using the total dataset and using a subset from various latitude regions or even from single vertical profiles, although the uncertainty increases as N decreases; it is not clear whether the profile centered at 15°N shows more scatter because N is small or whether air this far equatorward is not well-mixed enough to meet the slope-equilibrium requirement.

The SEAC4RS results also suggest, not surprisingly, that larger datasets will provide net $\Delta^{14}CO_2$ fluxes and ^{14}C production rates with significantly smaller uncertainties. For example, while the SEAC4RS dataset is comprised of many samples (N=50) uniformly distributed over a wide range of latitudes, the POLARIS (N=10) and SOLVE (N=7) datasets are comprised of close to an order of magnitude fewer samples that also have a spotty distribution across a wide range of latitudes. For both of these early missions (for which very few archived samples were still available), we have also calculated the slopes using a combination of N_2O measurements from different instruments, which are not always in good agreement when the measurements overlap (see Tables S1 and S2). All of these contribute to the larger uncertainties in the POLARIS and SOLVE $\Delta^{14}CO_2$:N_2O slopes (Table 2.1; Figure 2.4). Moreover, the SOLVE $\Delta^{14}CO_2$ flux (with N=7) is extremely sensitive to the limits in N_2O mixing ratios used to define the regression range (e.g., choosing N_2O> 250 ppbv versus N_2O>280 ppbv) – more so than the other sets of measurements. Additionally, two of the seven samples used in the SOLVE regression have elevated CO mixing ratios (~35 ppb compared to ~15 ppb for other SOLVE samples) and, for oxygen isotopes in CO_2, a depressed $\Delta\ln^{18}O/\Delta\ln^{17}O$ slope (0.65 and 0.84 compared to the average extratropical value of 1.71) [*Wiegel, et al.*, 2013]. In the context of oxygen isotope enrichments in CO_2, which have an exclusively stratospheric source, these anomalies are interpreted as (1) mixing of low N_2O air from high altitudes with high N_2O air from low altitudes within the stratosphere or (2) mixing of stratospheric air with air that has recently been transported from the troposphere. [*Wiegel, et al*, 2013] If (2) is the case, then the

"slope-equilibrium" approach may be less representative than if the samples were from the well-mixed region in the stratospheric overworld, thus contributing to the large uncertainty in the SOLVE global annual mean net isotope flux.

2.3.2 Trends in the $\Delta^{14}CO_2$ fluxes and ^{14}C production rates

We examine this new time series of global annual mean net $\Delta^{14}CO_2$ fluxes and global ^{14}C production rates shown in Figure 2.4 to try to discern the 11-year solar cycle in ^{14}C production rates. In principle, variations in stratospheric $\Delta^{14}CO_2$ levels could reflect variations in the ^{14}C production rate due to the 11-year solar cycle (which modulates the galactic cosmic ray penetration into the atmosphere) and/or changes in the stratospheric circulation and stratosphere-to-troposphere transport.

First, we consider our estimates of the radiocarbon production rates from the $\Delta^{14}CO_2$:N_2O correlation. Cosmogenic ^{14}C production rates are known to vary inversely with sinusoidal variations in solar activity – often quantified as the number of observed sunspots – since increases in solar activity strengthen Earth's geomagnetic field that, in turn, attenuates cosmic rays [e.g., *Dutta*, 2016 and references within]. To illustrate the solar cycle phase with respect to our empirical global ^{14}C production rates, Figure 2.6 shows the monthly mean International Sunspot Number [SILSO] along with the net $\Delta^{14}CO_2$ isotope fluxes and ^{14}C production rates from Figure 2.4. Furthermore, since there is likely a time lag with respect to solar-cycle variations in the ^{14}C production rate and the buildup of or decrease in stratospheric $^{14}CO_2$ levels, the net $\Delta^{14}CO_2$ fluxes and ^{14}C production rates for each year are also shown in Figure 2.6 shifted by −2 years (open circles) and −5 years (open squares) – which are typical mean ages of air in the lower midlatitude and high latitude stratosphere, respectively [e.g., *Boering et al.*, 1996; *Hall et al.,* 1999; *Waugh and Hall*, 2002]. Although our sampling is somewhat sparse in time, sampling did occur at different stages of the 11-year sunspot cycle. Even if we imagine that there is some signal in the current noise, an anti-correlation of the empirical ^{14}C production rates for 1997, 2000, 2004, and 2013 with the solar cycle cannot be discerned. We suspect that solar-cycle variations in the ^{14}C production rate are damped out by the width of stratospheric age spectra and their long tails [e.g., *Waugh and Hall*, 2002]. For example, observation- and model-derived age spectra for midlatitude lower stratospheric air have spectral widths of ~2 years (for which the spread in the broadest part of the age spectrum is twice that, or 4 years [e.g., *Andrews et al.,* 2001; *Li, et al*., 2012] and tails extending out to at least 8 years [*Ehhalt et al.*, 2002; *Waugh and Hall*, 2002], and they may be characterized by a bimodal distribution of newer and older air with mean ages of 1 year and 5 years at N_2O levels of 250 ppbv [*Andrews et al.,* 2001]. Contributions of such a wide range of transport and mixing times for air in the lower stratosphere could explain the apparent lack of sensitivity to the solar cycle in this dataset. Further observations of precise $\Delta^{14}CO_2$ measurements in the extratropics will be needed to determine the robustness of this conclusion.

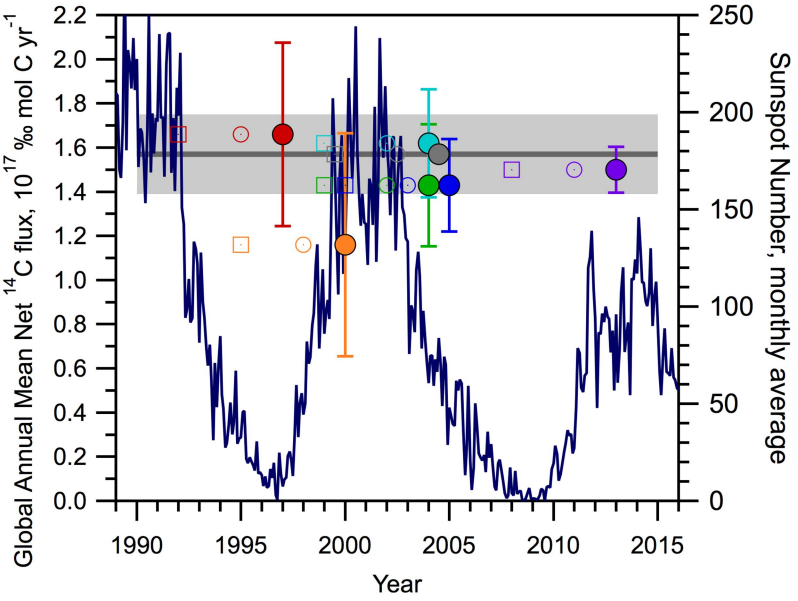

Figure 2.6 The global annual mean net $\Delta^{14}CO_2$ fluxes (primary y-axis) from Figure 2.4 (solid circles) shown with the monthly averaged International Sunspot Number (SILSO, Royal Observatory of Belgium, Brussels) on the secondary y-axis. Open symbols show the net $\Delta^{14}CO_2$ fluxes shifted by –2 years (open circles) and –5 years (open squares); see text.

We also note that lack of a solar cycle dependence in our values for the net $\Delta^{14}CO_2$ flux to the troposphere and the corresponding ^{14}C production rate cannot be extended to the net flux of ^{14}CO to the troposphere. *Jöckel and Brenninkmeijer* [2002] have shown that interpretation of stratospheric ^{14}CO levels and their transport to the troposphere and subsequent evolution there requires that the solar cycle in the ^{14}C cosmogenic production rate be taken into account when, e.g., comparing measurements of ^{14}CO from different time periods. This is because the lifetime of CO with respect to oxidation by OH to CO_2 is on the order of 2–3 months; thus, some stratospheric ^{14}CO will be transported to the troposphere before it is oxidized, so a solar cycle in ^{14}CO production reflects recent production rate and is not be damped out by the wide age spectra of stratospheric air. Given this loss of a fraction of ^{14}CO to the troposphere before it is oxidized to $^{14}CO_2$, we estimated in Kanu *et al.* [2016] a conservative upper bound to the potential low bias in our ^{14}C production rates derived from the observed $\Delta^{14}CO_2$:N_2O slopes of < 5%, based on ^{14}CO observations in the lower stratosphere [*Brenninkmeijer et al.*, 1995].

Second, there does not appear to be a long-term trend in the global annual mean net $\Delta^{14}CO_2$ fluxes derived from the $\Delta^{14}CO_2$:N_2O correlation shown in Figures 2.4 and 2.6. However, in contrast to the solar-activity-driven variations in the ^{14}C production rate discussed above, which in principle could be sensitive to solar activity if, we believe, the age spectra were more peaked and had shorter tails, we do not expect that the global annual mean net $\Delta^{14}CO_2$ fluxes will be very sensitive to a change in the annual mean air mass fluxes out of the stratosphere, for example. Indeed, air mass fluxes do not appear in Equation (1) for the net $\Delta^{14}CO_2$ fluxes in Section 2.2 above since, given that CO_2 levels in the stratosphere are only ~1% less than CO_2

levels in the troposphere, the air mass fluxes cancel out to good approximation (see Kanu *et al.* [2016] for the full equation). This insensitivity to air mass fluxes between the stratosphere and troposphere – which themselves can differ by a factor of 3 depending on simply the definition of the tropopause surface (compare, e.g., *Appenzeller et al.* [1996] across the 380K surface with *Holton* [1990] across the 100 mbar surface) – can be understood as follows: if the air mass flux between the stratosphere and troposphere increases, the accumulation of stratospheric $^{14}CO_2$ would decrease; conversely, if the air mass flux decreases, $^{14}CO_2$ accumulation would increase. Since the net isotope flux is a product of the two, it remains roughly constant. This argument has been applied in many other stratospheric isotope studies to indicate that we can quantify net isotope fluxes from the stratosphere to the troposphere for isotopic species with stratospheric sources, such as $\Delta^{17}O$ of CO_2 [e.g., Luz *et al*., 1999] and N_2O isotopologues [e.g., Park *et al.*, 2004], without explicitly knowing the air mass fluxes. For this study, it means that we should not expect to see a long-term trend in the global annual mean $\Delta^{14}CO_2$ flux, even if the stratosphere-troposphere exchange might be increasing in response to an accelerating stratospheric circulation (or some features of) as climate changes. Rather, it is the $\Delta^{14}CO_2$ observations themselves, not the derived net isotope fluxes, that provide the constraints on the stratospheric circulation, as discussed below.

If in fact the relevant stratospheric age spectra are sufficiently wide to attenuate variations in the ^{14}C production rate due to the solar cycle and our conclusion thus remains robust as additional observations are made, long-term monitoring of $\Delta^{14}CO_2$ levels may reveal changes in the stratospheric circulation without the complicating factor of needing to take variations in the ^{14}C production rate into account. For example, comparison of observed and modeled $\Delta^{14}CO_2$ can serve as a sensitive diagnostic for evaluating stratospheric transport into, within, and out of the stratosphere in global chemistry-climate models, as we showed in Kanu *et al.* [2016]. It is also likely that simultaneous measurements of $\Delta^{14}CO_2$ – an inert tracer with a lower stratospheric source and tropospheric sink – in combination with mean age tracers like CO_2 and SF_6 – conservative tracers with increasing tropospheric sources and mesospheric sinks – could be especially useful, since mean ages and residence times are correlated but have different sensitivities to aspects of the stratospheric circulation, as shown by *Hall and Waugh* [2000; 2002]: The mean age is an average over the distribution of transit times from the tropical tropopause to a point in the stratosphere, while the residence time is an average of the distribution of transit times from a point in the stratosphere to the tropopause [*Hall and Waugh*, 2000; 2002]; they show using their simplified 'tropical pipe model' that mean ages and residence times both decrease with more rapid circulation through the system (i.e., with increases in either the tropical vertical velocity or the midlatitude vertical diffusivity in their model), with less recirculation (i.e., with less mixing of older midlatitude air back into the tropical upwelling region, known as the "detrainment flux"), and with a larger fraction of air in the tropical upwelling region. However, the sensitivity of residence times and mean ages to each of these circulation parameters can be quite different; they illustrate this both by using their tropical pipe model and by showing that different 2D and 3D stratospheric models with similar mean ages can show a wide range of residence times and vice versa. Deciphering the origin of these differences in model transport, however, is difficult. Comparing observed $^{14}CO_2$ levels and mean ages from observations (which is simply the observed time lag between the tropospheric boundary conditions for CO_2 or SF_6 and measured mixing ratios in the stratosphere) with model results may provide a means to more accurately attribute model-model and model-observation

discrepancies to specific aspects of the stratospheric circulation. Similarly, long-term observations of both $\Delta^{14}CO_2$ and mean ages from the CO_2 and SF_6 lag times together, and comparisons with models, may provide a means to detect and understand how the stratospheric circulation may be changing in response to increased radiative forcing by greenhouse gases in a manner that mean ages may not be sensitive to, such as a faster circulation in the lower stratosphere [e.g., *Engel et al.,* 2009, *Bönisch et al.*, 2011] or that mean ages alone may not unambiguously identify.

2.3.3 Vertical $\Delta^{14}CO_2$ profiles extending across the tropopause

As discussed in the previous section and shown in Figure 2.2, the SEAC4RS dataset is comprised of many vertical profiles spanning latitudes from 16.3° to 48.9°N that cover altitudes from 12 to 20 km. Two of these vertical profiles, near 29.5°N, extend down to 5 km. A single vertical profile is also available from the DC3 mission on 21 May 2012 at 35°N spanning altitudes from 1.2 to 11.9 km, shown in Figure 2.7. The number and spatial extent of these vertical profiles of $\Delta^{14}CO_2$ and their collection during major aircraft campaigns for which many other species and dynamical parameters have been measured are unprecendented and provide important constraints on the vertical distribution of stratospheric and tropospheric $^{14}CO_2$ in the Northern Hemisphere needed for inverse modeling estimates of global, hemispheric, and regional emission rates of CO_2 [e.g. *Basu et al.,* 2016; *Turnbull et al*., 2011; *Miller and Michalak,* 2017 and references within].

We can also use these observations to examine processes that affect atmospheric composition in the upper troposphere/lower stratosphere (UT/LS) from several outliers in two of the $\Delta^{14}CO_2$ profiles: one outlier from the SEAC4RS dataset is a sample collected in the stratosphere several kilometers above the tropopause that is unexpectedly depleted in $^{14}CO_2$ and one outlier from the DC3 dataset is a sample collected in the troposphere that is unexpectedly enriched in $^{14}CO_2$. These $\Delta^{14}CO_2$ observations, combined with simultaneous measurements of other trace gases and back trajectory calculations, provide insight into influences of long-range transport and local convection on the vertical distribution of $\Delta^{14}CO_2$.

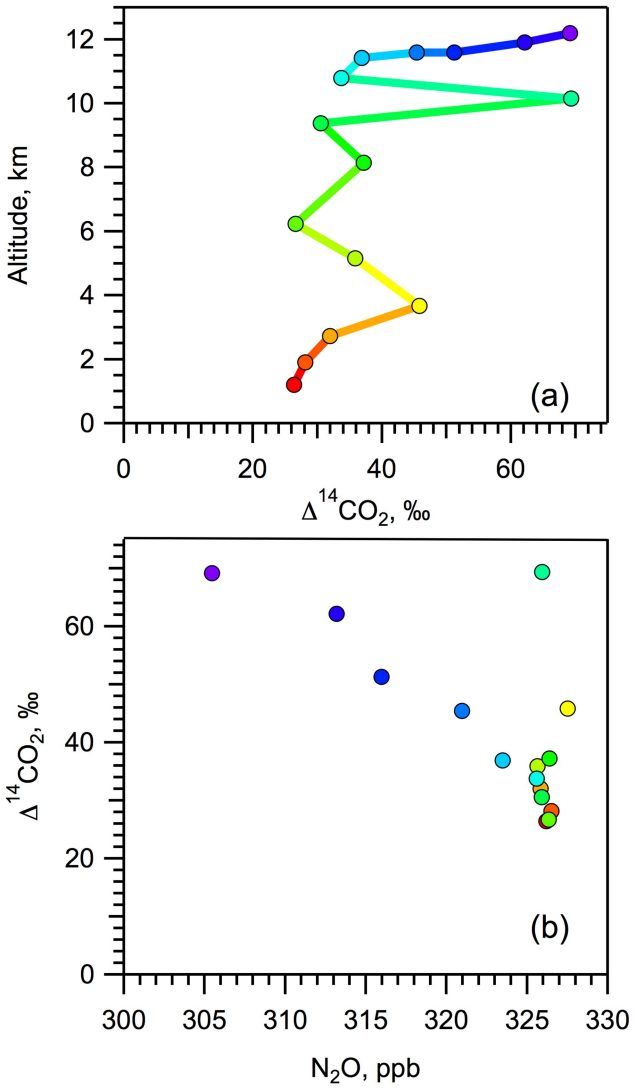

Figure 2.7 Measurements of $\Delta^{14}CO_2$ from whole air samples collected on a single vertical profile on 21 May 2012 at 35°N, 87°W during the DC3 mission. The colors evolve with time/altitude, so that individual $\Delta^{14}CO_2$ measurements may be compared in (a) altitude vs. $\Delta^{14}CO_2$ and (b) $\Delta^{14}CO_2$ vs. N_2O mixing ratio.

The SEAC4RS mission took place during the Summer and Autumn of 2013, and the sample with an anomalously low value for $\Delta^{14}CO_2$ was collected on 13 September 2013 at 17.7 km at 27.3°N and 93.8°W over the Gulf of Mexico. The low $\Delta^{14}CO_2$ value (16.3‰), which is the only purple datum above 14 km in Figure 2.2, is more typical of tropospheric air, but this sample was collected in the stratosphere, 2.7 km above the local tropopause, and at a potential temperature of 411K, well above the 380K isentropic surface delineating the stratospheric overworld. Continuous *in situ* measurements of O_3 and CO before, during, and after the collection of this sample (Figure 2.S3) show a decrease in O_3 of ~150 ppb and an increase in CO of ~10 ppb for this air sample relative to the air in the vertical profile above and below it as the ER-2 aircraft is ascending. Measurements of ethane and ethyne by GC/MS in the whole air samples show that these relatively short-lived gases (47 days and 7-12 days, respectively) would be expected to decrease as the aircraft ascends but instead they remain elevated above the expected background in this sample with low $\Delta^{14}CO_2$. Both the *in situ* and the WAS hydrocarbon measurements suggest that air in this sample recently entered the stratosphere. Moreover, because the aircraft intercepted this low-O_3, high-CO, enhanced-hydrocarbon air mass both on ascent and half an hour earlier on descent through these same potential temperature surfaces, this new air several kilometers above the tropopause appears to be quite large in extent – at least 1.5 degrees based on the latitudes of ascent and descent. While most air enters the stratosphere through the tropical tropopause [e.g. *Holton*, 1995; *Schoeberl*, 2013], convection in the subtropical and midlatitude regions of the Asian Monsoon and the North American Monsoon can also penetrate the tropopause, lofting near-surface air deep into the stratosphere [e.g., *Randel et al.,* 2010; *Park et al.*, 2007; *Pittmann et al*., 2007]. Diabatic back-trajectory calculations for air sampled in this vertical profile at potential temperatures ranging from 398 to 413K, which appear as green-yellow lines in Figure 2.8, show that air associated with this unusually low $\Delta^{14}CO_2$ sample likely entered the stratosphere above the Asian monsoon a few weeks before it was sampled. The enhanced CO mixing ratio is also consistent with local pollution from industry or biomass burning in Asia, but is rarely observed for the North American monsoon [e.g., *Randel et al.,* 2010; *Park et al.*, 2007]. Thus, while it is possible that this air entered the stratosphere via marine convection in the western Gulf of Mexico, via convection associated with Tropical Storm Ingrid in the eastern Gulf of Mexico at the time, or via mesoscale convective complexes in North America, as had been largely assumed during the SEAC4RS mission, back trajectories and other trace gas measurements suggest that this $\Delta^{14}CO_2$ outlier is most likely polluted air that was injected into the stratosphere above the Asian monsoon in August, about 2 to 4 weeks earlier. This is a case for which the features that identify the influence of long-range transport on the upper troposphere/lower stratosphere (UT/LS) were subtly present in the vertical profiles of conventional tracers O_3 and CO, but were decidedly evident in the $\Delta^{14}CO_2$ vertical profile.

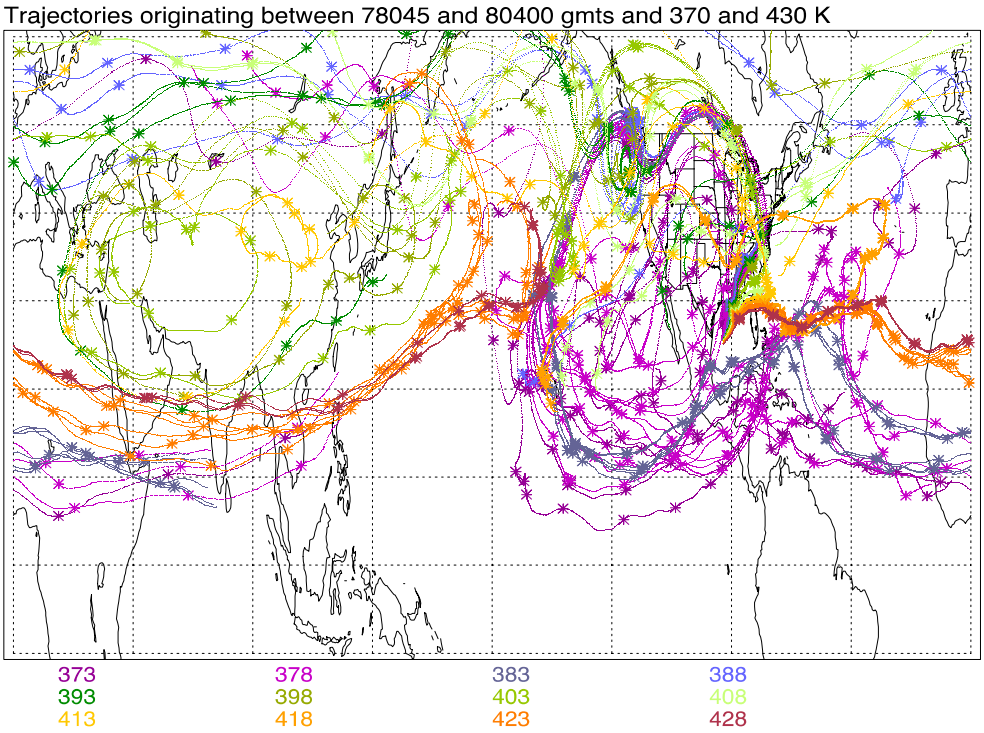

Figure 2.8 Diabatic back trajectories for air at various potential temperatures (colors) for the vertical profile sampled during SEAC4RS near 27°N and 93.8°W on 13 September 2013. Trajectories for lower and higher potential temperatures in the vertical profile do not originate in the Asian monsoon, but trajectories from 398 to 413 go to the anticyclone. The potential temperature of the sample of interest for the anomalously low value of $\Delta^{14}CO_2$ is 411 K.

While an anomalously low value of $\Delta^{14}CO_2$ was observed well above the tropopause during SEAC4RS, an anomalously high value of $\Delta^{14}CO_2$ was observed well below the tropopause during the DC3 mission. This sample was collected at 10.1 km (1.6 km below the local tropopause) at a potential temperature of 332K. $\Delta^{14}CO_2$ is greatly enriched at 69.3‰ while, given the rest of the profile, a value for $\Delta^{14}CO_2$ of only ~30‰ is expected (Figure 2.7). Continuous *in situ* measurements of ozone and water vapor show no corresponding increase in ozone or decrease in water vapor that might indicate a stratospheric intrusion or other cross-tropopause transport (Figure 2.S4). In fact, *in situ* measurements of CO are elevated by ~10 ppb relative to air sampled before and after this sample when a stratospheric intrusion should be depleted in CO. The mixing ratio of n-pentane, which has an atmospheric lifetime of 5 days, is elevated to 53 ppt for this sample compared to an average of 23 ppt for all other whole air samples from this flight. Additionally, the mixing ratio of n-pentane is larger than that of i-pentane, indicating that this sample could be influenced by emissions from biomass burning or petroleum drilling and storage. A tracer of convection – the ratio of NOx to HNO_3 [e.g. *Bertram et al.*, 2007] – indicates this air had recently experienced rapid convection, and *Barth et al.* [2015] uses this flight to illustrate the characteristics of weak, pre-frontal convection in which updrafts of 10-20 m/s served to loft boundary layer air into the upper troposphere [*Barth et al.*, 2015]. Local convection could thus have lofted surface air to 10 km where this air was then

sampled. With a stratospheric intrusion ruled out and other *in situ* and whole air sample tracer measurements consistent with convective lofting from the surface, then there are two possibilities for surface air to be so enriched in $^{14}CO_2$. First, CO_2 emissions from biomass burning can release carbon that was fixed when atmospheric $^{14}CO_2$ was higher due to nuclear weapons testing; such emissions can elevate $\Delta^{14}CO_2$ values far above the tropospheric background and have been observed in aircraft samples, at least at altitudes of 2 and 4 km [e.g., *Vay et al.*, 2011]. However, biomass burning indicators (e.g., black carbon (BC), HCN, and CH_3CN) are not elevated for this DC3 sample (Figure 2.S4). The second possibility is that the aircraft intercepted $^{14}CO_2$ emissions from a nuclear power plant or a medical waste facility [e.g., *Graven and Gruber*, 2011]. Nuclear power plants are known to episodically release $^{14}CO_2$ and $^{14}CH_4$ which can affect the local abundance of $^{14}CO_2$ [e.g., Yim, 2006]. The flight path of the aircraft happened to be over three nuclear power plants (Sequoyah: 35.2°N, 85.1°W; Brown Ferry: 34.7°N, 87.1°W; and Watts Bar: 35.6°N, 84.8°W), each of which were located between 80 and 200 km of where the enriched sample was collected. Therefore, the high radiocarbon content of this sample could be explained when locally ^{14}C-enriched CO_2 from a nuclear power plant underwent rapid convection to the upper troposphere during a storm and was intercepted by the aircraft. We speculate that nuclear power plants and other industrial activities including petroleum storage facilities which emit short-lived hydrocarbons such as the elevated n-pentane that was also measured in the high $\Delta^{14}CO_2$ sample may be co-located in this non-urban area of the Tennessee Valley. In either case, measurements of the suite of tracers discussed indicate that the high $\Delta^{14}CO_2$ air sampled below the tropopause was not the result of a stratospheric intrusion, which one might expect, but rather the result of convective outflow of an air mass unexpectedly elevated in $\Delta^{14}CO_2$.

2.4 Conclusions

New measurements of the vertical distributions of $\Delta^{14}CO_2$ for 1997, 2000, 2004, 2012, and 2013 were presented and the general relationships of $\Delta^{14}CO_2$ with altitude and N_2O mixing ratios were discussed. Global annual mean net $\Delta^{14}CO_2$ fluxes from the stratosphere to the troposphere and global ^{14}C production rates were estimated for each time period using an entirely empirical method, as previously described in *Kanu et al.* [2016], and the resulting ^{14}C production rates were the same to within the uncertainties from 1997 to 2013 and across the Northern Hemisphere extratropics in 2013. With the exception of two somewhat rare outliers to the general trend in $\Delta^{14}CO_2$ with altitude, which provided interesting insights into long and short range transport, these vertical profiles for the Northern Hemisphere summer are important new constraints to diagnose the stratospheric circulation as well as for inverse modeling studies that aim to quantify the partitioning of carbon between the atmosphere, biosphere, and oceans, and to infer regional and global fossil fuel emissions from surface measurements of $\Delta^{14}CO_2$. These $\Delta^{14}CO_2$ measurements represent the beginning of a record that could be useful in detecting and monitoring long-term changes in the Brewer-Dobson circulation as it is predicted to respond to radiative forcing associated with increasing greenhouse gas emissions and ozone depletion.

Acknowledgements

This work was supported by NASA's Upper Atmosphere Research Program (NNX13AH10G to UC Berkeley). Figure 2.8 is courtesy of Leonhard Pfister, NASA, Ames Research Center, Moffett Field, CA.

References

Andrews, A. E. et al. (2001), Mean ages of stratospheric air derived from in situ observations of CO_2, CH_4, and N_2O, *J. Geophys. Res.*, *106*(D23), 32295–32314, doi:10.1029/2001JD000465.

Appenzeller, C., J. R. Holton, and K. H. Rosenlof (1996), Seasonal variation of mass transport across the tropopause, *J. Geophys. Res. Atmos.*, *101*(D10), 15071–15078, doi:10.1029/96JD00821

Barth, M. C. et al. (2015), The deep convective clouds and chemistry (DC3) field campaign, *Bull. Am. Meteorol. Soc.*, *96*(8), 1281–1309, doi:10.1175/BAMS-D-13-00290.1.

Basu, S., J. B. Miller, and S. Lehman (2016), Separation of biospheric and fossil fuel fluxes of CO_2 by atmospheric inversion of CO_2 and $^{14}CO_2$ measurements: Observation System Simulations, *Atmos. Chem. Phys.*, *16*, 5665–5683, doi:10.5194/acp-16-5665-2016.

Bertram, T. H. et al. (2007), Direct measurements of the convective recycling of the upper troposphere, *Science*, *315*, 816–820, doi:10.1126/science.1134548.

Boering, K. A., T. Jackson, K. J. Hoag, A. S. Cole, M. J. Perri, M. Thiemens, and E. Atlas (2004), Observations of the anomalous oxygen isotopic composition of carbon dioxide in the lower stratosphere and the flux of the anomaly to the troposphere, *Geophys. Res. Lett.*, *31*, L03109, doi:10.1029/2003GL018451.

Boering, K. A., S. C. Wofsy, B. C. Daube, H. R. Schneider, M. Loewenstein, and J. R. Podolske (1996), Stratospheric mean ages and transport rates from observations of carbon dioxide and nitrous oxide, *Science*, *274*(5291), 1340-1343, doi:10.1126/science.274.5291.1340.

Bönisch, H., A. Engel, T. Birner, P. Hoor, D. W. Tarasick, and E. . Ray (2011), On the structural changes in the Brewer-Dobson circulation after 2000, *Atmos. Chem. Phys.*, *11*(8), 3937–3948, doi:10.5194/acp-11-3937-2011.

Brenninkmeijer, C. A. M., D. C. Lowe, M. R. Manning, R. J. Sparks, and P. F. J. van Velthoven (1995), The ^{13}C, ^{14}C, and ^{18}O isotopic composition of CO, CH_4, and CO_2 in the higher southern latitudes lower stratosphere, *J. Geophys. Res.*, *100*(D12), 26163–26172.

Cantrell, C. A. (2008), Technical Note: Review of methods for linear least-squares fitting of data and application to atmospheric chemistry problems, *Atmos. Chem. Phys.*, *8*, 5477–5487, doi:10.5194/acp-8-5477-2008.

Denman, K.L., G. Brasseur, A. Chidthaisong, P. Ciais, P.M. Cox, R.E. Dickinson, D. Hauglustaine, C. Heinze, E. Holland, D. Jacob, U. Lohmann, S Ramachandran, P.L. da Silva Dias, S.C. Wofsy and X. Zhang, 2007: Couplings Between Changes in the Climate System and Biogeochemistry. In: Climate Change 2007: The Physical Science Basis. Contribution of Working Group I to the Fourth Assessment Report of the Intergovernmental Panel on Climate Change [Solomon, S., D. Qin, M. Manning, Z. Chen, M. Marquis, K.B. Averyt, M.Tignor and H.L. Miller (eds.)]. Cambridge University Press, Cambridge, United Kingdom and New York, NY, USA

Denning, R. F., S. L. Guidero, G. S. Parks, and B. L. Gary (1989), Instrument description of the airborne microwave temperature profiler, *J. Geophys. Res.*, *94*(D14), 16757–16765, doi:10.1029/JD094iD14p16757.

Diskin, G. S., J. R. Podolske, G. W. Sachse, and T. A. Slate (2002), Open-path airborne tunable diode laser hygrometer, Proc. SPIE 4817, *Diode Lasers and Applications in Atmospheric Sensing*, 196, doi:10.1117/12.453736

Dutta, K. (2016), Sun, Ocean, Nuclear Bombs, and Fossil Fuels: Radiocarbon Variations and Implications for High-Resolution Dating, *Annu. Rev. Earth Planet. Sci.*, *44*, 239–275, doi:10.1146/annurev-earth-060115-012333.

Ehhalt, D. H., F. Rohrer, S. Schauffler, and W. Pollock (2002), Tritiated water vapor in the stratosphere: Vertical profiles and residence time, *J. Geophys. Res.*, *107*(D24), 4757, doi:10.1029/2001JD001343.

Engel, A. et al. (2009), Age of stratospheric air unchanged within uncertainties over the past 30 years, *Nat. Geosci.*, *2*, 28–31, doi:10.1038/ngeo388.

Flocke, F. et al. (1999), An examination of chemistry and transport processes in the tropical lower stratosphere using observations of long-lived and short-lived compounds obtained during STRAT

and POLARIS, *J. Geophys. Res.*, *104*(D21), 26625–26642, doi:10.1029/1999jd900504.
Gao, R. S., J. Ballard, L. A. Watts, T. D. Thornberry, S. J. Ciciora, R. J. McLaughlin, and D. W. Fahey (2012), A compact, fast UV photometer for measurement of ozone from research aircraft, *Atmos. Meas. Tech.*, *5*(9), 2201–2210, doi:10.5194/amt-5-2201-2012.
Graven, H. D. (2015), Impact of fossil fuel emissions on atmospheric radiocarbon and various applications of radiocarbon over this century, *Proc. Natl. Acad. Sci. U. S. A.*, *112*(31), 9542–9545, doi:10.1073/pnas.1504467112.
Graven, H. D., T. P. Guilderson, and R. F. Keeling (2012a), Observations of radiocarbon in CO_2 at La Jolla, California, USA 1992-2007: Analysis of the long-term trend, *J. Geophys. Res.*, *117*, D02302, doi:10.1029/2011JD016533.
Graven, H. D., T. P. Guilderson, and R. F. Keeling (2012b), Observations of radiocarbon in CO_2 at seven global sampling sites in the Scripps flask network: Analysis of spatial gradients and seasonal cycles, *J. Geophys. Res.*, *117*, D02303, doi:10.1029/2011jd016535.
Graven, H. D., and N. Gruber (2011), Continental-scale enrichment of atmospheric $^{14}CO_2$ from the nuclear power industry: potential impact on the estimation of fossil fuel-derived CO_2, *Atmos. Chem. Phys.*, *11*(23), 12339–12349, doi:10.5194/acp-11-12339-2011.
Greenblatt, J. B. et al. (2002), Tracer-based determination of vortex descent in the 1999/2000 Arctic winter, *J. Geophys. Res.*, *107*(D20), 8279, doi:10.1029/2001jd000937.
Hall, T. M., D. W. Waugh, K. A. Boering, and R. A. Plumb (1999), Evaluation of transport in stratospheric models, *J. Geophys. Res.*, *104*, 18815–18839, doi:10.1029/1999jd900226.
Hall, T. M., and D. W. Waugh (2000), Stratospheric residence time and its relationship to mean age, *J. Geophys. Res.*, *105*(D5), 6773–6782, doi:10.1029/1999jd901096.
Holton, J. R. (1990), On the Global Exchange of Mass between the Stratosphere and Troposphere, *J. Atmos. Sci.*, *47*(3), 392–395.
Holton, J. R., P. H. Haynes, M. E. McIntyre, A. R. Douglass, R. B. Rood, and L. Pfister (1995), Stratosphere-troposphere exchange, *Rev. Geophys.*, *33*(4), 403–439, doi:10.1029/95RG02097.
Jackman, C. H., A. R. Douglass, K. F. Brueske, and S. A. Klein (1991), The influence of dynamics on two-dimensional model results: simulations of ^{14}C and stratospheric aircraft NO_x injections, *J. Geophys. Res.*, *96*(D12), 22522-22572.
Jöckel, P., and C. A. M. Brenninkmeijer (2002), The seasonal cycle of cosmogenic ^{14}CO at the surface level: A solar cycle adjusted, zonal-average climatology based on observations, *J. Geophys. Res.*, *107*(D22), 4656, doi:10.1029/2001JD001104.
Johnston, H. (1989), Evaluation of excess C 14 and SR 90 data for suitability to test Two-dimensional stratospheric models, *J. Geophys. Res.*, *94*(D15), 18485–18493, doi:10.1029/JD094iD15p18485.
Kanu, A. M., L. L. Comfort, T. P. Guilderson, P. J. Cameron-Smith, D. J. Bergmann, E. . Atlas, S. Schauffler, and K. A. Boering (2016), Measurements and modeling of contemporary radiocarbon in the stratosphere, *Geophys. Res. Lett.*, *43*(3), 1399–1406, doi:10.1002/2013GL058740.
Kinnison, D. E., H. S. Johnston, and D. J. Wuebbles (1994), Model study of atmospheric transport using carbon 14 and strontium 90 as inert tracers, *J. Geophys. Res.*, *99*(D10), 20647–20664.
Kjellström, E., J. Feichter, and G. Hoffmann (2000), Transport of SF_6 and $^{14}CO_2$ in the atmospheric general circulation model ECHAM4, *Tellus*, *52B*, 1–18.
Levin, I., B. Kromer, M. Schmidt, and H. Sartorius (2003), A novel approach for independent budgeting of fossil fuel CO_2 over Europe by $^{14}CO_2$ observations, *Geophys. Res. Lett.*, *30*(23), 2194, doi:10.1029/2003GL018477.
Levin, I., T. Naegler, B. Kromer, M. Diehl, R. J. Francey, A. J. Gomez-Pelaez, L. P. Steele, D. Wagenbach, R. Weller, and D. E. Worthy (2010), Observations and modelling of the global distribution and long-term trend of atmospheric $^{14}CO_2$, *Tellus*, *62B*, 26–46, doi:10.1111/j.1600-0889.2009.00446.x.
Li, F., J. Austin, and J. Wilson (2008), The strength of the Brewer-Dobson circulation in a changing climate: Coupled chemistry-climate model simulations, *J. Clim.*, *21*, 40–57, doi:10.1175/2007JCLI1663.1.

Li, F., D. W. Waugh, A. R. Douglass, P. A. Newman, S. E. Strahan, J. Ma, J. E. Nielsen, and Q. Liang (2012), Long-term changes in stratospheric age spectra in the 21st century in the Goddard earth observing system chemistry-climate model (GEOSCCM), *J. Geophys. Res. Atmos.*, *117*, D20119, doi:10.1029/2012JD017905.

Luz, B., E. Barkan, M. L. Bender, M. H. Thiemens, and K. A. Boering (1999), Triple-isotope composition of atmospheric oxygen as a tracer of biosphere productivity, *Nature*, *400*, 547–550, doi:10.1038/22987.

Masarik, J., and J. Beer (1999), Simulation of particle fluxes and cosmogenic nuclide production in the Earth's atmosphere, *J. Geophys. Res.*, *104* (D10), 12099-12111, doi:10.1029/1998JD200091.

Masarik, J., and J. Beer (2009), An updated simulation of particle fluxes and cosmogenic nuclide production in the Earth's atmosphere, *J. Geophys. Res.*, *114*, D11103 doi:10.1029/2008jd010557.

McLinden, C. A., M. J. Prather, and M. S. Johnson (2003), Global modeling of the isotopic analogues of N_2O: Stratospheric distributions, budgets, and the ^{17}O–^{18}O mass-independent anomaly, *J. Geophys. Res.*, *108*(D8), 4233, doi:10.1029/2002JD002560.

Miller, S. M., and A. M. Michalak (2017), Constraining sector-specific CO_2 and CH_4 emissions in the US, *Atmos. Chem. Phys.*, *17*, 3963–3985, doi:10.5194/acp-17-3963-2017.

Minschwaner, K., R. J. Salawitch, and M. B. McElroy (1993), Absorption of solar radiation by O_2 : Implications for O_3 and lifetimes of N_2O, $CFCl_3$, and CF_2Cl_2, *J. Geophys. Res.*, *98*(D6), 10543–10561, doi:10.1029/93JD00223.

Murphy, D. M., and D. W. Fahey (1994), An estimate of the flux of stratospheric reactive nitrogen and ozone into the troposphere, *J. Geophys. Res.*, *99*(D3), 5325–5332, doi:10.1029/93jd03558.

Newman, P. A., D. W. Fahey, W. H. Brune, M. J. Kurylo, and S. R. Kawa (1999), Preface [to special section on Photochemistry of Ozone Loss in the Arctic Region in Summer (POLARIS)], *J. Geophys. Res. Atmos.*, *104*(D21), 26481–26495, doi:10.1029/1999JD900832.

Newman, P. A. et al. (2002), An overview of the SOLVE/THESEO 2000 campaign, *J. Geophys. Res.*, *107*(D20), 8259, doi:10.1029/2001jd001303.

Oberländer-Hayn, S. et al. (2016), Is the Brewer-Dobson circulation increasing or moving upward?, *Geophys. Res. Lett.*, *43*, 1772–1779, doi:10.1002/2015GL067545.

Park, J., M. K. W. Ko, C. H. Jackman, R. A. Plumb, and K. H. Sage (1998), Report of the 1998 Models and Measurements II Workshop, edited, NASA Ref. Publ.

Park, M., W. J. Randel, A. Gettelman, S. T. Massie, and J. H. Jiang (2007), Transport above the Asian summer monsoon anticyclone inferred from Aura Microwave Limb Sounder tracers, *J. Geophys. Res. Atmos.*, *112*, D16309, doi:10.1029/2006JD008294.

Park, S. Y., E. L. Atlas, K. A. Boering, P. Sunyoung, E. L. Atlas, K. A. Boering, S. Y. Park, E. L. Atlas, and K. A. Boering (2004), Measurements of N_2O isotopologues in the stratosphere: Influence of transport on the apparent enrichment factors and the isotopologue fluxes to the troposphere, *J. Geophys. Res.*, *109*, D01305, doi:10.1029/2003JD003731.

Pittman, J. V. et al. (2007), Transport in the subtropical lowermost stratosphere during the Cirrus Regional Study of Tropical Anvils and Cirrus Layers–Florida Area Cirrus Experiment, *J. Geophys. Res. Atmos.*, *112*, D08304, doi:10.1029/2006JD007851.

Plumb, R. A. (2007), Tracer interrelationships in the stratosphere, *Rev. Geophys.*, *45*, RG4005, doi:10.1029/2005RG000179.

Plumb, R. A., and M. K. W. Ko (1992), Interrelationships between mixing ratios of long lived stratospheric constituents, *J. Geophys. Res.*, *97*(D9), 10145–10156.

Podolske, J., and M. Loewenstein (1993), Airborne tunable diode laser spectrometer for trace-gas measurement in the lower stratosphere, *Appl. Opt.*, *32*(27), 5324–5333.

Podolske, J. R., G. W. Sachse, and G. S. Diskin (2003), Calibration and data retrieval algorithms for the NASA Langley/Ames Diode Laser Hygrometer for the NASA Transport and Chemical Evolution Over the Pacific (TRACE-P) mission, *J. Geophys. Res.*, *108*(D20), 8792,doi:10.1029/2002jd003156.

Prather, M. J., and E. Remsberg (1993), The atmospheric effects of stratospheric aircraft: Report of the 1992 Models and Measurements Workshop, edited, p. 1291, NASA Ref. Publ.

Prather, M. and D. Ehhalt, Atmospheric Chemistry and Greenhouse Gases, in Climate Change 2001: The Scientific Basis. Contribution of Working Group I to the Third Assessment Report of the Intergovernmental Panel on Climate Change, J.T. Houghton et al. (eds.), Cambridge University Press, New York, NY, pp. 239-287, 2001.

Randel, W. J., M. Park, L. Emmons, D. Kinnison, P. Bernath, K. Walker, C. Boone, and H. Pumphrey (2010), Asian Monsoon Transport of Pollution to the Stratosphere, *Science*, *328*(5978), 611–613.

Randerson, J. T., I. G. Enting, E. A. G. Schuur, K. Caldeira, and I. Y. Fung (2002), Seasonal and latitudinal variability of troposphere $\Delta^{14}C$: Post bomb contributions from fossil fuels, oceans, the stratosphere, and the terrestrial biosphere, *Global Biogeochem. Cycles*, *16*(4), 1112, doi:10.1029/2002GB001876.

Ryerson, T. B. et al. (1998), Emissions lifetimes and ozone formation in power plant plumes, *J. Geophys. Res.*, *103*(D17), 22569–22583, doi:10.1029/98jd01620.

Sachse, G. W., G. F. Hill, L. O. Wade, and M. G. Perry (1987), Fast-response, high-precision carbon-monoxide sensor using a tunable diode-laser absortoion technique, *J. Geophys. Res.*, *92*(D2), 2071–2081, doi:10.1029/JD092iD02p02071.

Sachse, G. W., J. E. Collins, G. F. Hill, L. O. Wade, L. G. Burney, and J. A. Ritter (1991), Airbone tunable diode-laser sensor for high-precision concentraiton and flux measurements of carbon-monoxide and methane, in *Conf on Measurement of Atmospheric Gases*, vol. 1433, pp. 157–166.

Sargent, M. R., D. S. Sayres, J. B. Smith, M. Witinski, N. T. Allen, J. N. Demusz, M. Rivero, C. Tuozzolo, and J. G. Anderson (2013), A new direct absorption tunable diode laser spectrometer for high precision measurement of water vapor in the upper troposphere and lower stratosphere, *Rev. Sci. Instrum.*, *84*(7), doi:10.1063/1.4815828.

Schauffler, S. M., E. L. Atlas, F. Flocke, R. A. Lueb, V. Stroud, and W. Travnicek (1998), Measurements of bromine containing organic compounds at the tropical tropopause, *Geophys. Res. Lett.*, *25*(3), 317–320, doi:10.1029/98gl00040.

Schauffler, S. M., E. L. Atlas, S. G. Donnelly, A. Andrews, S. A. Montzka, J. W. Elkins, D. F. Hurst, P. A. Romashkin, G. S. Dutton, and V. Stroud (2003), Chlorine budget and partitioning during the Stratospheric Aerosol and Gas Experiment (SAGE) III Ozone Loss and Validation Experiment (SOLVE), *J. Geophys. Res.*, *108*(D5), 4173, doi:10.1029/2001jd002040.

Schoeberl, M. R., A. R. Douglass, and J. Joiner (2008), Introduction to special section on Aura Validation, *J. Geophys. Res.*, *113*, D15S01, doi:10.1029/2007jd009602.

Schoeberl, M. R., A. E. Dessler, and T. Wang (2013), Modeling upper tropospheric and lower stratospheric water vapor anomalies, *Atmos. Chem. Phys.*, *13*, 7783–7793, doi:10.5194/acp-13-7783-2013.

Schroeder, J. R., L. L. Pan, T. Ryerson, G. Diskin, J. Hair, S. Meinardi, I. Simpson, B. Barletta, N. Blake, and D. R. Blake (2014), Evidence of mixing between polluted convective outflow and stratospheric air in the upper troposphere during DC3, *J. Geophys. Res.*, *119*(19), 11477–11491, doi:10.1002/2014jd022109.

SILSO, World Data Center - Sunspot Number and Long-term Solar Observations, Royal Observatory of Belgium, on-line Sunspot Number catalogue: http://www.sidc.be/SILSO/, '1989-2016', last accessed 17 April 2017

Stuiver, M., and H. A. Polach (1977), Discussion: Reporting of ^{14}C data, *Radiocarbon*, *19*(3), 355–363.

Toon, O. B. et al. (2016), Planning, implementation, and scientific goals of the Studies of Emissions and Atmospheric Composition, Clouds and Climate Coupling by Regional Surveys (SEAC^{4}RS) field mission, *J. Geophys. Res.*, *121*, 4967–5009, doi:10.1002/2015JD024297.

Turnbull, J. C. et al. (2011), Assessment of fossil fuel carbon dioxide and other anthropogenic trace gas emissions from airborne measurements over Sacramento, California in spring 2009, *Atmos. Chem. Phys.*, *11*, 705–721, doi:10.5194/acp-11-705-2011.

Vay, S. A. et al. (2011), Patterns of CO_2 and radiocarbon across high northern latitudes during International Polar Year 2008, *J. Geophys. Res.*, *116*, D14301, doi:10.1029/2011JD015643.

Waugh, D. W., and T. M. Hall (2002), Age of stratospheric air: Theory, observations, and models, *Rev.*

Geophys., *40*(4), 1010, doi:10.1029/2000RG000101.
Webster, C. R., R. D. May, C. A. Trimble, R. G. Chave, and J. Kendall (1994), Aircraft (ER-2) laser infrared-absportion spectrometer (ALIAS) for in-situ stratopsheric measurements of HCl, N_2O, CH_4, NO_2, and HNO_3, *Appl. Opt.*, *33*(3), 454–472.
Weinstock, E. M., E. J. Hintsa, A. E. Dessler, J. F. Oliver, N. L. Hazen, J. N. Demusz, N. T. Allen, L. B. Lapson, and J. G. Anderson (1994), New fast-response photofragment fluoresence hygrometer for use on the NASA ER-2 and the PERSEUS remotely piloted aircraft, *Rev. Sci. Instrum.*, *65*, 3544–3554, doi:10.1063/1.1144536.
Werner, B. et al. (2017), Probing the subtropical lowermost stratosphere, tropical upper troposphere, and tropopause layer for inorganic bromine, *Atmos. Chem. Phys.*, 17, 1161–1186 doi:10.5194/acp-2016-656.
Wiegel, A. A., A. S. Cole, K. J. Hoag, E. L. Atlas, S. M. Schauffler, and K. A. Boering (2013), Unexpected variations in the triple oxygen isotope composition of stratospheric carbon dioxide, *PNAS*, *110*(44), 17680–17685, doi:10.1073/pnas.1213082110.
Yim, M. S., and F. Caron (2006), Life cycle and management of carbon-14 from nuclear power generation, *Prog. Nucl. Energy*, *48*(1), 2–36, doi:10.1016/j.pnucene.2005.04.002.

Supplementary Materials

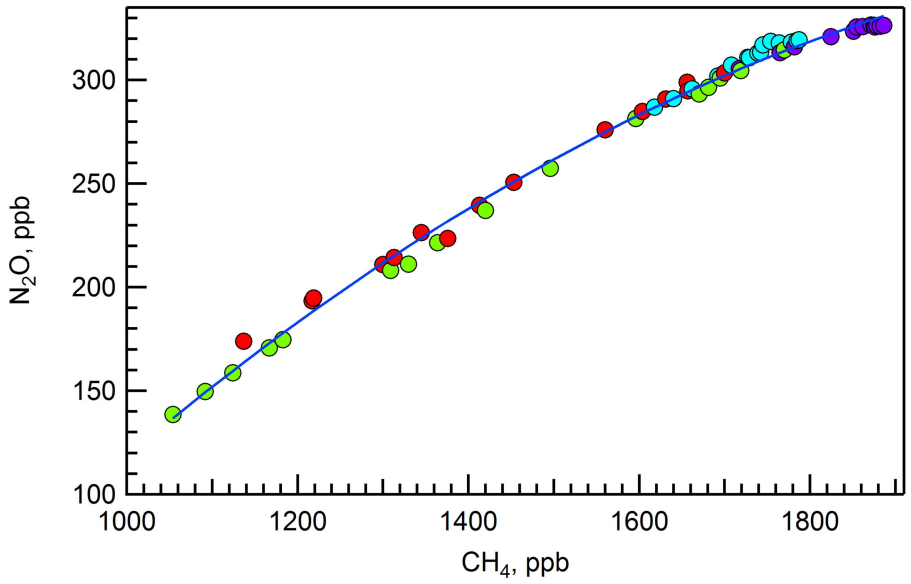

Figure 2.S1 Mixing ratios of N_2O plotted as a function of CH_4 for all samples measured for radiocarbon that have simultaneous measurements of N_2O and CH_4 mixing ratios, shown in different color circles for each campaign. A polynomial regression is shown by a blue line ($y= ax^2+bx+c$; $a = 1.22x10^{-4}$, $b=0.59$, $c= 351.8$). This regression is used to estimate N_2O mixing ratios for SEAC4RS samples, for which N_2O mixing ratios were not measured.

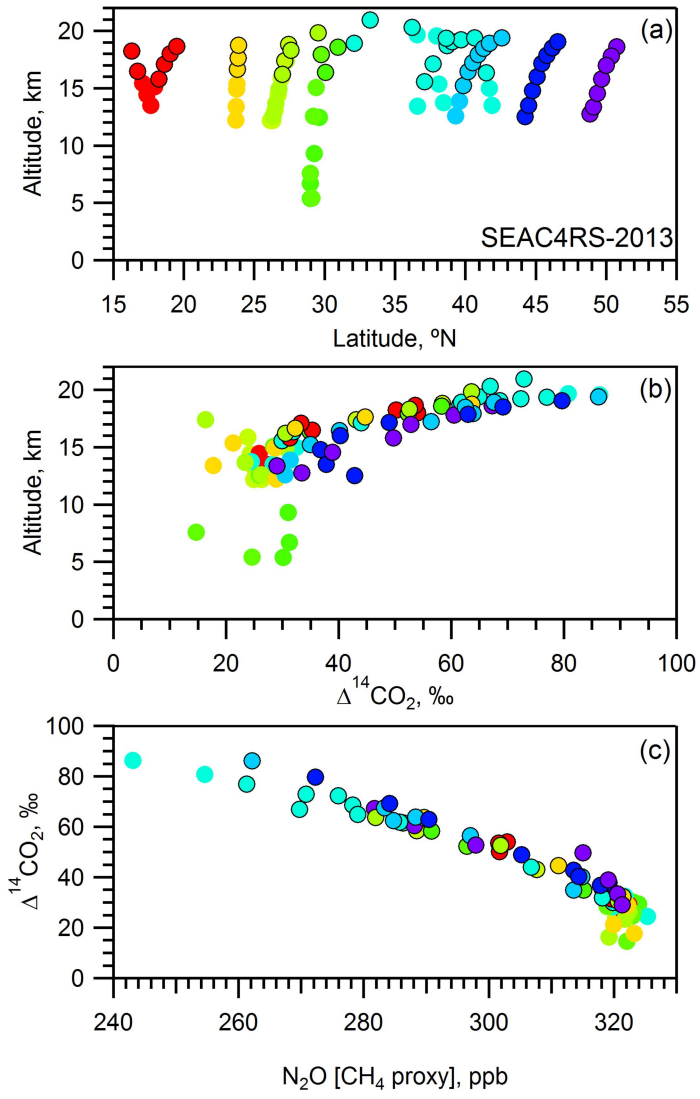

Figure 2.S2 (a) Altitude and latitude of SEAC4RS samples measured for $\Delta^{14}CO_2$ (b) Vertical profiles of $\Delta^{14}CO_2$ for SEAC4RS samples, and (c) $\Delta^{14}CO_2$ versus N_2O for SEAC4RS samples. Points of the same color are from the same vertical profile, chosen as a single ascent or descent during a flight. The points outlined in black were used to calculate a slope for the $\Delta^{14}CO_2$: N_2O correlation. The outlier discussed in section 2.3.3 has a low $\Delta^{14}CO_2$ value of 16.3‰ and is visible in panel (b) as the point above and to the left of the main cluster of data.

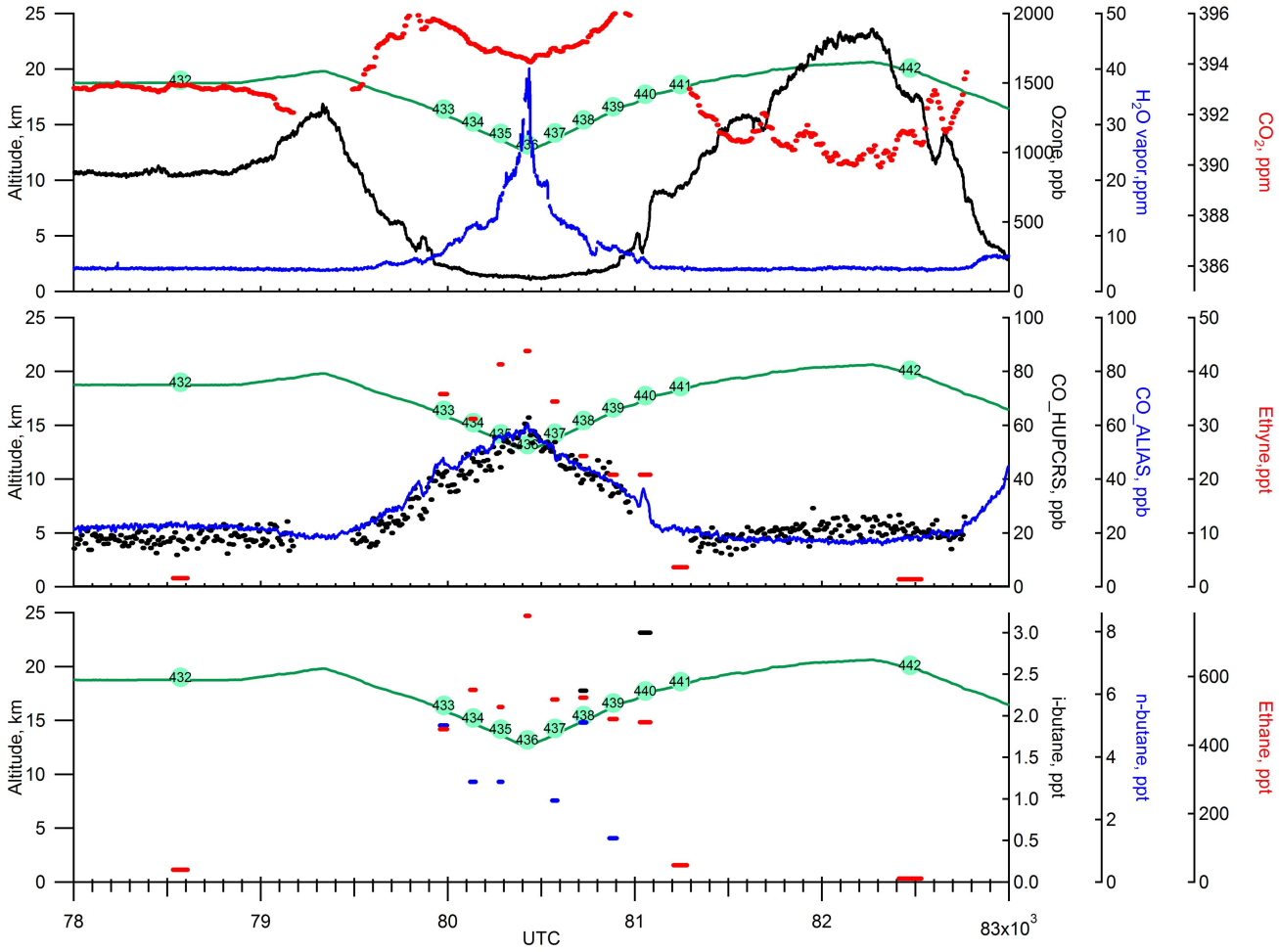

Figure 2.S3 Continuous *in situ* measurements and GC/MS measurements from whole air samples for SEAC4RS flight on 13 September 2013. Sample 440 has a lower $\Delta^{14}CO_2$ than expected. Top panel: Stratospheric indicators: O_3, H_2O, CO_2. Middle panel: CO from HUPCRS and from ALIAS and Ethyne. Bottom panel: i-butane, n-butane, ethane. A period of low-O_3 and high-CO is observed at both UTC ~79800 and 81000 s, indicating that this feature must be a large air mass that covers 1.5 degrees of latitude.

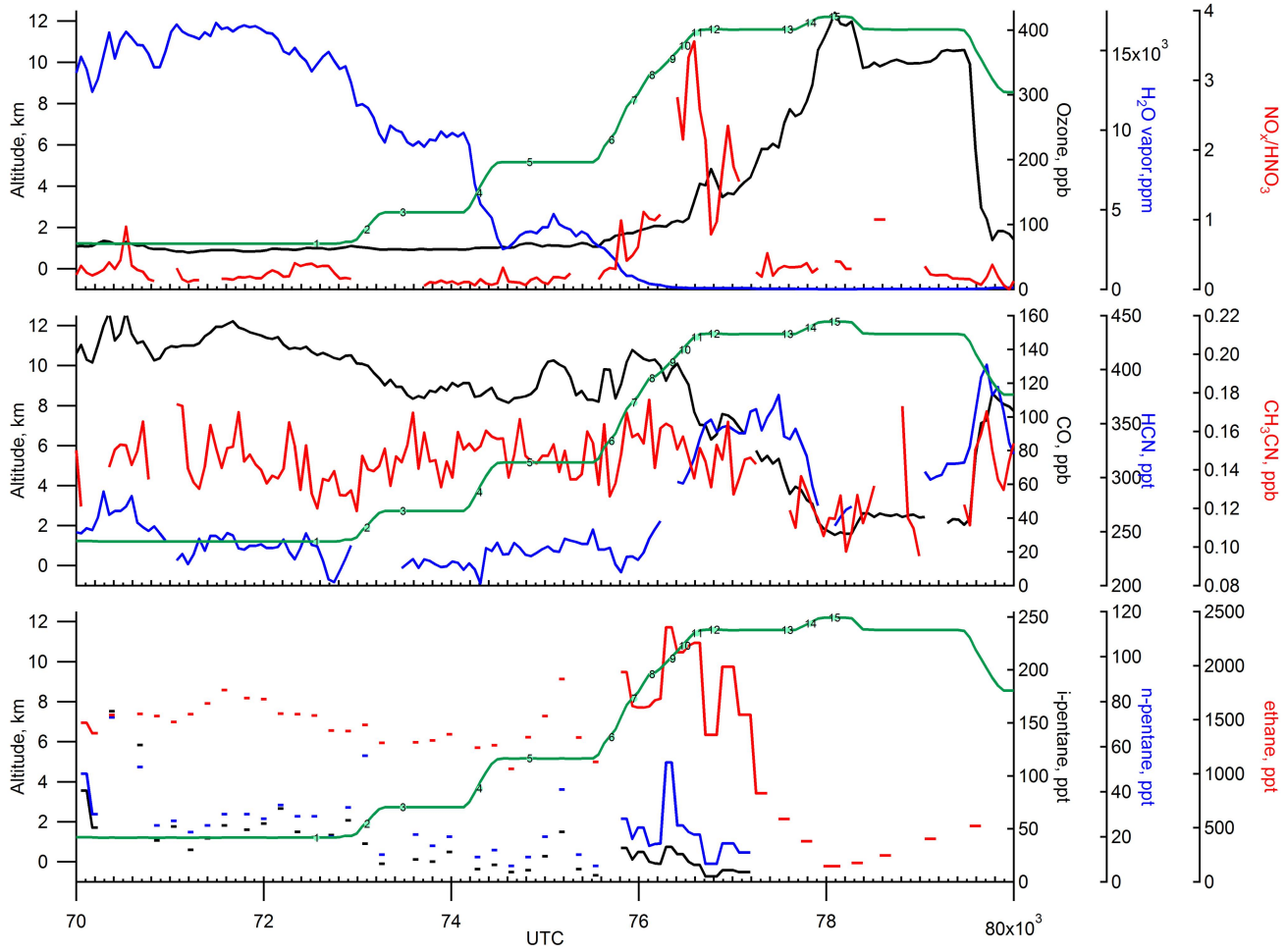

Figure 2.S4 Continuous *in situ* measurements and GC/MS measurements from whole air samples for DC3 flight on 21 May 2012. Sample 9 is more enriched in $\Delta^{14}CO_2$ than expected for its N_2O mixing ratio. Top panel: stratospheric indicators O_3 and H_2O and NO_x/HNO_3, an indicator of convection. Middle panel: Biomass burning indicators CO, HCN, and CH_3CN. Bottom panel: Short-lived hydrocarbons (lifetime): i-pentane (5 days), n-pentane (5 days), and ethane (47 days).

Table 2.ST1 Global annual mean net ^{14}C fluxes for SEAC4RS vertical profiles

Flight Number	Minimum Latitude	Maximum Latitude	Average Latitude, ˚N	Global Annual Mean Net Isotope Flux*, 10^{17} ‰ mol C yr^{-1}	N
17	16.31	19.48	18.06	2.01 ± 0.36	6
17	23.81	23.87	23.84	1.77 ± 0.26	3
16	27.01	29.54	28.05	1.54 ± 0.65	3
9	32.10	41.47	36.74	1.43 ± 0.32	5
15	37.11	39.70	38.48	1.53 ± 0.23	6
20	39.86	42.57	41.00	1.67 ± 0.22	7
20	44.23	46.57	45.32	1.67 ± 0.07	8
20	48.85	50.75	49.74	1.45 ± 0.49	7
ALL	16.31	50.74	36.44	1.50 ± 0.11	50
Lat>25N	27.01	50.74	40.04	1.49 ± 0.12	41
Lat>35N	36.22	50.74	43.45	1.48 ± 0.14	31
Lat>45N	45.09	50.74	48.10	1.59 ± 0.26	12

*2σ uncertainties are the error in slope for the $\Delta^{14}CO_2$: N_2O regression

Table 2.ST2.1 Measurements on whole air samples collected during the POLARIS mission

CAMS #	Sample Name / Flight Date (Position) / Can No.	Fraction Modern	stdev	$\Delta^{14}C^{\dagger}$	stdev	Altitude, km	Latitude, °N	Longitude, °	Pressure, mbar	Potential Temperature, K	CH_4_WAS, ppb	N_2O, ppb (ALIAS)	N_2O, ppb (ATLAS)
169285	19970908 (8) 1120	1.1891	0.0019	182.41	1.92	17.92	79.1	-133.3	76.0	464.2	1413	239.5	240.9*
169286	19970908 (13) 1244	1.1948	0.0021	188.06	2.09	18.49	84.4	-107.5	70.2	480.0	1345	226.3	224.3*
169287	19970908 (23) 2043	1.2077	0.0020	200.81	1.97	20.33	78.6	-134.3	53.0	513.4	1219	194.7	190.4*
169288	19970910 (18) 1227	1.1790	0.0027	172.31	2.71	18.06	64.4	-152.0	76.7	464.0	1453	250.5*	
169290	19970910 (23) 1061	1.1477	0.0018	141.22	1.82	15.63	64.7	-151.5	111.2	420.3	1604	284.9*	
169291	19970910 (28) 1201	1.1349	0.0018	128.48	1.83	13.29	64.8	-150.5	158.2	382.1	1657	294.7*	
169292	19970915 (3) 1003	1.1923	0.0028	185.54	2.75	19.27	64.6	-152.0	62.4	484.7	1376	223.4	233.4*
169293	19970915 (18) 1166	1.1947	0.0032	187.95	3.22	19.38	64.7	-151.9	62.0	485.5	1300	210.9	205.8*
169295	19970915 (28) 1212	1.1240	0.0018	117.64	1.82	13.31	64.8	-151.2	157.7	373.9	1700	303.5	313.0*
169296	19970918 (13) 1053	1.2080	0.0021	201.19	2.08	19.78	89.4	-147.5	55.8	504.1	1217	193.5	193.6*
169297	19970918 (23) 2013	1.2095	0.0021	202.60	2.08	20.30	79.6	-147.7	52.2	510.8	1137	174.0	173.9*
169298	19970919 (3) 1246	1.1950	0.0019	188.21	1.93	19.11	64.5	-154.6	62.3	493.9	1313	214.3	218.8*
169300	19970919 (13) 2148	1.1589	0.0020	152.36	2.03	14.32	64.5	-151.6	131.9	406.5	1560	275.9	279.8*
169301	19970919 (18) 1115	1.1391	0.0026	132.62	2.61	10.76	64.5	-150.7	219.8	346.8	1656	298.9	
172343	19970921 (28) 1085	1.1344	0.0018	127.98	1.75	19.53	23.7	-157.2	62.7	452.5	1631	290.8	
169302	19970923 (3) 2006	1.1372	0.0018	130.75	1.83	20.51	-3.3	-159.3	52.5	480.9	1627		291.6*
169303	19970923 (5) 1179	1.1321	0.0020	125.70	1.95	19.61	-2.3	-159.2	60.6	459.1	1649		300.0*
169305	19970923 (9) 1075	1.1123	0.0022	106.02	2.17	16.53	-1.1	-159.2	104.3	378.9	1711		316.5*
169306	19970923 (13) 1216	1.1105	0.0022	104.19	2.16	17.86	-0.6	-159.2	82.3	397.9	1705		312.3*
169307	19970923 (28) 2074	1.1365	0.0020	130.04	2.02	20.96	7.3	-159.2	48.7	499.5	1606		286.4*

* N_2O measurement that was used in all figures and analyses

† $\Delta^{14}C$ is reported for the date of isolation from the reservoir (Y): $\Delta^{14}C = [(F_{mod} \cdot e^{\lambda (1950-Y)}) - 1] \cdot 1000$; λ=1/8267 based on 5730 yr half-life [*Stuiver and Polach*, 1977]

Table 2.ST2.2 Measurements on whole air samples collected during the SOLVE mission

CAMS #	Sample Name Flight Date (Position) Can No	fraction modern	±	$\Delta^{14}C$	±	Pressure Altitude, km	Latitude, °N	Longitude, °	Pressure, hPa	Potential Temperature, K	CH_4_WAS, ppb	N_2O_WAS, ppb	N_2O ppb (ATLAS)
169308	19991211 (12) 2127	1.1164	0.0023	109.63	2.33	16.19	31.64	-127.74	99.87	390.33	-	-	300.9
169310	19991211 (30) 1227	1.0971	0.0023	90.46	2.25	11.24	35.04	-118.28	218.09	335.53	1795	314.5	314.6
169311	20000106 (12) 1075	1.1367	0.0027	129.85	2.65	19.58	23.97	-120.00	58.46	472.82	-	281.8	281.5
169312	20000109 (12) 1253	1.1714	0.0018	164.33	1.82	20.10	40.6	-99.60	53.90	502.00	-	210.0	211.1
169313	20000111 (10) 1179	1.1637	0.0018	156.65	1.79	19.15	48.65	-67.30	62.63	477.18	-	236.1	237.1
169314	20000111 (15) 2121	1.1442	0.0019	137.28	1.94	18.26	44.36	-70.92	72.01	465.77	-	257.1	257.4
169413	20000123 (5) 1225	1.2009	0.0019	193.69	1.93	19.60	73.47	10.66	58.30	435.83	1086	158.9	158.6
169414	20000127 (10) 1008	1.1709	0.0018	163.83	1.79	19.54	51.65	36.57	58.85	465.45	1365	220.6	221.5
169415	20000127 (25) 1129	1.1966	0.0019	189.43	1.93	19.82	66.23	22.61	56.72	444.96	1031	132.6	138.5
169416	20000127 (30) 1146	1.1272	0.0019	120.40	1.93	12.29	66.99	21.87	184.71	338.23	-	-	296.5
169418	20000131 (5) 1061	1.1969	0.0021	189.71	2.07	19.24	72.55	17.94	61.71	432.83	1151	174.8	174.6
169419	20000202 (25) 1014	1.1946	0.0021	187.37	2.05	19.30	73.98	16.81	61.14	431.05	1075.5	148.6	149.7
169420	20000203 (5) 2020	1.1992	0.0020	192.02	1.94	17.15	71.73	26.06	85.88	397.04	-	207.1	208.2
169421	20000203 (15) 1200	1.1992	0.0020	191.96	1.94	18.66	73.03	24.93	67.58	419.42	1130	167.37	170.7
169423	20000203 (25) 1114	1.1321	0.0020	125.26	1.98	14.54	68.43	24.36	129.55	360.72	-	283.9	293.3
169424	20000203 (30) 2120	1.1230	0.0023	116.25	2.26	11.71	68.29	23.40	202.47	323.98	-	-	304.5

Table 2.ST2.3 Measurements on whole air samples collected during the Pre-AVE mission

CAMS #	Sample Name Flight Date (Position) Can No	fraction modern	±	$\Delta^{14}C$	±	Altitude, km	Latitude, °N	Longitude, °	CH_4_WAS (ppbv)	N_2O (ppbv)
172344	20040119 (10) 2126	1.1057	0.0018	98.55	1.82	17.94	33.56	-82.29	1639	291.0
172345	20040119 (20) 2102	1.0827	0.0019	75.67	1.88	9.57	32.46	-81.59	1743	313.3
172346	20040119 (30) 1197	1.0919	0.0019	84.82	1.89	12.59	33.53	-83.45	1730	310.8
172347	20040119 (40) 2003	1.1073	0.0018	100.06	1.79	18.03	34.18	-86.76	1616	286.8
172348	20040121 (20) 1070	1.0930	0.0018	85.90	1.77	13.40	38.36	-96.74	1692	301.9
172349	20040121 (30) 2004	1.0973	0.0018	90.11	1.77	18.34	31.56	-95.55	1665	295.8
172350	20040124 (25) 1035	1.0775	0.0018	70.50	1.74	15.28	18.18	-84.33	1765	317.9
172351	20040124 (35) 2055	1.0848	0.0019	77.77	1.89	18.38	13.51	-82.57	1741	313.0
172353	20040127 (35) 1030	1.0807	0.0020	73.70	1.94	16.08	1.01	-84.50	1788	319.4
172354	20040129 (5) 1180	1.0819	0.0020	74.83	1.94	17.03	7.87	-85.19	1753	318.6
172355	20040129 (15) 1225	1.0834	0.0018	76.39	1.81	14.70	3.55	-87.61	1784	319.0
172356	20040130 (15) 1177	1.0814	0.0018	74.31	1.76	17.57	3.17	-87.64	1745	316.9
172357	20040130 (25) 1200	1.0808	0.0018	73.76	1.74	13.85	-0.78	-89.67	1776	318.2
172358	20040130 (45) 2062	1.0843	0.0018	77.20	1.75	18.69	6.48	-85.93	1725	310.9
172359	20040202 (45) 2088	1.0895	0.0017	82.43	1.69	17.59	26.55	-93.08	1709	307.1

Table 2.ST2.4 Measurements on whole air samples collected during the DC3 mission

CAMS #	Sample Name Flight Date ("Snake" #)	fraction modern	±	$\Delta^{14}C$	±	Altitude, km	Latitude, °N	Longitude, °	Pressure, mbar	Potential Temperature, K	CH_4 DACOM, ppb	N_2O DACOM, ppb
169425	20120521 (1401)	1.0341	0.0016	26.40	1.59	1.20	34.80	273.68	876.90	301.24	1878	326.2
169426	20120521 (1402)	1.0359	0.0016	28.14	1.59	1.89	34.94	274.16	804.96	302.02	1871	326.5
169427	20120521 (1407)	1.0344	0.0016	26.66	1.58	6.22	34.67	273.45	457.18	320.62	1875	326.3
169428	20120521 (1409)	1.0383	0.0021	30.56	2.11	9.37	34.81	273.54	290.85	328.88	1882	325.9
169429	20120521 (1412)	1.0437	0.0016	35.89	1.59	5.16	34.83	273.80	529.01	316.81	1854	325.7
169430	20120521 (1413)	1.0537	0.0016	45.81	1.61	3.66	35.25	272.99	643.52	308.79	1861	327.5
169431	20120521 (1418)	1.0398	0.0018	32.00	1.75	2.73	34.78	273.60	725.89	304.33	1862	325.9
169433	20120521 (1423)	1.0450	0.0017	37.18	1.73	8.14	34.71	273.45	348.46	326.61	1886	326.4
169434	20120521 (1801)	1.0774	0.0019	69.35	1.89	10.15	34.58	273.67	258.22	331.17	1875	325.9
169435	20120521 (1802)	1.0533	0.0022	45.43	2.17	11.59	35.11	273.38	206.26	334.74	1825	321.0
169436	20120521 (1804)	1.0772	0.0017	69.16	1.64	12.19	34.75	271.42	187.55	358.55	1717	305.5
169437	20120521 (1814)	1.0592	0.0020	51.26	2.00	11.58	34.75	272.61	206.57	338.32	1782	316.0
169438	20120521 (1816)	1.0415	0.0018	33.73	1.79	10.78	34.76	273.66	234.04	332.62	1876	325.6
169439	20120521 (1817)	1.0447	0.0018	36.89	1.80	11.42	34.81	273.38	211.88	334.43	1851	323.5
169440	20120521 (1819)	1.0702	0.0022	62.16	2.19	11.90	34.73	272.02	196.42	345.42	1765	313.2

Table 2.ST2.5 Measurements on whole air samples collected during the SEAC4RS mission

CAMS #	Sample Name Flight Date (Position) Can No	fraction modern	±	$\Delta^{14}C$	±	Altitude, km	Latitude, °N	Longitude, °	Pressure, hPa	Potential Temperature, K	Methane_WAS, ppbv
172360	20130918 (9) 1089	1.0665	0.0017	58.43	1.72	19.19	27.44	263.55	65.98	448.45	1.627
172361	20130918 (10) 1239	1.0511	0.0017	43.10	1.69	17.83	27.17	263.84	82.76	409.13	1.732
172363	20130918 (11) 3100	1.0317	0.0017	23.89	1.66	16.41	26.92	264.11	105.75	373.47	1.811
172364	20130918 (12) 1231	1.0321	0.0017	24.27	1.67	15.05	26.70	264.36	133.29	359.69	1.823
172365	20130918 (13) 2042	1.0329	0.0018	25.10	1.74	13.82	26.49	264.59	163.36	353.29	1.814
172366	20130918 (14) 3190	1.0342	0.0017	26.31	1.67	12.92	26.30	264.79	187.68	350.51	1.817
172367	20130918 (15) 2114	1.0327	0.0018	24.90	1.75	12.91	26.13	264.75	188.20	348.20	1.823
172368	20130814 (27) 1195	1.0664	0.0017	58.31	1.74	18.59	30.95	265.57	73.17	434.72	1.639
172369	20130814 (28) 3157	1.0428	0.0017	34.89	1.70	16.38	30.07	265.16	107.04	376.78	1.778
172373	20130814 (29) 1098	1.0373	0.0018	29.41	1.78	12.46	29.63	265.13	203.18	347.15	1.836
172374	20130814 (30) 1208	1.0389	0.0022	31.02	2.15	9.30	29.26	265.09	321.87	339.51	1.814
172375	20130814 (31) 2077	1.0392	0.0017	31.27	1.70	6.70	28.99	265.13	455.04	329.11	1.823
172376	20130814 (32) 3089	1.0380	0.0017	30.16	1.70	5.38	28.98	265.43	537.00	322.19	1.830
172377	20130911 (11) 3155	1.0363	0.0018	28.48	1.77	14.10	36.60	266.43	153.46	357.43	1.818
172378	20130911 (13) 2001	1.0378	0.0017	29.94	1.69	16.10	37.11	266.56	110.12	380.36	1.808
172379	20130911 (15) 2112	1.0520	0.0017	44.02	1.71	17.59	37.69	266.71	85.94	416.40	1.727
172383	20130911 (18) 1051	1.0696	0.0017	61.49	1.73	19.14	38.71	266.95	66.86	453.81	1.616
172380	20130911 (19) 1048	1.0768	0.0020	68.65	2.03	19.47	39.05	266.75	63.44	462.98	1.576
172381	20130911 (21) 1141	1.0806	0.0019	72.37	1.84	19.64	39.70	266.73	61.61	465.49	1.565
172384	20130911 (23) 1185	1.0852	0.0020	76.95	1.95	19.76	38.65	267.15	60.33	474.96	1.498
172385	20130911 (24) 2124	1.0947	0.0019	86.35	1.87	19.96	37.95	267.36	58.47	483.49	1.421
172386	20130911 (26) 3021	1.0890	0.0018	80.76	1.76	20.07	36.56	267.77	57.57	479.68	1.469
172387	20130916 (3) 1217	1.0582	0.0017	50.20	1.71	18.62	16.31	276.20	72.23	429.95	1.698

172388	20130916 (4) 3202	1.0432	0.0018	35.28	1.77	16.99	16.71	276.04	95.40	382.74	1.797
172389	20130916 (5) 1061	1.0378	0.0017	29.94	1.68	16.04	17.06	275.89	112.22	363.15	1.814
172390	20130916 (6) 1130	1.0337	0.0017	25.88	1.67	15.14	17.37	275.76	131.62	357.10	1.820
172391	20130916 (7) 3203	1.0351	0.0017	27.25	1.68	14.24	17.65	275.65	152.00	354.88	1.823
172393	20130916 (8) 1069	1.0371	0.0017	29.24	1.69	15.74	17.92	275.53	117.40	364.91	1.825
172394	20130916 (9) 3068	1.0392	0.0019	31.32	1.88	16.33	18.23	275.41	105.76	375.88	1.807
172395	20130916 (10) 1158	1.0412	0.0017	33.34	1.70	17.50	18.61	275.25	86.52	401.08	1.809
172396	20130916 (11) 3059	1.0621	0.0018	54.03	1.82	18.37	19.02	275.07	74.67	430.22	1.705
172397	20130916 (12) 1034	1.0616	0.0017	53.58	1.73	18.96	19.48	274.88	67.81	448.31	1.697
172398	20130923 (29) 1248	1.0754	0.0018	67.27	1.75	18.93	50.74	256.99	67.77	468.06	1.593
172399	20130923 (28) 2099	1.0686	0.0018	60.48	1.74	18.10	50.37	257.16	77.28	447.92	1.625
173428	20130827 (21) 2012	1.0362	0.0017	28.34	1.68	13.51	41.89	270.35	170.65	354.78	1.808
173429	20130827 (22) 1084	1.0404	0.0019	32.48	1.87	15.00	41.69	270.72	133.45	368.01	1.821
173430	20130827 (23) 1071	1.0398	0.0016	31.91	1.61	16.35	41.47	271.12	106.70	390.06	1.797
173431	20130827 (26) 2079	1.0731	0.0019	64.91	1.90	19.39	40.66	272.55	64.89	462.11	1.580
173433	20130827 (27) 1218	1.0323	0.0018	24.50	1.77	13.75	38.46	272.68	163.72	355.25	1.846
173434	20130827 (28) 2127	1.0375	0.0016	29.65	1.60	15.37	38.13	272.64	125.50	366.63	1.819
173435	20130827 (29) 2121	1.0751	0.0017	66.90	1.66	20.31	36.22	270.46	55.90	488.11	1.536
173436	20130827 (31) 2072	1.0811	0.0020	72.92	1.96	20.95	33.24	265.61	50.31	500.11	1.541
173438	20130827 (32) 3032	1.0699	0.0017	61.77	1.65	18.90	32.10	265.37	70.03	448.29	1.613
173439	20130830 (27) 1119	1.0604	0.0019	52.32	1.90	18.38	29.75	265.48	76.03	423.52	1.669
173440	20130830 (28) 1228	1.0363	0.0016	28.42	1.60	15.68	29.39	265.22	119.84	367.52	1.802
173441	20130830 (29) 3096	1.0338	0.0018	25.93	1.75	13.30	29.20	265.38	178.01	350.00	1.830
173442	20130830 (31) 2048	1.0225	0.0016	14.69	1.58	8.11	28.99	265.77	379.07	333.74	1.823
173443	20130830 (32) 3085	1.0325	0.0017	24.65	1.66	5.78	29.08	265.61	511.95	327.39	1.829
173444	20130913 (25) 2129	1.0341	0.0016	26.28	1.62	13.24	26.34	266.54	176.60	350.64	1.825
173445	20130913 (26) 1016	1.0312	0.0016	23.41	1.59	14.27	26.53	266.44	148.39	357.56	1.821
173446	20130913 (27) 1090	1.0385	0.0017	30.61	1.67	15.45	26.75	266.33	122.29	366.00	1.815
173448	20130913 (28) 1037	1.0384	0.0017	30.54	1.67	16.62	27.01	266.20	100.09	381.09	1.814

173449	20130913 (29) 3208	1.0241	0.0017	16.34	1.64	17.75	27.29	266.06	82.41	411.51	1.804
173450	20130913 (30) 1044	1.0606	0.0016	52.56	1.63	18.62	27.60	265.90	71.44	438.32	1.699
173451	20130913 (32) 2115	1.0718	0.0017	63.62	1.65	20.13	29.54	264.62	56.25	476.91	1.594
173452	20130916 (22) 1142	1.0368	0.0016	28.90	1.60	12.96	23.70	267.97	187.20	349.98	1.824
173453	20130916 (23) 3000	1.0255	0.0017	17.71	1.65	14.10	23.72	267.70	154.88	356.19	1.831
173454	20130916 (24) 1059	1.0366	0.0026	28.70	2.54	15.52	23.75	267.42	122.11	361.32	1.822
173455	20130916 (25) 1214	1.0291	0.0016	21.25	1.59	15.92	23.78	267.09	113.81	366.05	1.809
173456	20130916 (26) 1147	1.0401	0.0016	32.24	1.61	17.10	23.81	266.72	92.89	390.88	1.819
173460	20130916 (27) 3058	1.0527	0.0019	44.66	1.88	18.00	23.85	266.28	79.51	424.19	1.753
173461	20130916 (28) 2089	1.0718	0.0017	63.63	1.72	19.09	23.87	265.81	66.54	454.85	1.633
173462	20130923 (5) 2083	1.0383	0.0020	30.47	1.95	13.05	39.29	261.02	175.51	361.67	1.810
173463	20130923 (6) 1193	1.0393	0.0017	31.37	1.67	14.31	39.57	260.94	143.53	374.73	1.817
173464	20130923 (7) 1159	1.0429	0.0018	34.97	1.75	15.66	39.86	260.85	115.86	391.72	1.768
173465	20130923 (8) 1206	1.0481	0.0016	40.16	1.61	16.84	40.19	260.76	95.70	407.62	1.776
173466	20130923 (9) 1101	1.0645	0.0024	56.41	2.35	17.61	40.53	260.65	84.59	426.72	1.672
173467	20130923 (10) 1222	1.0720	0.0017	63.83	1.72	18.32	40.90	260.54	75.57	444.05	1.626
173468	20130923 (11) 3150	1.0706	0.0017	62.48	1.71	18.84	41.29	260.42	69.63	453.84	1.608
173470	20130923 (12) 1224	1.0758	0.0017	67.61	1.72	19.30	41.70	260.30	64.70	463.78	1.601
173486	20130923 (14) 3078	1.0944	0.0018	86.13	1.83	19.75	42.57	260.02	60.18	476.31	1.502
173471	20130923 (15) 2133	1.0508	0.0017	42.81	1.68	12.90	44.23	259.48	177.77	363.23	1.768
173472	20130923 (16) 2014	1.0457	0.0018	37.77	1.80	13.84	44.49	259.39	152.58	375.82	1.804
173473	20130923 (17) 2035	1.0447	0.0017	36.76	1.67	15.12	44.78	259.30	124.86	392.50	1.795
173474	20130923 (18) 1104	1.0482	0.0017	40.29	1.68	16.35	45.09	259.19	102.79	410.85	1.773
173475	20130923 (19) 1162	1.0570	0.0017	48.95	1.69	17.52	45.43	259.07	85.38	428.25	1.718
173476	20130923 (20) 2097	1.0711	0.0017	62.95	1.72	18.20	45.78	258.95	76.67	444.29	1.637
173477	20130923 (21) 1250	1.0774	0.0019	69.19	1.89	18.83	46.17	258.81	69.33	460.54	1.605
173478	20130923 (22) 1064	1.0879	0.0018	79.66	1.74	19.39	46.57	258.66	63.31	475.46	1.548
173480	20130923 (23) 1256	1.0413	0.0017	33.43	1.66	13.04	48.85	257.79	172.16	366.18	1.813
173481	20130923 (24) 1172	1.0369	0.0017	29.03	1.66	13.63	49.11	257.68	156.27	372.29	1.818

173482	20130923 (25) 3133	1.0468	0.0017	38.88	1.72	14.82	49.38	257.57	129.43	387.76	1.803
173483	20130923 (26) 3129	1.0578	0.0016	49.75	1.62	16.07	49.69	257.44	106.09	412.13	1.777
173485	20130923 (27) 1132	1.0609	0.0019	52.84	1.87	17.27	50.01	257.31	88.08	433.45	1.677

Chapter 3

The effects of stratospheric chemistry and transport on the isotopic compositions of long-lived gases measured at Earth's surface

Abstract

A number of long-lived gases in Earth's atmosphere, including carbon dioxide (CO_2), nitrous oxide (N_2O), methane (CH_4), and molecular hydrogen (H_2), become highly enriched in the rare, heavy isotopes of carbon, hydrogen, oxygen, and nitrogen in the stratosphere. These enrichments arise from the often-unique photochemical isotope fractionation occurring in the stratosphere (or from interactions with cosmic rays in the case of $^{14}CO_2$), as well as the long residence times and mean ages of stratospheric air with respect to exchange with the troposphere of up to 5 years. Transport from the stratosphere to the troposphere then enriches the gases in the troposphere in these isotopes, often offsetting the isotopically light sources of these gases at Earth's surface, such as microbial activity and fossil fuel burning. In this review, we calculate the global annual mean net isotope fluxes from the stratosphere to the troposphere using stratospheric observations of the isotopic compositions of CH_4, H_2, CO_2, and N_2O combined with simultaneous measurements of N_2O mixing ratios and independent knowledge of the global N_2O loss rate, compare the resulting isotope fluxes with previous estimates, examine the robustness of the results, and provide evidence that these isotope fluxes are in all cases large enough to affect interpretations of the global and regional concentration and isotope budgets of these gases.

3.1 Introduction

Measurements of the isotopic compositions of carbon dioxide (CO_2), nitrous oxide (N_2O), methane (CH_4), and molecular hydrogen (H_2) at Earth's surface have long been used to identify and quantify the sources and sinks of these gases, but the role of the stratosphere has yet to be fully quantified. Because the mass of air in the stratosphere is only 10% of that in the troposphere, and because large isotope effects in the photolysis or photooxidation of stratospheric gases had not yet been discovered or fully appreciated until relatively recently, most studies using isotope compositions measured at Earth's surface to constrain the magnitudes and geographic distributions of the sources of these gases to the atmosphere have ignored the possible influence of a stratospheric component, reasoning that the relatively small amount of air returning to the troposphere from the stratosphere would have a negligible impact on the isotopic composition of gases at the surface [e.g., *Fung et al.*, 1991]. Even so, measurements of the isotopic composition of some long-lived gases on a handful of stratospheric whole air samples published in the 1990s were beginning to reveal quite large isotope enrichments relative to the troposphere, including measurements of $\delta^{15}N$ and $\delta^{18}O$ of stratospheric N_2O [e.g., *Kim and Craig*, 1993; *Rahn and Wahlen*, 1997], $\delta^{13}C$ of CH_4 [e.g. *Sugawara et al.*, 1997], $\delta^{13}C$ and $\delta^{18}O$ of CO_2 [e.g., *Gamo et al.*, 1989]), and $\delta^{17}O$ and $\delta^{18}O$ of CO_2 [*Thiemens et al.*, 1995]. Motivated by these early discoveries, and as measurement techniques improved, such as the development of continuous flow isotope ratio mass spectrometry (cf-IRMS [*Brand*, 1995]) that allowed more precise measurements to be made on orders of magnitude smaller air samples, additional measurements of the isotopic composition of stratospheric gases confirmed the large isotope enrichments, and many laboratory and modeling efforts were then devoted to understanding the

nature and magnitude of the isotope effects producing these enrichments (e.g., *Saueressig et al.* [2001] and *McCarthy et al.* [2003] for CH_4; *Yung and Miller* [1997], *Kaiser et al.* [2003], and [*McLinden et al.* [2003] for N_2O).

In addition, because the observed stratospheric isotope enrichments were so large, efforts began to quantify the effect of stratospheric chemistry and transport on tropospheric isotopic compositions. Nitrous oxide was the first and arguably the simplest case since the primary sink is photolysis (90%) and photoxidation (10%) occurring only in the stratosphere, and *Kim and Craig* [1993] recognized from their two archived stratospheric samples that the stratospheric enrichments occurring most likely in the sink reactions could balance the isotopically light sources from microbial activity in soils and the oceans. Nevertheless, quantifying the isotope flux from the stratosphere required to balance the isotopically light microbial sources was stymied due to few stratospheric observations, lack of knowledge of the underlying isotope effects, and the concern (e.g., as expressed by *Rahn and Wahlen* [1997]) over the very large spread in estimates for the air mass flux from the stratosphere to the troposphere (e.g., choosing the 100 mbar surface [*Holton*, 1990] versus the 380 K potential temperature surface [*Appenzeller et al.*, 1996] results in a factor of 3 difference in calculated cross-tropopause air mass fluxes.). For methane, the relevant isotope effects in the sink reactions CH_4 + OH, Cl, and $O(^1D)$ had already been measured by the late 1990s, so efforts to quantify the influence of stratospheric chemistry on isotope compositions at Earth's surface could be investigated using 2D models in which the known isotope effects were fully implemented [e.g., *McCarthy et al.*, 2001; *Wang et al.*, 2002]; both 2D modeling studies found that tropospheric CH_4 was enriched at steady-state by about 0.5‰ by photochemistry occurring in the stratosphere, which is large enough to affect interpretations of global scale observations using 3D CTMs, as discussed in Section 3.3.1 below. For $\Delta^{17}O$ of CO_2 and δD of H_2, however, the relevant isotope effects occurring in the stratosphere are currently still not yet well enough understood that stratospheric observations can be robustly reproduced in models without parameterizations to fit the observations. In each of these cases, then, a robust means of estimating net isotope fluxes empirically from stratospheric isotope measurements – independent of whether or not all the underlying isotope effects are known and preferably with little sensitivity to the choice of air mass flux across the troposphere – is highly desirable in order to assess the extent to which stratospheric chemistry and transport can influence isotope compositions of these species measured at Earth's surface.

As reviewed here, such an empirical global mean net isotope flux can in fact be calculated from the slope of the correlation between measurements of the isotope composition of a long-lived gas and simultaneous measurements of N_2O mixing ratios, combined with independent knowledge of the global N_2O loss rate, as *Plumb and Ko* [1992] and *Plumb* [2007] have shown can be done for any two stratospheric tracers that are long-lived with respect to vertical and quasi-horizontal transport rates. We review this 'slope-equilibrium' approach to estimate the global annual mean net isotope fluxes from the stratosphere to the troposphere and update and synthesize results from previously published and new stratospheric observations, for δD and $\delta^{13}C$ of CH_4; δD of H_2; $\delta^{18}O$, $\Delta^{17}O$, and $\Delta^{14}C$ of CO_2; and $\delta^{15}N$, $\delta^{15}N^{\alpha}$, and $\delta^{18}O$ of N_2O. In each case, we also present evidence that the influence of stratospheric chemistry and transport is large enough to affect interpretations of isotopic compositions measured at the surface on annual as well as interannual and seasonal timescales.

3.2 Global annual mean net isotope fluxes: Method, observations, and results

3.2.1 The slope-equilibrium approach for estimating global annual mean net isotope fluxes

For gases that are chemically long-lived in the stratosphere relative to vertical and quasi-horizontal transport timescales (i.e., months to years), the observed compact correlation between mixing ratios of those gases is equal to the ratio of their global net vertical fluxes, as shown by *Plumb and Ko* [1992] and *Plumb* [2007]. As explained by *Plumb* [2007], the fact that chemically unrelated but long-lived species show spatially similar isopleths (surfaces of constant mixing ratio) throughout the entire stratosphere was first revealed by simultaneous measurements of CH_4 and N_2O by the Nimbus-7 SAMS satellite [*Jones and Pyle,* 1984], and led *Holton* [1986] and *Mahlman et al.* [1986] to show that these relationships are determined by a balance between the slope-steepening effect of the overturning circulation and the slope-flattening effect of quasi-horizontal mixing and thus that transport is responsible for the similar shapes of the long-lived tracer isopleths. *Plumb and Ko* [1992] then showed that the slope of the correlation between two long-lived tracers represents the ratio of the global net vertical fluxes of the two species if rapid isentropic mixing is global in extent (and which would result in there being one compact tracer:tracer relationship everywhere); they also illustrated how short-term, localized perturbations in the isopleths will still result in compact relationships for a variety of species measured by satellite, aircraft, and high-altitude balloon instruments since any local changes (e.g., short-term displacements or mixing) would affect the concentrations of each long-lived, conserved tracer the same way. Importantly, *Plumb* [2007] was then able to relax the requirement of globally compact relationships and showed that the slope of two long-lived tracers is equal to the ratio of the global net vertical fluxes in the part of the stratosphere where isentropic mixing is rapid even if that relationship does not extend through the deep tropics nor into the polar vortices. In other words, the slope of the tracer:tracer relationship in the well-mixed extratropical stratosphere still yields the ratio of their global net vertical fluxes, even if those relationships are not global in extent. In fact, *Plumb* [2007] suggests that the ability to obtain an accurate slope from observations may be more limiting than the assumptions underlying the global net flux derivation.

Even before *Plumb* [2007] demonstrated that one could obtain the ratio of the global net vertical fluxes from the tracer:tracer relationships measured in the extratropical 'surf zone' (i.e., where isentropic mixing is rapid), a number of studies have used the slope-equilibrium approach to estimate the flux of species with stratospheric sources to the troposphere by exploiting the correlation of that species with simultaneous measurements of N_2O mixing ratios. Measurements of N_2O are used because the global net vertical flux of N_2O is simply the global N_2O loss rate since 99% of N_2O loss occurs in the stratosphere and the global loss rate has been determined independently from a combination of photochemical modeling and global measurements of N_2O mixing ratios from satellites [*Minschwaner et al.*, 1993]. Thus, the net flux of any long-lived tracer can be estimated based on the observed tracer:N_2O slope. This slope-equilibrium approach has been applied to estimating net vertical fluxes of O_3 [*Murphy and Fahey*, 1994; *Olsen et al.*, 2002], NO_y [*Fahey et al.*, 1995], and meteoritic material [*Cziczo et al.*, 2001], as well as the ^{17}O anomaly in CO_2 [*Luz et al.*, 1999; *Boering et al.*, 2004] and N_2O isotopologues [*Park et al.*, 2004].

In deriving the framework for this study to obtain the net isotope fluxes from a *Plumb* slope-equilibrium approach, it is also illustrative to point out the similarities with the net isotope flux definitions used in isotope biogeochemical studies. The net isotope flux (NIF) of any species between two reservoirs, A and B, can be expressed as the product of the mass flux of that species, $F(X)_{BA}$ between A and B, and the difference between the isotopic compositions of the two reservoirs, $(\delta_B - \delta_A)$, through mass balance considerations [e.g. *Raupach*, 2001; *Fung et al.*, 1997; *Farquhar et al.*, 1993; *Cuntz*, 2003 a,b]:

$$\text{Net Isotope Flux} = F(X)_{BA} \cdot (\delta_B - \delta_A) \quad (1)$$

For transport from the stratosphere (reservoir B) to the troposphere (reservoir A), the mass flux of gas 'X' from the stratosphere to the troposphere, $F(X)_{ST}$, can be expressed as the total air mass flux from the stratosphere to troposphere, 'MF', multiplied by the mixing ratio of gas X in air exiting the stratosphere, or 'X_S'.

$$\text{Net Isotope Flux (Stratosphere to Troposphere)} = F(X)_{ST} \cdot (\delta_S - \delta_T) = MF \cdot X_S \cdot (\delta_S - \delta_T) \quad (2)$$

To find an expression for $(\delta_S - \delta_T)$, the observed compact linear relationship between the isotopic composition of gas X and the N_2O mixing ratio can be used since the slope, m, is, by definition, $(\delta_S - \delta_T)/ [N_2O_S - N_2O_T]$ where N_2O_S is the mixing ratio of N_2O in air exiting the stratosphere and N_2O_T is the mixing ratio of air in the troposphere:

$$(\delta_S - \delta_T) = m \cdot [N_2O_S - N_2O_T] \quad (3)$$

The slope m of the observed $\delta X{:}N_2O$ correlation in Equation (3) is determined in this study for $N_2O > 250$ ppbv by a Williamson-York bivariate fit, which considers the uncertainties in both the x and y data [*Cantrell*, 2008]. A similar expression for the correlation between the mixing ratios of the species of interest, X, and N_2O can be written in Equation (4).

$$(X_S - X_T) = m' \cdot [N_2O_S - N_2O_T] \quad (4)$$

The slope m′ in Equation (4) is also determined by Williamson-York bivariate fit to the stratospheric observations, similar to Equation (3) for the $\delta X{:}N_2O$ correlation.

From here, we note that the sum of the global loss rate of N_2O (L) due to photolysis and photooxidation in the stratosphere and the stratospheric growth rate (G_S, which is assumed to be 10% of the tropospheric growth rate) is equivalent to the net vertical flux of N_2O, as described in *McElroy and Jones* [1996], which itself can be expressed as the difference between the N_2O mixing ratio exiting the stratosphere and the N_2O mixing ratio in the troposphere multiplied by the mass flux of air MF through the tropopause (Equation (5)).

$$-(L+Gs) = [N_2O_S - N_2O_T] \cdot MF \quad (5)$$

Solving for the $[N_2O_S - N_2O_T]$ term in Equation (5) and substituting this expression into both Equation (3) and Equation (4), expressions for X_S and $(\delta_S - \delta_T)$ are obtained in terms of L, G_S, MF and X_T. These in turn can be substituted into Equation (2) and simplified to Equation (6).

$$Net\ Isotope\ Flux = \frac{mm'(L+Gs)^2}{MF} - m(L+Gs)X_T \quad (6)$$

In Equation (6), m is the observed slope of the $\delta X{:}N_2O$ correlation, m′ is the observed slope of $X{:}N_2O$ correlation, L is the global loss rate of N_2O due to photolysis (12.6 ± 25% TgN yr^{-1}, *Minschwaner et al.* [1993]; *Prather and Ehhalt* [2001]), G_S is the stratospheric growth rate (0.3 TgN yr^{-1}, which is 10% of tropospheric growth rate [*Denman and Brasseur*, 2007]), X_T is the global annual mean mixing ratio of species X in the troposphere (for which the annually averaged global tropospheric mixing ratios from NOAA/ESRL flask network can be found at http://www.esrl.noaa.gov/gmd/ccgg/), and MF is the global annual air mass flux between the stratosphere and troposphere.

Estimates for the air mass flux, MF, may differ by a factor of 3 or more. For example, *Appenzeller et al.* [1996] calculate an air mass flux across the 380K surface of 6.8 x 10^{17} kg air yr^{-1}, while *Holton* [1990] calculates an air mass flux across the 100 mbar surface of 2.0 x 10^{17} kg air yr^{-1}. This difference largely cancels, however, as we will demonstrate in the results in the next section: the differences in net isotope fluxes calculated using Equation (6) are only ~10 to 20% larger for the *Appenzeller* air mass flux than for the *Holton* air mass flux even though the *Appenzeller* flux is 3 times larger than the *Holton* flux. This decreased sensitivity to the actual air mass fluxes can be understood as follows: For the smaller air mass flux between the stratosphere and troposphere, air resides in the stratosphere for a longer time during which species can be isotopically enriched before being transported back into the troposphere. For the larger air mass flux, air resides in the stratosphere for a shorter period of time and air returns to the troposphere with substantially less isotopic enrichment in the species of interest. In other words, for larger MF, $(\delta_S - \delta_T)$ is smaller, while for smaller MF, $(\delta_S - \delta_T)$ is larger; their product in the net isotope flux expression in Equation (2) is approximately equal, as noted previously by *Luz et al.* [1999]. For species with larger differences between X_S and X_T, such as for CH_4 and N_2O as we show below, the difference between using the *Appenzeller* versus the *Holton* values for MF are about 10% for CH_4 and about 20% for N_2O. For H_2 and CO_2, however, for which X_S and X_T are very close to each other (to within 1% for CO_2 and even smaller for H_2), the differences are very small. In fact, when X_S is assumed to be equal to X_T, the expression in Equation (4) equates to zero and Equation (6) reduces to Equation (7),

$$Net\ Isotope\ Flux = -m[X]_{T=S}(L+Gs) \quad (7)$$

Which is the expression used for $\Delta^{14}C$ of CO_2 in *Kanu et al.* [2016] and in Chapter 2.

Uncertainties in the resulting net annual mean isotope fluxes will be discussed for each specific case below, but in general the uncertainty is the sum of the systematic uncertainty (for our application) in the N_2O loss rate of ± 25% and the uncertainty from the $\delta X{:}[N_2O]$ linear regressions, which are typically about ± 10% or smaller. Uncertainty in how well the samples represent the state of the well-mixed region of the extratropical stratosphere for each isotope and for each field measurement campaign is harder to quantify but will be discussed for each net isotope flux below, especially in the cases that multiple datasets from different time periods or from different research groups and platforms are available to compare.

3.2.2 NASA ER-2, WB57-F, and Balloon Sample Observations and Results

Using the approach outlined in Section 3.2.1 above, we use measurements of the isotopic compositions of long-lived gases in whole air samples collected by the Whole Air Sampler (WAS) aboard the NASA ER-2 and WB57-F aircraft [*Flocke et al.*, 1999] and by the Cryogenic Whole Air Sampler (CWAS) flown on a high-altitude balloon platform [*Froidevaux et al.*, 2006], along with simultaneous measurements of N_2O mixing ratios (from *in situ* instruments or on the whole air samples themselves, when available) to estimate the global annual mean net isotope fluxes from the stratosphere to the troposphere. For each isotopic species, the slopes and uncertainties of the measured $\delta X{:}[N_2O]$ and the $[X]{:}[N_2O]$ correlations for N_2O>250 ppbv – for which the slope-equilibrium relationships are linear and the samples were collected in the well-mixed extratropical stratosphere – are presented in Table 3.1. The slopes in Table 3.1 and the equations and parameters described above are used to estimate global annual mean net isotope fluxes, a summary of which is presented in Table 3.2. More specific details for each set of measurements and plots of δX versus N_2O and X versus N_2O are given in each subsection below, as well as a brief overview of the isotope fractionation mechanisms. Following the results given in this section, these net isotope flux estimates are then compared with results from other isotope datasets and model investigations as well as their possible influence on isotope compositions at Earth's surface in Section 3.3 below.

Table 3.1 Regression results of $\delta X{:}[N_2O]$ and $[X]{:}[N_2O]$ correlations for samples with $[N_2O]$>250ppb

Mission	N	Isotope Species	m*	m_std_err	b	b_std_err
STRAT, POLARIS, SOLVE	26	$\delta^{13}C$ of CH_4	–0.027	0.002	–38.65	0.61
		δD of CH_4	–0.162	0.029	–36.53	8.42
		CH_4	4.081	0.241	444.59	69.39
SOLVE	5	δD of H_2	–0.928	0.337	416.77	96.95
SOLVE	9	$\delta^{18}O$ of CO_2	–0.017	0.004	46.49	0.99
		$\Delta^{17}O$ of CO_2	–0.024	0.008	7.22	2.16
		CO_2	0.045	0.003	352.62	0.94
POLARIS	5	$\Delta^{17}O$ of CO_2	–0.022	0.002	6.64	0.50
SOLVE, POLARIS	7	$\delta^{15}N$ of N_2O	–0.051	0.006	22.63	1.69
		$\delta^{15}N^{\alpha}$ of N_2O	–0.090	0.010	44.06	2.78
		$\delta^{18}O$ of N_2O	–0.046	0.003	58.67	0.83
Balloon 2004/2005	14	$\delta^{15}N$ of N_2O	–0.049	0.002	21.57	0.55
		$\delta^{15}N^{\alpha}$ of N_2O	–0.070	0.016	37.71	4.72
		$\delta^{18}O$ of N_2O	–0.039	0.003	56.75	0.97

* Regressions performed using a Williamson-York bivariate fit [*Cantrell*, 2008]: y = mx+b; uncertainty (1σ)

Table 3.2 Summary of Global Annual Mean Net Isotope Fluxes

Isotope species	Campaign	Reference for Data	Global Annual Mean Net Isotope Flux* (*Appenzeller* Mass Flux) †		Global Annual Mean Net Isotope Flux* (*Holton* Mass Flux) †	
$\delta^{13}C$ of CH_4	STRAT, POLARIS, SOLVE	Rice, 2003	256 ± 68 (20)	‰ TgC yr^{-1}	226 ± 70 (17)	‰ TgC yr^{-1}
δD of CH_4	STRAT, POLARIS, SOLVE	Rice, 2003	1511 ± 480 (272)	‰ TgC yr^{-1}	1338 ± 489 (241)	‰ TgC yr^{-1}
δD of H_2	SOLVE	Rahn, 2003	449 ± 196 (163)	‰ TgH yr^{-1}		
$\delta^{18}O$ of CO_2	SOLVE	Wiegel, 2013	34 ± 11 (7)	‰ PgC yr^{-1}	34 ± 11 (7)	‰ PgC yr^{-1}
$\Delta^{17}O$ of CO_2	SOLVE	Wiegel, 2013	49 ± 20 (16)	‰ PgC yr^{-1}	49 ± 20 (16)	‰ PgC yr^{-1}
$\Delta^{17}O$ of CO_2	POLARIS	Boering, 2004	45 ± 11 (4)	‰ PgC yr^{-1}		
$\Delta^{14}C$ of CO_2	POLARIS, Pre-AVE, Balloon 2004 and 2005, SEAC4RS‡	Kanu, 2016; Chapter 2	1846 ± 239	‰ PgC yr^{-1}		
$\delta^{15}N$ of N_2O	POLARIS, SOLVE	Park, 2004	194 ± 56 (24)	‰ Tg N yr^{-1}	163 ± 58 (24)	‰ Tg N yr^{-1}
	Balloon 2004/2005	-	189 ± 50 (8)	‰ Tg N yr^{-1}	159 ± 52 (8)	‰ Tg N yr^{-1}
$\delta^{15}N^{\alpha}$ of N_2O	POLARIS, SOLVE	Park, 2004	344 ± 98 (39)	‰ TgN yr^{-1}	289 ± 101 (40)	‰ TgN yr^{-1}
	Balloon 2004/2005	-	272 ± 97 (66)	‰ TgN yr^{-1}	229 ± 100 (67)	‰ TgN yr^{-1}
$\delta^{18}O$ of N_2O	POLARIS, SOLVE	Park, 2004	174 ± 47 (12)	‰ TgN yr^{-1}	146 ± 48 (12)	‰ TgN yr^{-1}
	Balloon 2004/2005	-	152 ± 42 (14)	‰ TgN yr^{-1}	128 ± 43 (14)	‰ TgN yr^{-1}

* Error (1σ) includes the uncertainty in the N_2O loss rate (±25%) as well as uncertainties in the slope of the $\Delta^{14}CO_2$:N_2O relationship (±5–25%). Values in parentheses are uncertainties associated with the regression fit only.

† Global annual mean net isotope flux as calculated using the air mass flux from *Appenzeller et al.* [1996] (MF= 6.8 x10^{17} kg air yr^{-1}) or *Holton* [1990] (MF= 2.0 x10^{17} kg air yr^{-1})

‡ Average global annual mean net isotope flux from POLARIS, Pre-AVE, Balloon 2004/2005, and SEAC4RS. SOLVE was excluded because it has a significantly higher uncertainty associated with the regression compared to the other missions.

$\delta^{13}C$ and δD of stratospheric CH_4

Measurements of $\delta^{13}C$ and δD of stratospheric CH_4 from whole air samples collected by the WAS instrument aboard the NASA ER-2 aircraft during the STRAT [e.g., *Andrews et al.*, 2001], POLARIS [*Newman et al.*, 1999], and SOLVE [*Newman et al.*, 2002] missions in 1996, 1997, and 2000, respectively, versus simultaneous measurements of N_2O mixing ratios measured by the ATLAS tunable diode laser instrument [*Podolske and Loewenstein*, 1993] are shown in Figures 3.1(a) and 3.1(b), respectively, and were originally reported in *Rice et al.* [2003] and *McCarthy et al.* [2003]. The isotope measurements were made with a custom CH_4 preconcentrator followed by continuous-flow gas chromatograph combustion IRMS (GC/C/IRMS) for $\delta^{13}C$-CH_4 or by continuous-flow gas chromatograph pyrolysis IRMS (GC/C/IRMS) for δD-CH_4 [*Rice et al.*, 2001]. Figure 3.1(a) and 3.1(b) show that CH_4 becomes increasingly enriched in ^{13}C and D as it is oxidized by OH, Cl, and $O(^1D)$ in the stratosphere due to significant kinetic isotope effects (KIEs) in these sink reactions. A tabulation and discussion of all the relevant carbon and hydrogen KIEs and their temperature dependence from experiment and theory as of 2003 is given in *McCarthy et al.* [2003], and only one experimental study has appeared since that time [*Feilberg et al.*, 2005]. *McCarthy et al.* [2003] found that in a global 2D model, isotope fractionation by these three reactions in the stratosphere was largely consistent with these observations. In fact, the combined $\delta^{13}C$-CH_4 and δD-CH_4 observations and comparisons with model output were used to explore some of the larger discrepancies between laboratory KIE measurements, since model errors in the OH, Cl, and $O(^1D)$ abundances and in stratospheric transport are the same for both $\delta^{13}C$-CH_4 and δD-CH_4.

Figure 3.1 shows the compact relationships observed between the CH_4 isotopic compositions and N_2O mixing ratios [(a) and (b)] as well as between the CH_4 and N_2O mixing ratios [(c)] from which the empirical net isotope fluxes from the stratosphere to the troposphere can be derived. Using the full expression for the global annual mean net isotope flux in Equation (6) in which both the $\delta^{13}C$-CH_4:[N_2O] and [CH_4]:[N_2O] correlations (Table 3.1) and a global tropospheric CH_4 mixing ratio of 1764 ppm – the average of global annual means for 1997 and 2000 [NOAA-ESRL] – are used, the global annual mean net $\delta^{13}C$-CH_4 flux from the stratosphere to the troposphere is (256 ± 68) ‰ TgC yr^{-1} using the air mass flux across the 380K surface [*Appenzeller et al.*, 1996] – or (226 ± 70) ‰ TgC yr^{-1} using the air mass flux across the 100 mbar surface [*Holton*, 1990]; see Table 3.2. The difference in the net isotope fluxes using the two different air mass fluxes is only ~10% despite the factor of 3 difference in the air mass fluxes. In a similar manner, the isotope flux for δD-CH_4 is estimated to be (1511 ± 480) ‰ TgC yr^{-1} and (1338 ± 489) ‰ TgC yr^{-1} for the *Appenzeller* and *Holton* fluxes, respectively; see Table 3.2. Again, the difference in the net isotope flux for δD-CH_4 using the different air mass fluxes is only ~10%. We note that the global annual mean net δD-CH_4 flux does depend sensitively on the range of N_2O chosen for the δD-CH_4:[N_2O] regression due to the curvature of the δD-CH_4:[N_2O] correlation. For comparison, if we apply the slope-equilibrium method to this δD-CH_4 dataset for N_2O> 195ppb, as has frequently been the choice for earlier studies of the isotopic composition of N_2O [*Park et al.,* 2004] and for $\Delta^{17}O$ of CO_2 [*Boering et al.*, 2004], the slope is = –0.30±0.01 (1σ; N=47) compared to a slope of –0.16±0.03 (1σ; N=26), for N_2O>250 ppbv, as we prefer for this study.

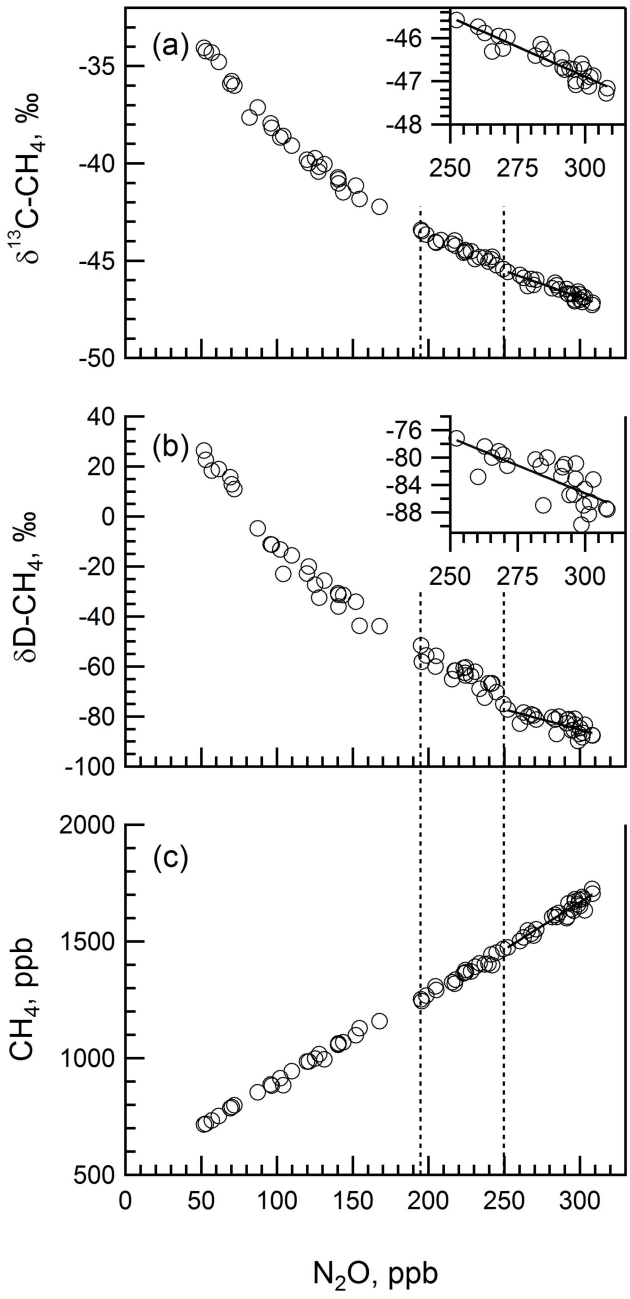

Figure 3.1 Plots of (a) $\delta^{13}C$ of CH_4, (b) δD of CH_4, and (c) CH_4 mixing ratio versus N_2O mixing ratio for the STRAT (1996), POLARIS (1997), and SOLVE (2000) missions. For the $\delta^{13}C$-CH_4:N_2O and δD-CH_4:N_2O correlations, stratospheric samples with N_2O > 250 ppb used for the global annual mean net isotope flux regression, as well as the slope of this regression, are shown in the insets. The vertical dashed lines at N_2O=195 ppb and N_2O=250 ppb indicate different N_2O limits as discussed in the main text. The curvature in the δD-CH_4:[N_2O] correlation makes the slope sensitive to the [N_2O] limits used. For example, for [N_2O] > 195 ppb, slope = –0.30 ± 0.01 (1σ; N=47); NIF (Appenzeller) = (2755 ± 114) ‰ TgC yr^{-1}(1σ; uncertainty propagated using only the uncertainty of the regression); NIF (Holton) = (2446 ± 101) ‰ TgC yr^{-1}. In comparison, when using [N_2O] > 250ppb, slope = –0.16 ± 0.03 (1σ; N=26); NIF (Appenzeller) = (1511 ± 272) ‰ TgC yr^{-1}; NIF (Holton) = (1338 ± 241) ‰ TgC yr^{-1}.

δD of stratospheric H_2

Measurements of δD of H_2 from whole air samples collected by the WAS instrument aboard the NASA ER-2 aircraft during the SOLVE mission in 2000 are shown versus simultaneous measurements of N_2O mixing ratio in Figure 3.2 and were originally reported in *Rahn et al.* [2003]. The isotope measurements were made using a nanomolar-scale off-line separation of H_2 followed by cf-IRMS that reduced sample sizes required from 40,000 liters of air to only 400 ml of air at STP [*Rahn et al.*, 2002]. Interestingly, Figure 3.2 shows that, while H_2 mixing ratios remain approximately constant, stratospheric H_2 becomes increasingly enriched in deuterium over time (i.e., as N_2O decreases, showing that air is increasingly photochemically processed as its residence time in the stratosphere increases); in fact, these are the largest deuterium enrichments measured in any material on Earth other than compounds found in very primitive meteorites. Box models [*Rahn et al.,* 2003] and global 2D models [e.g., *Mar et al.*, 2007] show that the extreme deuterium enrichment results from both the H_2 + OH sink reaction, which has a large KIE [e.g., *Ehhalt et al.*, 1989; *Talukdar et al.*, 1996], and the isotopically heavy source of H_2 from the CH_4+oxidant reactions that lead to H_2 production; indeed, that the source of H_2 from CH_4 oxidation is isotopically heavy (often referred to as "δD_{hv}") was first hypothesized by *Gerst and Quay* [2001] to balance the global H_2 and concentration budgets and was empirically demonstrated by *Rahn et al.* [2003] using the observations in Figure 3.2. The H_2 mixing ratio stays approximately constant in the troposphere and in the stratosphere up to 40 km at a mixing ratio of ~525 ppbv because the production and loss processes roughly balance one another [e.g., *Ehhalt et al.*, 1977; *Rahn et al.*, 2003], as evident in Figure 3.2(b).

Using the δD-H_2:[N_2O] correlation in Figure 3.2(a) to estimate the global annual mean δD-H_2 flux from the stratosphere to the troposphere, we note that, due to the nearly constant H_2 mixing ratio in the troposphere and stratosphere up to 40 km, we can apply Equation (7) since the approximation $X_S = X_T$ holds true. This also means that the resulting net isotope flux estimate does not depend on the air mass flux used. The slope of the δD-H_2:N_2O correlation in Figure 3.2(a) for N_2O>250 ppb (N=5) is –0.93 ± 0.34 (1σ) for SOLVE, which corresponds to an isotope flux of (449 ± 196) ‰ TgH yr^{-1}(1σ, uncertainty in both the slope and N_2O loss rate); see Tables 3.1 and 3.2. The uncertainty if we consider just the slope is 163‰ TgH yr^{-1}. For comparison, if the limits are expanded to N_2O>200 ppb, the slope is ~25% greater at –1.167 ± 0.111(1σ, N=8) and the net isotope flux is (564 ± 54) ‰ TgH yr^{-1} (1σ, slope only). As will be discussed below in Section 3.3.2, having an empirical net δD-H_2 from the stratosphere is especially useful for predicting the impact of stratospheric chemistry and transport on measurements of δD of H_2 at the surface. First, both the extreme deuterium enrichment in the stratosphere and the similar H_2 mixing ratios in the stratosphere and the troposphere (as opposed to smaller isotope enrichments and smaller values of X_S, relative to X_T, for, e.g., N_2O and CH_4,) already suggest that transport from the stratosphere will be an important term in the global H_2 isotope budget used to infer the magnitudes of the various sources and sinks of atmospheric H_2. In addition, the underlying KIEs and photolysis isotope effects producing the large deuterium enrichment in the CH_4 oxidation source are still not well understood nor well quantified empirically, including their high sensitivity to temperature, pressure, and CH_2O photolysis isotope effects, all of which vary greatly in space and time across the stratosphere and troposphere, as shown by *Mar et al.* [2007].

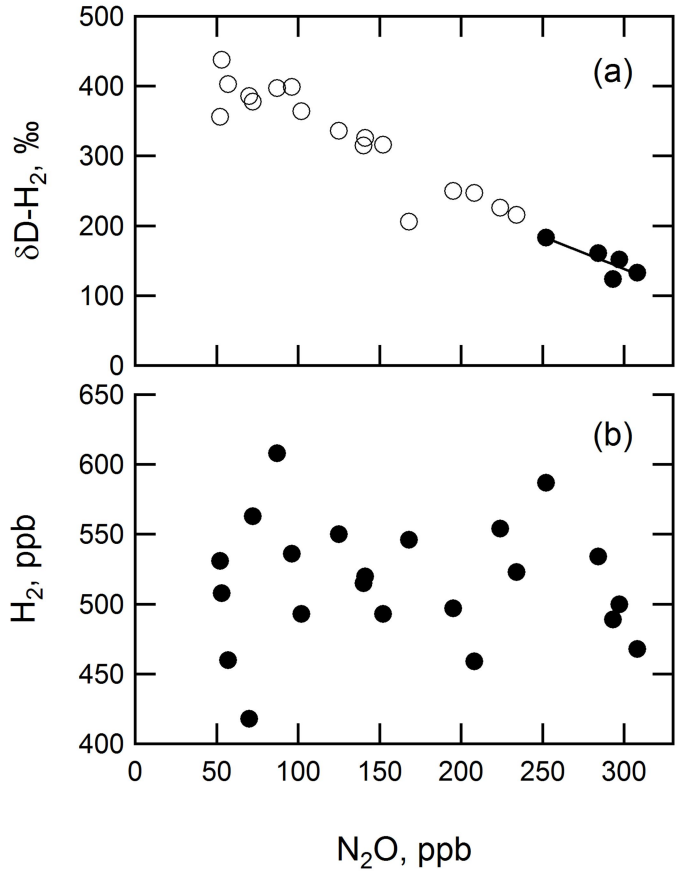

Figure 3.2 δD of H_2 versus N_2O mixing ratios from the SOLVE(2000) mission. In (a), stratospheric samples with N_2O > 250 ppb used in the isotope flux regression are shown as filled circles. In (b), molecular H_2 mixing ratios measured by mass spectrometry are relatively constant since the rates of H_2 production and loss are comparable throughout most the stratosphere.

$\delta^{18}O$ and $\Delta^{17}O$ of stratospheric CO_2

Measurements of the triple oxygen isotopic composition of CO_2 from whole air samples collected by the WAS instrument aboard the NASA ER-2 aircraft during the POLARIS and SOLVE missions are shown versus simultaneous measurements of N_2O mixing ratio in Figure 3.3(a) ($\delta^{18}O$ of CO_2 for SOLVE), Figure 3.3(b) ($\Delta^{17}O$ of CO_2 for SOLVE), and Figure 3.4 ($\Delta^{17}O$ of CO_2 for POLARIS compared with SOLVE), as first reported by *Boering et al.* [2004] for POLARIS and *Wiegel et al.* [2013] for SOLVE. For the isotope measurements, CO_2 was cryogenically separated from the whole air sample. For the POLARIS samples, $\delta^{17}O$ and $\delta^{18}O$ of CO_2 were measured by converting the CO_2 to O_2 using the BrF_5 technique and the isotopic composition of the O_2 was measured by dual inlet IRMS [*Boering et al.*, 2004]; the BrF_5 technique resulted in some mass-dependent fractionation so that the $\delta^{17}O$ and $\delta^{18}O$ values are mass-dependently scattered; thus only $\Delta^{17}O$ of CO_2 values (defined as $\Delta^{17}O = \delta^{17}O - \lambda_{MD} \cdot \delta^{18}O$, where λ_{MD} is the mass-dependent coefficient) are examined here. For the SOLVE samples, $\delta^{17}O$ and $\delta^{18}O$ were measured by the CeO_2 technique [*Assonov and Brenninkmeijer*, 2001] and dual inlet IRMS. In *Wiegel et al.* [2013], we recommended that the logarithmic form of $\Delta^{17}O$ of CO_2

be used (for which $\ln^x O = (R_{sample}/R_{standard})\cdot 1000$), but, for this study, in which the isotope variations are relatively small for N_2O>250 ppbv, we use the more common δ notation (for which $\delta^x O = (R_{sample}/R_{standard} - 1) \cdot 1000$). For consistency across the POLARIS and SOLVE datasets, here $\Delta^{17}O = \delta^{17}O - \lambda_{MD} \cdot \delta^{18}O$ was recalculated using $\lambda_{MD} = 0.528$, as in *Wiegel et al* [2013] rather than $\lambda_{MD} = 0.516$ that was used in *Boering et al.* [2004], and which is arguably preferred in general [*Meijer and Li*, 1998; *Assonov and Brenninkmeijer*, 2005]. We note that using δ versus ln notation and using $\lambda_{MD} = 0.516$ vs $\lambda_{MD} = 0.528$ makes less than a 1% difference in the resulting $\Delta^{17}O$ of CO_2 net isotope fluxes to the troposphere. For our overview and discussion purposes in this study (as to whether stratospheric chemistry and transport affect tropospheric isotopic compositions), this is a small difference; but we refer investigators who need very precise information on consistent scales to the supplementary materials which provide all the measurements needed for more precise calculations. For the $\delta^{18}O$ of CO_2 fluxes, the difference in using δ versus ln notation is about 5%.

Figures 3.3(b) and 3.4 show that stratospheric CO_2 becomes non-mass-dependently enriched in ^{17}O and ^{18}O over time (as the air is photochemically processed, evidenced by N_2O decreasing), as previous measurements have shown [e.g., *Brenninkmeijer et al.*, 1995; *Thiemens et al.*, 1995; *Lämmerzahl et al.*, 2002]. These enrichments are due to the photochemical transfer of the large and unusual non-mass-dependent KIEs in the ozone formation reaction ($O+O_2+M \rightarrow O_3$) [e.g., *Mauersberger et al.*, 2005] via isotope exchange between CO_2 and $O(^1D)$ that is produced by O_3 photolysis [e.g., *Yung et al.*, 1997; *Wiegel et al.*, 2013]. As *Wiegel et al.* [2013] demonstrate, while laboratory measurements of isotope exchange between CO_2 and O_2 via $O(^1D)$ at room temperature show remarkably good agreement with photochemical predictions using just the known ozone formation KIEs and $O+O_2$ isotope exchange reactions at room temperature, the stratospheric CO_2 enrichments still show a $\delta^{17}O/\delta^{18}O$ slope that is larger than predictions; the remaining lab-measurement discrepancies and differences observed in different regions of the stratosphere (i.e., subtropics versus extratropics) is hypothesized to be due to mass-dependent isotope effects in ozone photolysis that are larger than theoretical predictions or a temperature dependence in the formation rate coefficients for $^{17}O^{16}O^{16}O$ vs $^{16}O^{17}O^{16}O$ that has not yet been measured. Because a kinetics-only approach to calculating the ^{17}O and ^{18}O enrichments in stratospheric CO_2 in a global model is still not possible, having empirical net isotope flux estimates that allow us to test for the influence of stratospheric chemistry and transport on tropospheric values for $\Delta^{17}O$ and $\delta^{18}O$ of CO_2 is essential for applications in the troposphere.

To estimate the global annual mean net $\delta^{18}O$-CO_2 and $\Delta^{17}O$-CO_2 fluxes from the stratosphere to the troposphere for SOLVE, we use Equation (6), but for POLARIS, for which CO_2 mixing ratios were unavailable, we use Equation (7). However, since there is less than a 1% difference between CO_2 mixing ratios in the stratosphere and the troposphere and the value of m′ is small, there is a negligible difference in using Equation (6) compared to using Equation (7) for SOLVE. For $\delta^{18}O$-CO_2, the global annual mean net $\delta^{18}O$-CO_2 flux is (34 ± 11) ‰ PgC yr^{-1}. For $\Delta^{17}O$-CO_2, the global annual mean net $\Delta^{17}O$-CO_2 flux (with λ=0.528 and using δ-notation) is (49 ± 20) ‰ PgC yr^{-1} (16 ‰ PgC yr^{-1} of the stated uncertainty is from the fit of the slope) for SOLVE and (45 ± 11) ‰ PgC yr^{-1} (4 ‰ PgC yr^{-1} of the stated uncertainty is from the fit of the slope) for POLARIS. These values will be discussed in Section 3.3.3 below in the context of another stratospheric dataset and their influence on tropospheric CO_2 isotopic compositions.

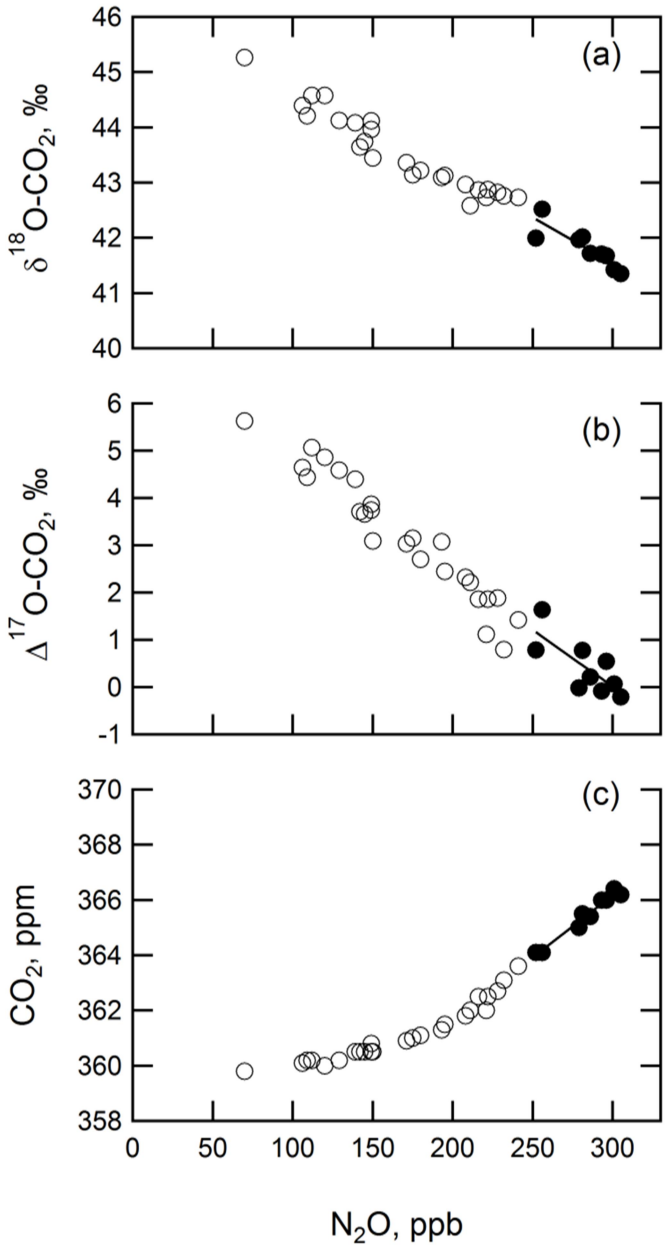

Figure 3.3 For the SOLVE mission in 2000, (a) $\delta^{18}O$ of CO_2 (b) $\Delta^{17}O$ *of* CO_2 and (c) CO_2 mixing ratio as a function of N_2O mixing ratio. Stratospheric samples with $N_2O > 250$ ppb used for the net isotope flux regression are shown as filled circles.

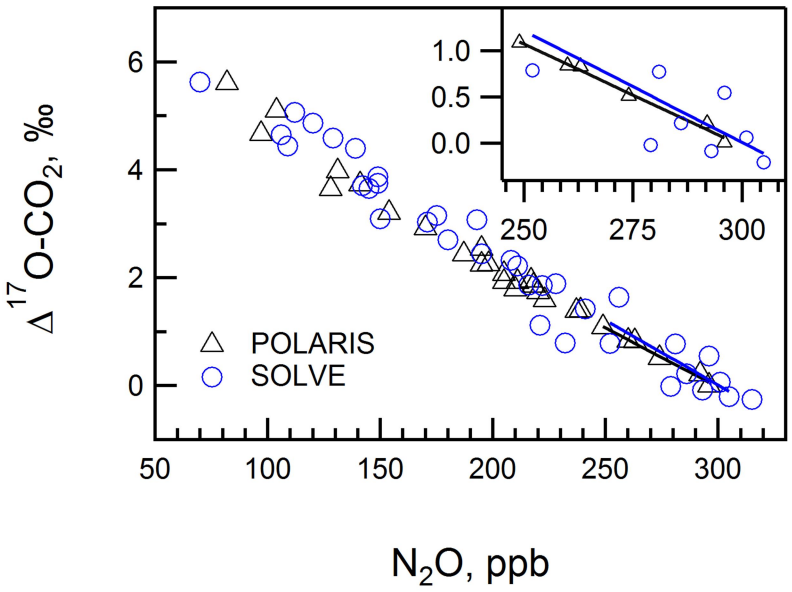

Figure 3.4 $\Delta^{17}O$ of CO_2 for POLARIS (1997; *Boering et al.* [2004]; black triangles) and SOLVE (2000; *Wiegel et al*. [2013]; blue circles) versus N_2O mixing ratio. Stratospheric samples with N_2O > 250 ppb used for the global annual mean net isotope flux regression, as well as the regression line, are shown in the inset. For SOLVE, m = –0.024±0.01 (1σ; N=9), giving an isotope flux of (49 ± 16) ‰ PgC yr^{-1}. For comparison, for POLARIS, m = –0.022±0.02 (1σ; N=5), giving an isotope flux of (45 ± 4) ‰ PgC yr^{-1}. The stated uncertainties are uncertainties in the slope only.

$\Delta^{14}C$ of stratospheric CO_2

Measurements of $\Delta^{14}C$ of CO_2 from whole air samples collected by the WAS instrument aboard the NASA ER-2 or WB57-F aircraft during the POLARIS (1997), SOLVE (2000), Pre-Ave (2004), and SEAC4RS (2013) missions, as well as from the CWAS instrument flown on high-altitude balloon platforms in 2004 and 2005 are shown versus simultaneous measurements of N_2O mixing ratio in Figure 3.5. For the isotope measurements, CO_2 was cryogenically separated from the whole air samples and stored in flamed-off glass ampoules for long-term storage. The purified CO_2 was then graphitized prior to analysis at the Center for Accelerator Mass Spectrometry at Lawrence Livermore National Laboratory; $\Delta^{14}C$ values are reported here as geochemical samples [*Stuiver and Polach,* 1977] (corrected assuming $\delta^{13}C$ of 8‰ V-PBD), with a 1σ precision of 2‰. As discussed in detail in Chapter 2 and apparent in Figure 3.5, $\Delta^{14}CO_2$ increases as N_2O decreases as ^{14}C is slowly produced from nuclear spallation reactions between ^{14}N and thermal neutrons resulting from the penetration of galactic cosmic rays into the lower stratosphere and upper troposphere and builds up over time. Additionally, year-to-year, CO_2 mixing ratios are increasing and $^{14}CO_2$ levels are decreasing due to fossil fuel combustion, which releases radiocarbon-free CO_2. Comparison of stratospheric $\Delta^{14}CO_2$ measurements and simulated $\Delta^{14}CO_2$ from a 3D chemical transport model in Kanu *et al*. [2016] showed that $^{14}CO_2$ is very sensitive to the stratospheric circulation and, thus, may serve as a tracer to identify changes in the stratospheric circulation as well as a diagnostic tool for evaluating the

stratospheric circulation and stratospheric residence times in models. Additionally, now that much of the ^{14}C produced by above-ground nuclear weapons testing in the 1950s and 1960s has been sequestered into long-term reservoirs, knowledge of the natural cosmogenic production rate of radiocarbon and subsequent transport of $^{14}CO_2$ from the stratosphere to the troposphere is becoming increasingly important in studies that use $^{14}CO_2$ measurements at the surface to quantify carbon sources and sinks including fossil fuel emissions [e.g., *Randerson et al.*, 2002; *Turnbull et al.*, 2009]. The empirical estimates presented in Chapter 2 and reviewed here provide valuable information about the influence of ^{14}C production and transport from the stratosphere on $\Delta^{14}CO_2$ measurements at the surface.

Figure 3.5(b) shows the $\Delta^{14}CO_2$:N_2O correlations for POLARIS, SOLVE, Balloon 2004 and 2005 flights, Pre-AVE, and SEAC4RS for N_2O>250 ppbv. Global annual mean net isotope flux estimates for each year are discussed in Chapter 2 and the average for all sampling years, excluding SOLVE (for reasons discussed in Chapter 2) is (1846 ± 239) ‰ PgC yr^{-1}. This empirical isotope flux is useful for carbon cycle studies that use ^{14}C as a tracer as well as for studies that use $\Delta^{14}CO_2$ to infer fossil fuel emission on regional and global scales.

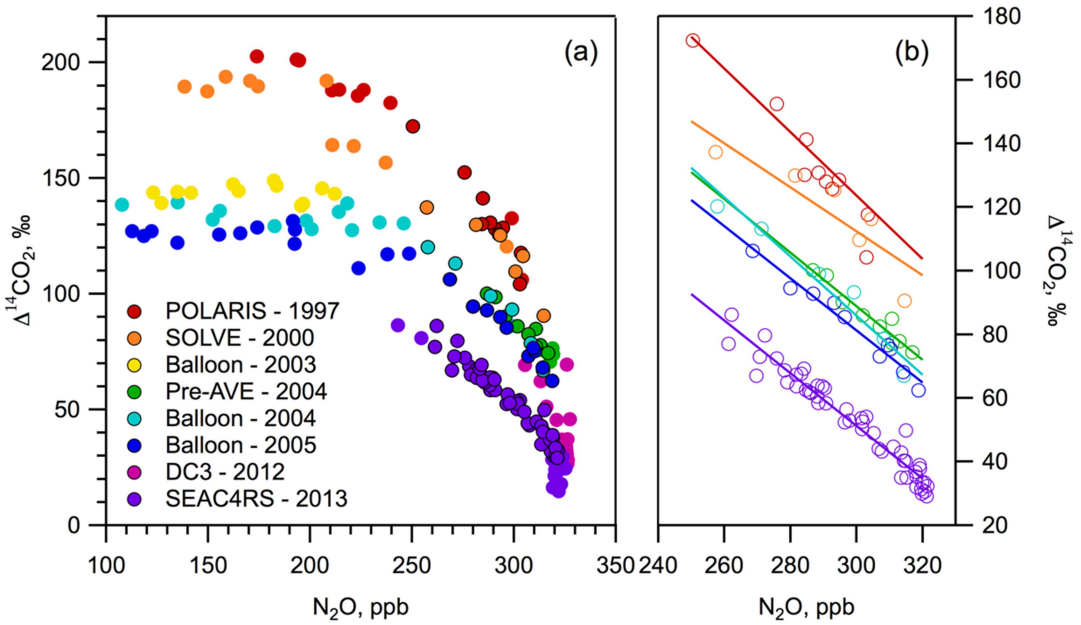

Figure 3.5 $\Delta^{14}C$ of CO_2 measurements from Chapter 2. In (a), the stratospheric data points for which 250<N_2O<320 ppbv are outlined in black and were used to determine the slope of the $\Delta^{14}CO_2$: N_2O relationship for calculating the global annual mean net $\Delta^{14}CO_2$ flux from the stratosphere to the troposphere and the global ^{14}C production rate. In (b), the stratospheric data points are shown with the regression line.

$\delta^{15}N$, $\delta^{15}N^{\alpha}$, and $\delta^{18}O$ of stratospheric N_2O

Measurements of $\delta^{15}N$, $\delta^{15}N^{\alpha}$ (i.e., the isotopic composition at the α, or middle atom position in N_2O), and $\delta^{18}O$ of N_2O from whole air samples collected by the WAS instrument

aboard the NASA ER-2 aircraft during the POLARIS and SOLVE mission in 1997 and 2000, respectively, versus simultaneous measurements of N_2O mixing ratios measured by the ATLAS tunable diode laser instrument [*Podolske and Loewenstein*, 1993; *Hurst et al.*, 2000] for POLARIS and by GC/MS for SOLVE [*Schauffler et al.*, 2003] are shown in Figures 3.6, 3.7, and 3.8, respectively, as originally reported in *Park et al.* [2004]. The isotope measurements were performed by IRMS operated in continuous flow mode coupled with an online preconcentrator and gas chromatograph [*Park et al.*, 2004, 2012; *Croteau et al.*, 2010]. In addition, new isotope measurements for $\delta^{15}N$, $\delta^{15}N^{\alpha}$, and $\delta^{18}O$ of N_2O are presented here from whole air samples collected during balloon flights in 2004 and 2005 (as described in *Kanu et al.* [2016] for $\Delta^{14}CO_2$ measurements) using the same IRMS instrumentation as for the POLARIS and SOLVE aircraft samples.

Figures 3.6, 3.7, and 3.8 show that, as N_2O is destroyed by photolysis and by photoxidation by $O(^1D)$, the remaining N_2O becomes increasingly enriched in ^{15}N and ^{18}O, as shown previously by *Kim and Craig* [1993], *Rahn and Wahlen* [1997], *Toyoda et al.* [2001], and *Röckmann et al.* [2003b], as well as by the data shown here from *Park et al.* [2004]. Indeed, *Kim and Craig* [1993] used isotope measurements on two archived stratospheric air samples to first suggest that large isotope effects in the stratospheric sink could balance the isotopically light sources to yield the measured isotopic composition of N_2O measured in the troposphere. Subsequent laboratory experiments and theoretical calculations [e.g., *Kaiser et al.*, 2002; *Röckmann et al.*, 2003; *Yung et al.*, 2004; *Schmidt et al.*, 2011] and incorporation of the underlying isotope effects in a global 3D model [*McLinden et al.*, 2003] have shown that photolysis in the stratosphere – N_2O's primary sink – enriches the remaining N_2O in both ^{15}N and ^{18}O; the tails of the UV absorption cross-sections for the heavy isotopologues ($^{15}N^{14}N^{16}O$, $^{14}N^{15}N^{16}O$, $^{14}N^{14}N^{18}O$) are blue-shifted slightly out of the solar window for N_2O photolysis in the stratosphere relative to the light isotopologue ($^{14}N^{14}N^{16}O$). The enrichment at the central nitrogen atom position (the α position) is much larger than at the terminal nitrogen atom position (the β position) or the average over the two positions (simply $\delta^{15}N$), largely because it is the N–O bond that is broken in N_2O photolysis.

Comparing the POLARIS and SOLVE data with the new balloon N_2O isotope data in Figures 3.6–3.8, we note that all the N_2O isotope:N_2O correlations are compact for $N_2O > 200$ ppbv. This similarity at higher N_2O values was discussed extensively by Park *et al*. [2004] in comparison with the other N_2O isotope studies referenced above; air with N_2O mixing ratios less than 200 ppbv is either found at higher altitudes in the stratosphere or at low altitudes in the stratosphere after air has descended from much higher altitudes in the polar vortex, and hence can reflect very different chemical and transport histories. In fact, *Plumb* [2007] also describes such differences in long-lived tracer correlations in general starting at ~180 ppbv of N_2O, and, again, these differences are due to differences in the chemical and transport histories. As Park *et al.* [2004] show and discuss, the lower values for the N_2O isotope compositions sampled by the ER-2 aircraft during POLARIS (Figures 3.6–3.8) represent very old air that had descended in the polar vortex the previous winter/spring and then mixed with air at lower altitudes, which accounts for it being even further removed from the idealized Rayleigh fractionation line due to the extensive mixing it has experienced. The more tropical the air, the more Rayleigh-like, and, hence, the higher the value for the isotopic composition for a given N_2O mixing ratio for $N_2O < 200$ ppbv; this is evident in the two distinct sets of N_2O isotope:N_2O correlations in the

balloon dataset, one more tropical and one more midlatitude-like. Pragmatically, and for our purposes here, we note that the global annual mean net isotope fluxes can be calculated from the linear regime for N_2O>200 ppbv that is remarkably uniform across all the datasets measured to date.

Using Equation (6) with m′ = 1 and the N_2O isotope:N_2O correlations in Figures 3.6–3.8, the global annual mean net isotope fluxes can be derived and compared for POLARIS and for the new balloon dataset. The difference between the results for the *Appenzeller* versus the *Holton* air mass fluxes is about 15 to 20%, a slightly larger difference than for the CH_4 isotope results since there is a larger difference between X_S (i.e., the mixing ratio of species X in air exiting the stratosphere) and X_T (i.e., the mixing ratio of species X in air entering the stratosphere from the tropical troposphere) for N_2O than for CH_4. In Section 3.3.4 below, these net isotope fluxes for N_2O are compared with other data sets and with model results, and their influence on the isotopic composition of tropospheric N_2O is discussed.

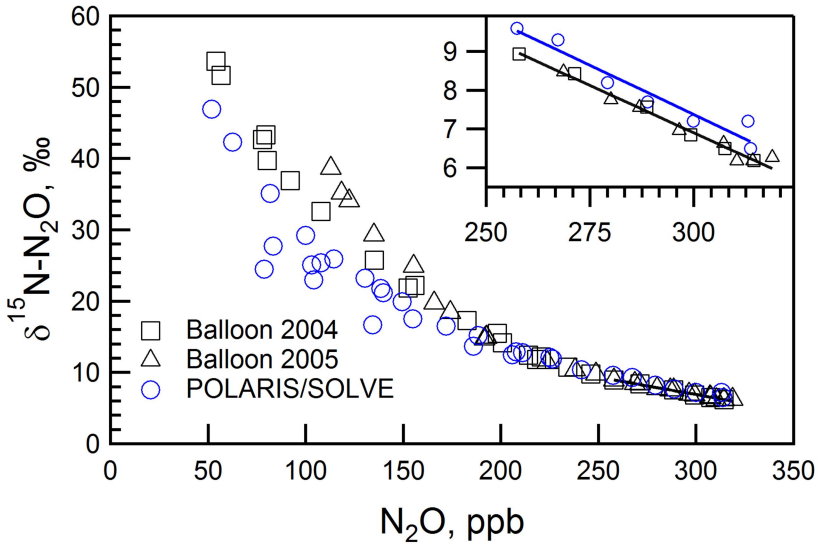

Figure 3.6 $\delta^{15}N$ of N_2O versus N_2O for samples from balloon flights at 34°N over Fort Sumner, NM in 2004 (black squares) and 2005 (black triangles) and from POLARIS (1997) and SOLVE (2000) aircraft missions in *Park et al*., 2004 (blue circles). Stratospheric samples with N_2O > 250 ppb used for the net isotope flux regression, as well as the regression line, are shown in the inset. The slopes of the correlations are very comparable; –0.051 ± 0.006 (1σ; N=7) for POLARIS/SOLVE and –0.049 ± 0.002 (1σ; N=14) for Balloon 2004/2005 resulting in global annual mean net isotope fluxes of (194 ± 24) ‰ TgC yr^{-1} and (189 ± 8) ‰ TgC yr^{-1}, respectively (*Appenzeller* mass flux; 1σ in slope only).

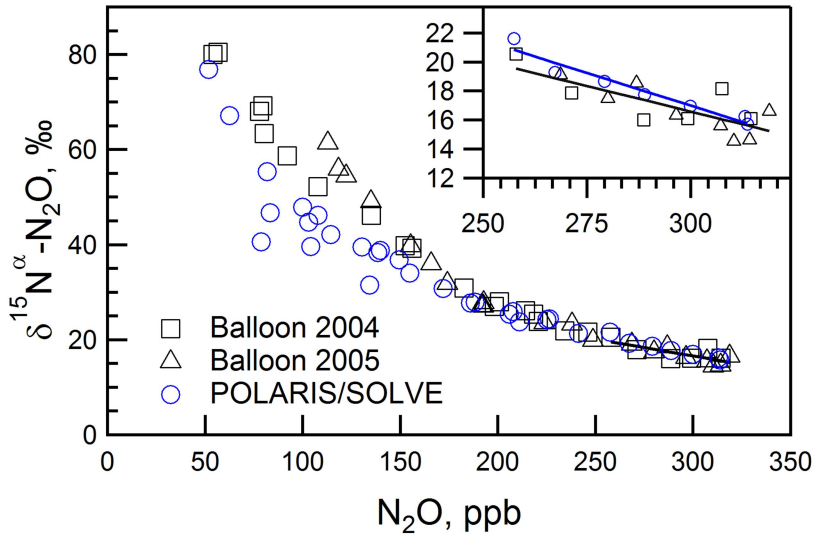

Figure 3.7 $\delta^{15}N^{\alpha}$ of N_2O for balloon flights in 2004 and 2005 and POLARIS/SOLVE, as in Figure 3.6. The slopes of the correlations are –0.090 ± 0.010 (1σ; N=7) for POLARIS/SOLVE and –0.070 ± 0.016 (1σ; N=14) for Balloon 2004/2005 resulting in global annual mean net isotope fluxes of (344 ± 39) ‰ TgC yr^{-1} and (272 ± 66) ‰ TgC yr^{-1}, respectively (*Appenzeller* mass flux; 1σ in slope only).

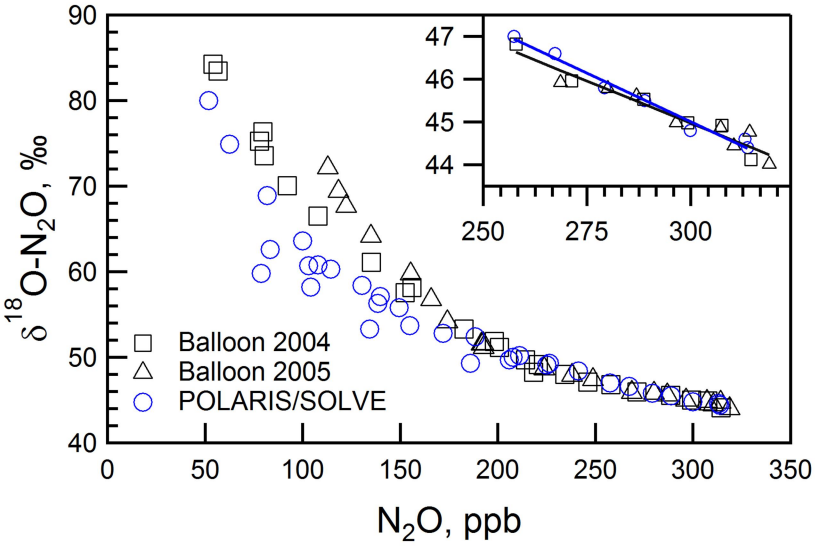

Figure 3.8 $\delta^{18}O$ of N_2O for balloon flights in 2004 and 2005 and POLARIS/SOLVE, as in Figure 3.6. The slopes of the correlations are quite similar: –0.046 ± 0.003 (1σ; N=7) for POLARIS/SOLVE and –0.039 ± 0.003 (1σ; N=14) for Balloon 2004/2005 resulting in global annual mean net isotope fluxes of (174 ± 12) ‰ TgC yr^{-1} and (152 ± 14) ‰ TgC yr^{-1}, respectively (*Appenzeller* mass flux; 1σ in slope only).

3.3 Discussion

Given the large enrichments in the rare, heavy isotopes in CH_4, H_2, CO_2, and N_2O that occur in the stratosphere, transport of these highly enriched gases from the stratosphere to the troposphere – even after dilution with isotopically lighter tropospheric air – may influence surface isotopic compositions and interfere with using surface measurements to infer, for example, the relative magnitudes of natural versus anthropogenic sources of these gases. In this section, we compare the global annual mean net isotope flux estimates in Table 3.2 with estimates from other observations and from modeling studies, when available (see Table 3.3). We also provide some estimates and comparisons that suggest that, even in cases for which the annual mean net isotope flux from the stratosphere to the troposphere is small compared to other components of the isotope budget, the stratospheric influence may not be negligible as previously assumed, especially relative to, for example, interhemispheric gradients or seasonal cycles in isotopic compositions measured at the surface.

3.3.1 δD and $\delta^{13}C$ of CH_4

Methane is the most abundant non-CO_2 greenhouse gas in the modern atmosphere and comes from myriad sources at the surface including agriculture and fossil fuels. Because its global warming potential is 28 times greater than that of CO_2 on the 100-year time horizon [e.g., *Stocker et al.*, 2013] and it has a much shorter global lifetime of 9.1 ± 0.9 years [*Prather et al.*, 2012], CH_4 is a good target for emission legislation because curtailing methane emissions would quickly reduce its large contribution to radiative forcing. Isotope compositions of methane are increasingly being used to identify its atmospheric sources and how they may be changing over time [*Kai et al.*, 2011; *Kirschke et al.*, 2013; *Rice et al.*, 2016; *Saunois et al.*, 2016a, 2016b; *Schaefer et al.*, 2016; *Schwietzke et al.*, 2016]. Even though the amount of methane returning to the troposphere from the stratosphere is a small component of the overall methane budget (~9 Tg CH_4 yr^{-1}), the large enrichments in ^{13}C and D may mean that the global annual mean net isotope fluxes can have a non-negligible effect on methane isotope measurements at Earth's surface. In *McCarthy et al.* [2001], we compared results from LLNL's 2D model LOTUS for the steady-state $\delta^{13}C$ composition of tropospheric CH_4 in which the relevant CH_4 oxidation KIEs had been included to model results in which the KIEs were all set to 1 and found that the ^{13}C enrichments in the stratosphere and transport to the troposphere results in a +0.6‰ enrichment in tropospheric $\delta^{13}C$-CH_4. Similarly, we find that using the net $\delta^{13}C$-CH_4 isotope flux in Table 3.2 in a two-box (stratosphere-troposphere) model of CH_4 sources and sinks enriches tropospheric CH_4 by +0.5‰ relative to that without a net flux of enriched CH_4 from the stratosphere. For comparison, the interhemispheric gradient from 41°S to 71°N in $\delta^{13}C$-CH_4 is –0.5‰ and the seasonal amplitude at 60°N is 0.4‰ [*Quay et al.*, 1999]. Thus, at steady-state and in a well-mixed troposphere, the influence of the stratosphere on tropospheric $\delta^{13}C$-CH_4 is as large as the interhemispheric gradient and the seasonal cycle at high latitudes, which are important constraints for 3D inverse models that aim to quantify the various CH_4 sources [e.g., *Houweling et al.*, 2016]. We also used 2D model results from LOTUS with and without the hydrogen KIEs for CH_4 oxidation in the stratosphere as well as a two-box model for δD-CH_4 using the global annual mean net isotope flux from the stratosphere to the troposphere in Table 3.2. In both cases, the effect of transport of the stratospheric enrichments in deuterium in CH_4 and its transport to the troposphere increased tropospheric δD-CH_4 by +5–10‰, which is also as large as the interhemispheric gradient in δD-

CH_4 values at the surface. Furthermore, the few other stratospheric CH_4 isotope measurements available [*Sugawara et al.*, 1997; *Röckmann et al.*, 2011] are in close enough agreement that we do not expect these conclusions to change – that is, that isotope fractionation in the stratosphere and the return of air to the troposphere may be large enough to alter the magnitudes and/or distributions of CH_4 sources inferred from inverse models that do not account for such a stratospheric influence.

3.3.2 δD of H_2

There is great interest in determining the current sources and sinks of atmospheric H_2 so that if hydrogen fuel cells replace combustion as a major energy source for, e.g., transportation, the effects of potentially large increases in anthropogenic H_2 emissions on the oxidation capacity of the troposphere and stratospheric ozone can be better predicted [e.g. *Pieterse et al.*, 2011; *Tromp et al.*, 2003; *Warwick et al.*, 2004; *Feck et al.*, 2008; *Jacobson*, 2008]. Measurements of the isotopic composition of H_2 have played a key role in deciphering the identity and magnitudes of its sources and sinks [e.g., *Gerst and Quay*, 2001; *Rahn et al.*, 2003; *Rhee et al.*, 2006]. Because the deuterium enrichments in stratospheric H_2 are so large (Figure 3.2 above as well as balloon observations from *Röckmann et al.*, [2003a]), it seems likely that transport from the stratosphere will influence δD-H_2 values measured at Earth's surface. Similar to the McCarthy *et al.* [2001] box model results for δ^{13}C-CH_4 described above, the global annual mean net δD-H_2 flux from the stratosphere to the troposphere with a value similar to that in Table 3.2 was used to estimate the influence of stratospheric chemistry and transport on tropospheric δD-H_2 at steady state and found that transport to the troposphere increased tropospheric δD-H_2 by +10–15‰, a substantial enrichment which is also as large as the interhemispheric gradient in δD-H_2 values at the surface [*Gerst and Quay*, 2001].

For comparison, a large number of samples (N=123) were collected in the lowermost stratosphere aboard commercial aircraft flights as part of the CARIBIC program between 15° and 90°N in May 2009 and measured for δD-H_2 [*Batenburg et al.*, 2012]. The global annual mean net δD-H_2 flux from the stratosphere to the troposphere that we estimated using the slope-equilibrium method with the δD-H_2:N_2O correlation they report (see Table 3.3) is twice as large as the one we derived from the SOLVE mission measurements in Figure 3.2 above. While it is unclear why there is a factor of two discrepancy at this time (Batenburg et al. [2012] speculates an inconsistent interlaboratory comparison and/or the influence of a sampling bias toward the lowermost stratosphere for the CARIBIC data compared to the wider altitude range available to stratospheric aircraft), a net δD-H_2 flux twice as large would mean an even larger effect on tropospheric δD-H_2 of +20–30‰ than the +10–15‰ estimated with our box model. In fact, this is closer to the value of +29‰ that is required in the TM5 model study of *Pieterse et al.* [2011] to resolve the H_2 isotope budget and achieve δD-H_2 values similar to observations. An even larger value of +37‰ is required in the GEOS-chem Chemical Transport Model [*Price et al.*, 2007]. These results all suggest that transport from the stratosphere may influence δD-H_2 values at the surface. A more recent modeling study using δD-H_2 and H_2 mixing ratio measurements from the EuroHydros project and the CARIBIC program and with new parametrizations for surface deposition of H_2 showed a range of stratospheric contributions to tropospheric values, ranging from –137‰ to +59‰, with the "most realistic model results" being 0‰, meaning that while tropospheric H_2 budget in the current version of their model is most sensitive to

uncertainties in H_2 deposition [*Pieterse et al.*, 2013], the uncertainties appear large.

3.3.3 $\delta^{18}O$, $\Delta^{17}O$, and $\Delta^{14}C$ of CO_2

Measurements of the oxygen isotopic composition of CO_2 have long been used to partition the relative contributions of various sources and sinks in the carbon cycle and how they may be changing over time. The $\delta^{18}O$ isotope composition of tropospheric CO_2 is largely governed by the competing processes of photosynthetic uptake and respiration, and so has been used to estimate gross carbon fluxes between the atmosphere and biosphere [*Farquhar et al.*, 1993; *Ciais et al.*, 1997; *Cuntz*, 2003a,b; *Welp et al.*, 2011]. Attempts to quantify the degree to which stratospheric CO_2, enriched in ^{18}O, influences tropospheric isotopic compositions have been made [e.g., *Cuntz,* 2003a,b], and the empirical estimate in Table 3.2 and in *Kawagucci et al.* [2008] provide important comparisons. The value for the global annual mean net $\delta^{18}O$-CO_2 flux from the stratosphere to the troposphere in Table 3.2 of (34 ± 11) ‰ PgC yr^{-1} is in good agreement with the global annual mean net isotope flux reported in *Kawagucci et al.* [2008] of (38 ± 11) ‰ PgC yr^{-1}. Although these are smaller than some terms in the tropospheric $\delta^{18}O$-CO_2 isotope budget, they are not negligible.

The ^{17}O anomaly in CO_2 (or $\Delta^{17}O$ of CO_2) has only more recently been proposed as a tracer of the global carbon cycle. *Hoag et al.* [2005] used a two-box model to explore the relative contributions of production of the ^{17}O anomaly in the stratosphere and its flux to the troposphere and destruction or dilution by various surface carbon fluxes in the biosphere. We proposed that knowing the isotope flux from the stratosphere, combined with measurements of tropospheric $\Delta^{17}O$ of CO_2, could be used to infer gross primary productivity (which destroys the $\Delta^{17}O$ anomaly produced in the stratosphere), similar to studies of $\delta^{18}O$ of tropospheric CO_2 but without its dependence on the isotopic composition of rainwater and of water in the chloroplasts of leaves [e.g., *Farquhar et al.*, 1993], which are difficult to model on a global scale. For the Hoag study, the net isotope fluxes from the POLARIS mission that were reported in *Boering et al.* [2004] were used. In the update and re-evaluation here and comparison with the more recently reported SOLVE observations, the values for the global annual mean net $\Delta^{17}O$-CO_2 fluxes for the POLARIS and SOLVE missions are (45 ± 11) and (49 ± 20) ‰ PgC yr^{-1}, respectively. The value for POLARIS is slightly different from the value of (43 ± 11) ‰ PgC yr^{-1} reported in *Boering et al.* [2004] because, here, we limit the linear regression to points with N_2O mixing ratio greater than 250 ppb rather than 195 ppb and use λ_{MD} = 0.528 instead of 0.516. These are all similar to the value of (48 ± 14) ‰ PgC yr^{-1} reported in *Kawagucci et al.* [2008] for stratospheric balloon samples. As we showed in *Hoag et al.* [2005], transport from the stratosphere does not just affect interpretations of isotope observations at Earth's surface, it provides a new tracer of gross carbon fluxes to compare with other approaches.

Measurements of the sudden increase and slow decline of $^{14}CO_2$ in the atmosphere due to nuclear weapons testing and its subsequent movement throughout the Earth system have long been used to study the partitioning of carbon in and among its oceanic, terrestrial, and atmospheric reservoirs, yielding rich insights into CO_2 exchange rates, transport, and carbon residence times [e.g., *Guilderson et al.*, 2000; *Randerson et al.*, 2002]. Now, however, radiocarbon levels in the stratosphere are primarily governed by the rate of natural cosmogenic production and the rates and details of $^{14}CO_2$ transport to the troposphere. Studies of carbon

cycling need a better understanding of the transport of cosmogenic radiocarbon from the stratosphere to the troposphere. From the $\Delta^{14}CO_2$:N_2O correlations for POLARIS, the Balloon 2004 and 2005 flights, Pre-AVE, and SEAC4RS shown in Figure 3.5, we derived an empirical estimate of the annual mean net isotope flux of (1846 ± 239) ‰ PgC yr^{-1} (Table 3.2). As discussed in Chapter 2, we do not a detect solar cycle dependence for the net isotope fluxes from the stratosphere to the troposphere. This greatly simplifies accounting for the influence of transport from the stratosphere on carbon cycle studies at the surface, including those that infer regional and global fossil fuel emissions from surface or near-surface observations [e.g.., *Riley et al.*, 2008; *Graven et al.*, 2012; *LaFranchi et al.*, 2013; *Beramendi-Orosco et al.*, 2015; *Graven*, 2015], especially now that the major anthropogenic perturbation to atmospheric $^{14}CO_2$ levels is fossil fuel combustion [e.g., *Levin et al.*, 2010].

3.3.4 $\delta^{15}N$, $\delta^{15}N^{\alpha}$, and $\delta^{18}O$ of N_2O

Nitrous oxide is a greenhouse gas and, now that chlorofluorocarbon (CFC) concentrations have decreased, the largest stratospheric ozone depleting substance (ODS) emitted as a result of human activities [*Ravishankara et al., 2009*]. With an increase of 0.3% yr^{-1} and positive climate feedbacks, it is imperative that we continue to gain a better mechanistic understanding of the N_2O sources and sinks in order to more reliably predict future atmospheric concentrations and their effect on climate and stratospheric O_3 depletion. Measurements of the isotopic composition of N_2O can provide such additional mechanistic information. For example, measurements of atmospheric N_2O isotope compositions can serve to reduce the large uncertainties in inverse modeling studies of N_2O concentrations that are being used to determine the magnitude, timing, and geographic distribution of N_2O sources to the atmosphere. Inverse modeling efforts pursued by multiple groups [*Röckmann et al.*, 1998; *Hirsch et al.*, 2006; *Huang et al.*, 2008; *Saikawa et al.*, 2014; *Thompson et al.*, 2014a, 2014b; *Bergamaschi et al.*, 2015] show that STE is the largest uncertainty in their analyses. Since, as noted above, isotopic compositions of N_2O from the stratosphere versus those for N_2O emitted from oceanic and terrestrial sources are so different, the addition of N_2O isotope observations to inverse modeling studies and empirical checks on the magnitude of the isotope flux from the stratosphere to the troposphere can help disentangle the effects of the stratosphere from the effects of N_2O emissions. From the slope-equilibrium method, we estimate the global annual mean net isotope fluxes for $\delta^{15}N$, $\delta^{15}N^{\alpha}$, and $\delta^{18}O$ of N_2O (Table 3.2) which are in remarkable agreement with the isotope fluxes approximated by –εL in the 3D model presented by *McLinden et al.* [2003] and shown in Table 3.3. The comparable values obtained by the full implementation of stratospheric isotope effects and by the completely empirical method from N_2O isotope: N_2O correlations, again points to the value of this empirical tool in estimating the global annual mean isotope fluxes from measurements alone. Finally, we note that, unlike some of the other species explored in this chapter, there is no question that stratospheric chemistry and transport greatly affect the background tropospheric N_2O isotope composition, with the stratospheric sink balancing the isotopically light sources, as *Kim and Craig* [1993] deduced. Additionally, seasonal cycles in N_2O isotope compositions have been observed, as reported by *Park et al.* [2012] that are largely driven by STE.

Table 3.3 Comparison with other isotope flux estimates

Isotope species	Reference	Global Annual Mean Net Isotope Flux*		Note
δD of H_2	Batenburg, 2012	919 ± 226	‰ TgH yr^{-1}	1
$\delta^{18}O$ of CO_2	Kawagucci, 2008	38 ± 11.4	‰ PgC yr^{-1}	2
$\Delta^{17}O$ of CO_2	Kawagucci, 2008	48 ± 14.4	‰ PgC yr^{-1}	2
$\Delta^{17}O$ of CO_2	Boering, 2004	43.2 ± 10.8	‰ PgC yr^{-1}	3
$\delta^{15}N$ of N_2O	Park, 2004; MF: Holton****	172 ± 65	‰ TgN yr^{-1}	4
	Park, 2004; MF: Appenzeller	188 ± 68	‰ TgN yr^{-1}	4
	Park, 2004; -εL	192 ± 48	‰ TgN yr^{-1}	
	McLinden, 2003 (model)	196 ± 39	‰ TgN yr^{-1}	
$\delta^{15}N^{\alpha}$ of N_2O	Park, 2004; MF: Holton	262 ± 100	‰ TgN yr^{-1}	4
	Park, 2004; MF: Appenzeller	287 ± 104	‰ TgN yr^{-1}	4
	Park, 2004; -εL	290 ± 74	‰ TgN yr^{-1}	
$\delta^{18}O$ of N_2O	Park, 2004; MF: Holton	159 ± 60	‰ TgN yr^{-1}	4
	Park, 2004; MF: Appenzeller	174 ± 63	‰ TgN yr^{-1}	4
	Park, 2004; -εL	172 ± 43	‰ TgN yr^{-1}	
	McLinden, 2003 (model)	182 ± 37	‰ TgN yr^{-1}	

* Estimates from previously published data, including previous analyses of some of the data also reviewed and re-analyzed here. Previous studies may have used different N_2O limits, notation, mass dependent relationships, etc., as described in the text.

[1] Global annual mean net isotope flux estimated from the δD-H_2:N_2O slope of –1.90 ± 0.8 reported in *Batenburg et al.* [2012].

[2] *Kawagucci et al.* [2008] estimates uncertainty for both $\delta^{18}O$ of CO_2 and $\Delta^{17}O$ of CO_2 be 30% (uncertainties in N_2O loss rate, least-squares linear fitting, and assumption that CO_2 mixing ratio is the same in the troposphere and stratosphere)

[3] *Boering et al.* [2004] reported an isotope flux of 3.6 ± 0.9 ‰ Pmol C yr^{-1}

[4] Isotope flux using the air mass flux from *Holton* [1990] or *Appenzeller et al.* [1996]

3.3.5 Beyond global annual mean fluxes and timescales

In addition to quantifying the global annual mean net isotope fluxes for all these long-lived species, there is now evidence that seasonal and interannual variations at the surface caused by transport from the stratosphere can be even larger. For example, annual cycles in the ^{15}N and ^{18}O isotopic compositions of N_2O were measured on archived air collected at Cape Grim Tasmania between 1978 and 2005 [*Park et al.*, 2012] which show the influence of both stratospheric air and ocean upwelling. A large deviation in the ^{15}N isotopic composition was also detected in this Cape Grim dataset during the large El Niño – Southern Oscillation (ENSO) event in 1997–1998, although it is not yet clear if this excursion was driven by changes in ocean upwelling, biomass burning, STE or variations in tropospheric transport [*Park et al.*, 2012]. Thiemens *et al.* [2014] also observed a large deviation in $\Delta^{17}O$ of CO_2 during 1997–1998 in a

decade-long time series of measurements at La Jolla, California; they argue that this variation during ENSO was due to enhanced primary productivity but might also be an effect of an ENSO-driven change in STE. Hofmann *et al.* [2016] observed a seasonal cycle in $\Delta^{17}O$ of CO_2 measured in Göttingen, Germany, that may be due to the seasonality of STE, fossil fuel burning, or biosphere activity. From these recent observations, it is clear that stratospheric signals – beyond an annual average signal mixed from the stratosphere into the troposphere – need to be taken into account when isotope measurements at the surface are used to infer local or regional sources of the gases of interest, especially for seasonal time scales. This accounting for the possible influence of the stratosphere on sub-annual and interannual timescales will require new approaches to understanding mixing of stratospheric air into the troposphere on a range of spatial and temporal scales. Such modeling efforts could range from full 3D chemical-transport models (whose annual mean net isotope fluxes from the stratosphere to the troposphere could be directly checked against the values presented here) to applying "tropospheric mean ages" calculated from a 3D chemical transport model that are convolved with the empirical net isotope fluxes presented here (without having to model the stratospheric isotope compositions themselves).

Finally, we note that quantifying the effect of stratospheric chemistry and transport at Earth's surface is also of interest for tropospheric ozone, a decades-long goal in atmospheric chemistry that continues to be difficult to achieve but which is important for human health as well as establishing EPA national ambient air quality standards (NAAQS) for O_3. Given both the similarities and differences between ozone and the isotopic compositions of long-lived greenhouse gases transported from the stratosphere, modeling the influence of the stratosphere on the isotopic compositions of these long-lived gases with distinct stratospheric signals at Earth's surface could aid in deconvolving the stratospheric from tropospheric sources of ozone at a given location – in a complementary effort to the extensive modeling and observational studies of stratospheric and tropospheric ozone [e.g., *Hess and Zbinden*, 2013; *Hsu and Prather*, 2014; *Orbe et al.*, 2014; *Yang et al.*, 2016] and other chemical or aerosol tracers [e.g., *Simmonds et al.*, 2013; *Liu et al.*, 2016].

3.4 Conclusions

In this study, we have used measurements of the enrichments of the rare, heavy isotopes in stratospheric CH_4, H_2, CO_2, and N_2O and their correlation with simultaneous measurements of N_2O mixing ratios to derive entirely empirical estimates of the global annual mean net isotope fluxes from the stratosphere to the troposphere. In turn, these net isotope fluxes from the stratosphere were compared with other components in their global or regional isotope budgets to determine if transport from the stratosphere is sufficiently large to influence tropospheric isotopic compositions. For each gas, we find that the fluxes from the stratosphere are large enough to influence tropospheric isotope compositions as well as their interhemispheric gradients, even on an annual mean basis, and hence are important to take into account when making "top-down" inferences about their sources and sinks and the impact of human activities. Furthermore, we have also synthesized observational evidence the stratosphere influences isotope compositions at the surface on subannual (e.g., seasonal) and interannual (e.g., ENSO-driven) time scales – such as N_2O isotopes at Cape Grim [*Park et al.*, 2012] and $\Delta^{17}O$ of CO_2 at La Jolla [*Thiemens et al*., 2014] and at Gottingen [*Hoffman et al.,* 2016]. In these cases, the influence on surface isotope compositions is much larger than a simple (well-mixed) box model

estimate would indicate. We also argue that studies that seek to deconvolve the influence of the stratosphere on the isotope compositions of gases at Earth's surface will also inform the stratospheric influence on O_3 concentrations at a particular location where isotope data exist. Overall, inclusion of the stratospheric fluxes in models will allow the stratospheric influence to be accounted for so that other biogeochemical processes that affect the mixing ratio and isotopic composition of these trace gas species can be better understood, and serve to reduce uncertainties in quantifying both natural and anthropogenic sources and sinks of these radiatively and/or chemically important trace gases.

References

Andrews, A. E. et al. (2001), Mean ages of stratospheric air derived from in situ observations of CO_2, CH_4, and N_2O, *J. Geophys. Res.*, *106*(D23), 32295–32314, doi:10.1029/2001JD000465.

Appenzeller, C., J. R. Holton, and K. H. Rosenlof (1996), Seasonal variation of mass transport across the tropopause, *J. Geophys. Res. Atmos.*, *101*(D10), 15071–15078, doi:10.1029/96JD00821.

Assonov, S. S., and C. A. M. Brenninkmeijer (2001), A new method to determine the ^{17}O isotopic abundance in CO_2 using oxygen isotope exchange with a solid oxide, *Rapid Commun. Mass Spectrom.*, *15*, 2426–2437, doi:10.1002/rcm.529.

Assonov, S. S., and C. A. M. Brenninkmeijer (2005), Reporting small $\Delta^{17}O$ values: existing definitions and concepts, *Rapid Commun. Mass Spectrom.*, *19*, 627–636, doi:10.1002/rcm.1833.

Batenburg, A. M., T. J. Schuck, A. K. Baker, A. Zahn, C. A. M. Brenninkmeijer, and T. Röckmann (2012), The stable isotopic composition of molecular hydrogen in the tropopause region probed by the CARIBIC aircraft, *Atmos. Chem. Phys.*, *12*(10), 4633–4646, doi:10.5194/acp-12-4633-2012.

Beramendi-Orosco, L., G. Gonzalez-Hernandez, A. Martinez-Jurado, A. Martinez-Reyes, A. Garcia-Samano, J. Villanueva-Diaz, F. J. Santos-Arevalo, I. Gomez-Martinez, and O. Amador-Muñoz (2015), Temporal and Spatial Variations of Atmospheric Radiocarbon in the Mexico City Metropolitan Area, *Radiocarbon*, *57*(3), 363–375, doi:10.2458/azu_rc.57.18360.

Bergamaschi, P. et al. (2015), Top-down estimates of European CH_4 and N_2O emissions based on four different inverse models, *Atmos. Chem. Phys.*, *15*, 715–736, doi:10.5194/acp-15-715-2015.

Boering, K. A., T. Jackson, K. J. Hoag, A. S. Cole, M. J. Perri, M. Thiemens, and E. Atlas (2004), Observations of the anomalous oxygen isotopic composition of carbon dioxide in the lower stratosphere and the flux of the anomaly to the troposphere, *Geophys. Res. Lett.*, *31*, L03109, doi:10.1029/2003GL018451.

Brand, W. A. (1995), PreCon: A Fully Automated Interface for the Pre-GC Concentration of Trace Gases on Air for Isotopic Analysis, *Isotopes Environ. Health Stud.*, *31*, 277–284, doi:10.1080/10256019508036271.

Brenninkmeijer, C. A. M., D. C. Lowe, M. R. Manning, R. J. Sparks, and P. F. J. van Velthoven (1995), The ^{13}C, ^{14}C, and ^{18}O isotopic composition of CO, CH_4, and CO_2 in the higher southern latitudes lower stratosphere, *J. Geophys. Res.*, *100*(D12), 26163–26172.

Cantrell, C. A. (2008), Technical Note: Review of methods for linear least-squares fitting of data and application to atmospheric chemistry problems, *Atmos. Chem. Phys.*, *8*, 5477–5487, doi:10.5194/acp-8-5477-2008.

Ciais, P. et al. (1997), A three-dimensional synthesis study of $\delta^{18}O$ in atmospheric CO_2: 1. Surface fluxes, *J. Geophys. Res. Atmos.*, *102*(D5), 5857–5872, doi:10.1029/96JD02360.

Croteau, P., E. L. Atlas, S. M. Schauffler, D. R. Blake, G. S. Diskin, and K. A. Boering (2010), Effect of local and regional sources on the isotopic composition of nitrous oxide in the tropical free troposphere and tropopause layer, *J. Geophys. Res.*, *115*, DJ00J11, doi:10.1029/2009jd013117.

Cuntz, M., P. Ciais, G. Hoffmann, and W. Knorr (2003a), A comprehensive global three-dimensional model of $\delta^{18}O$ in atmospheric CO_2: 1. Validation of surface processes, *J. Geophys. Res.*, *108*(D17), 4527, doi:10.1029/2002JD003153.

Cuntz, M., P. Ciais, G. Hoffmann, C. E. Allison, R. J. Francey, W. Knoor, P. P. Tans, J. W. C. White, and I. Levin (2003b), A comprehensive global three-dimensional model of $\delta^{18}O$ in atmospheric CO_2 : 2. Mapping the atmospheric signal, *J. Geophys. Res.*, *108*(D17), 4528, doi:10.1029/2002JD003154.

Cziczo, D. J., D. S. Thomson, and D. M. Murphy (2001), Ablation, flux, and atmospheric implications of meteors inferred from stratospheric aerosol., *Science*, *291*, 1772–1775, doi:10.1126/science.1057737.

Denman, K.L., G. Brasseur, A. Chidthaisong, P. Ciais, P.M. Cox, R.E. Dickinson, D. Hauglustaine, C. Heinze, E. Holland, D. Jacob, U. Lohmann, S Ramachandran, P.L. da Silva Dias, S.C. Wofsy and X. Zhang, 2007: Couplings Between Changes in the Climate System and Biogeochemistry. In: Climate Change 2007: The Physical Science Basis. Contribution of Working Group I to the Fourth

Assessment Report of the Intergovernmental Panel on Climate Change [Solomon, S., D. Qin, M. Manning, Z. Chen, M. Marquis, K.B. Averyt, M.Tignor and H.L. Miller (eds.)]. Cambridge University Press, Cambridge, United Kingdom and New York, NY, USA.

Ehhalt, D. H., U. Schmidt, and L. E. Heidt (1977), Vertical Profiles of Molecular Hydrogen in the Troposphere and Stratosphere, *J. Geophys. Res.*, *82*(37), 5907–5911.

Ehhalt, D. H., J. A. Davidson, C. A. Cantrell, I. Friedman, and S. Tyler (1989), The Kinetic Isotope Effect in the Reaction of H_2 With OH, *J. Geophys. Res.*, *94*(D7), 9831–9836.

Fahey, D. W. et al. (1995), Emission Measurements of the Concorde Supersonic Aircraft in the Lower Stratosphere, *Science*, *270*(5233), 70–74, doi:10.1126/science.270.5233.70.

Farquhar, G. D., J. Lloyd, J. A. Taylor, L. B. Flanagan, J. P. Syvertsen, K. T. Hubick, S. C. Wong, and J. R. Ehleringer (1993), Vegetation effects on the isotope composition of oxygen in atmospheric CO_2, *Nature*, *363*, 439–443, doi:10.1038/363439a0.

Feck, T., J. U. Grooß, and M. Riese (2008), Sensitivity of Arctic ozone loss to stratospheric H_2O, *Geophys. Res. Lett.*, *35*, L01803, doi:10.1029/2007GL031334.

Feilberg, K. L., D. W. T. Griffith, M. S. Johnson, and C. J. Nielsen (2005), The ^{13}C and D kinetic isotope effects in the reaction of CH_4 with Cl, *Int. J. Chem. Kinet.*, *37*(2), 110–118, doi:10.1002/kin.20058.

Flocke, F. et al. (1999), An examination of chemistry and transport processes in the tropical lower stratosphere using observations of long-lived and short-lived compounds obtained during STRAT and POLARIS, *J. Geophys. Res.*, *104*(D21), 26625–26642, doi:10.1029/1999jd900504.

Froidevaux, L. et al. (2006), Early validation analyses of atmospheric profiles from EOS MLS on the Aura satellite, *IEEE Trans. Geosci. Remote Sens.*, *44*(5), 1106–1121, doi:10.1109/tgrs.2006.864366.

Fung, I., J. John, J. Lerner, E. Matthews, M. Prather, L. P. Steele, and P. J. Fraser (1991), Three-Dimensional Model Synthesis of the Global Methane Cycle, *J. Geophys. Res.*, *96*(D7), 13033–13065, doi:10.1029/91jd01247.

Fung, I. et al. (1997), Carbon 13 exchanges between the atmosphere and biosphere, *Global Biogeochem. Cycles*, *11*(4), 507–533, doi:10.1029/97GB01751.

Gamo, T., M. Tsutsumi, H. Sakai, T. Nakazawa, M. Tanaka, H. Honda, H. Kubo, and T. Itoh (1989), Carbon and oxygen isotopic ratios of carbon dioxide of a stratospheric profile over Japan, *Tellus*, *41B*, 127–133, doi:10.1111/j.1600-0889.1989.tb00130.x.

Gerst, S., and P. Quay (2001), Deuterium component of the global molecular hydrogen cycle, *J. Geophys. Res.*, *106*(D5), 5021–5031, doi:10.1029/2000jd900593.

Graven, H. D. (2015), Impact of fossil fuel emissions on atmospheric radiocarbon and various applications of radiocarbon over this century, *PNAS*, *112*(31), 9542–9545, doi:10.1073/pnas.1504467112.

Graven, H. D., T. P. Guilderson, and R. F. Keeling (2012), Observations of radiocarbon in CO_2 at La Jolla, California, USA 1992-2007: Analysis of the long-term trend, *J. Geophys. Res.*, *117*, D02302, doi:10.1029/2011JD016533.

Guilderson, T. P., K. Caldeira, and P. B. Duffy (2000), Radiocarbon as a diagnostic tracer in ocean and carbon cycle modeling, *Global Biogeochem. Cycles*, *14*(3), 887–902, doi:10.1029/1999GB001192.

Hess, P. G., and R. Zbinden (2013), Stratospheric impact on tropospheric ozone variability and trends: 1990-2009, *Atmos. Chem. Phys.*, *13*, 649–674, doi:10.5194/acp-13-649-2013.

Hirsch, A. I., A. M. Michalak, L. M. Bruhwiler, W. Peters, E. J. Dlugokencky, and P. P. Tans (2006), Inverse modeling estimates of the global nitrous oxide surface flux from 1998-2001, *Global Biogeochem. Cycles*, *20*, GB1008, doi:10.1029/2004GB002443.

Hoag, K. J., C. J. Still, I. Y. Fung, and K. A. Boering (2005), Triple oxygen isotope composition of tropospheric carbon dioxide as a tracer of terrestrial gross carbon fluxes, *Geophys. Res. Lett.*, *32*, L02802, doi:10.1029/2004GL021011.

Hofmann, M. E. G., B. Horváth, L. Schneider, W. Peters, K. Schützenmeister, and A. Pack (2016), Atmospheric measurements of $\Delta^{17}O$ in CO_2 in Göttingen, Germany reveal a seasonal cycle driven by biospheric uptake, *Geochim. Cosmochim. Acta*, *199*, 143–163, doi:10.1016/j.gca.2016.11.019.

Holton, J. R. (1986), A dynamically based transport parameterization for one-dimensional photochemical

models of the stratosphere, *J. Geophys. Res.*, *91*(D2), 2681–2686, doi:10.1029/JD091iD02p02681.
Holton, J. R. (1990), On the Global Exchange of Mass between the Stratosphere and Troposphere, *J. Atmos. Sci.*, *47*(3), 392–395.
Houweling, S., P. Bergamaschi, F. Chevallier, M. Heimann, T. Kaminski, M. Krol, A. M. Michalak, and P. Patra (2017), Global inverse modeling of CH_4 sources and sinks: An overview of methods, *Atmos. Chem. Phys. Discuss.*, *17*, 256–256, doi:10.5194/acp-17-235-2017.
Hsu, J., and M. J. Prather (2014), Is the residual vertical velocity a good proxy for stratosphere-troposphere exchange of ozone?, *Geophys. Res. Lett.*, *41*, 9024–9032, doi:10.1002/2014GL061994.
Huang, J. et al. (2008), Estimation of regional emissions of nitrous oxide from 1997 to 2005 using multinetwork measurements, a chemical transport model, and an inverse method, *J. Geophys. Res. Atmos.*, *113*, D17313, doi:10.1029/2007JD009381.
Hurst, D. F. et al. (2000), Comparison of in situ N_2O and CH_4 measurements in the upper troposphere and lower stratosphere during STRAT and POLARIS, *J. Geophys. Res.*, *105*(D15), 19811–19822.
Jacobson, M. Z. (2008), Effects of wind-powered hydrogen fuel cell vehicles on stratospheric ozone and global climate, *Geophys. Res. Lett.*, *35*, L19803, doi:10.1029/2008GL035102.
Jones, R. L., and J. A. Pyle (1984), Observations of CH_4 and N_2O by the NIMBUS 7 SAMS: A comparison with in situ data and two-dimensional numerical model calculations, *J. Geophys. Res.*, *89*(D4), 5263–5279.
Kai, F. M., S. C. Tyler, J. T. Randerson, and D. R. Blake (2011), Reduced methane growth rate explained by decreased Northern Hemisphere microbial sources., *Nature*, *476*(7359), 194–197, doi:10.1038/nature10259.
Kaiser, J., T. Röckmann, and C. A. M. Brenninkmeijer (2002), Temperature dependence of isotope fractionation in N_2O photolysis, *Phys. Chem. Chem. Phys.*, *4*, 4420–4430, doi:10.1039/b204837j.
Kaiser, J., T. Röckmann, C. A. M. Brenninkmeijer, and P. J. Crutzen (2003), Wavelength dependence of isotope fractionation in N_2O photolysis, *Atmos. Chem. Phys.*, *3*, 303–313.
Kanu, A. M., L. L. Comfort, T. P. Guilderson, P. J. Cameron-Smith, D. J. Bergmann, E. Atlas, S. Schauffler, and K. A. Boering (2016), Measurements and modeling of contemporary radiocarbon in the stratosphere, *Geophys. Res. Lett.*, *43*, 1399–1406, doi:10.1002/2013GL058740.
Kawagucci, S., U. Tsunogai, S. Kudo, F. Nakagawa, H. Honda, S. Aoki, T. Nakazawa, M. Tsutsumi, and T. Gamo (2008), Long-term observation of mass-independent oxygen isotope anomaly in stratospheric CO(2), *Atmos. Chem. Phys.*, *8*, 6189–6197.
Kim, K.-R., and H. Craig (1993), Nitrogen-15 and Oxygen-18 Characteristics of Nitrous Oxide: A Global Perspective, *Science*, *262*(5141), 1855–1857.
Kirschke, S. et al. (2013), Three decades of global methane sources and sinks, *Nat. Geosci.*, *6*, 813–823, doi:10.1038/ngeo1955.
LaFranchi, B. W. et al. (2013), Constraints on emissions of carbon monoxide, methane, and a suite of hydrocarbons in the Colorado Front Range using observations of $^{14}CO_2$, *Atmos. Chem. Phys.*, *13*, 11101–11120, doi:10.5194/acp-13-11101-2013.
Lämmerzahl, P., T. Röckmann, C. A. M. Brenninkmeijer, D. Krankowsky, and K. Mauersberger (2002), Oxygen isotope composition of stratospheric carbon dioxide, *Geophys. Res. Lett.*, *29*(12), 1582, doi:10.1029/2001GL014343.
Levin, I., T. Naegler, B. Kromer, M. Diehl, R. J. Francey, A. J. Gomez-Pelaez, L. P. Steele, D. Wagenbach, R. Weller, and D. E. Worthy (2010), Observations and modelling of the global distribution and long-term trend of atmospheric $^{14}CO_2$, *Tellus Ser. B-Chemical Phys. Meteorol.*, *62B*, 26–46, doi:10.1111/j.1600-0889.2009.00446.x.
Liu, H. et al. (2016), Using beryllium-7 to assess cross-tropopause transport in global models, *Atmos. Chem. Phys.*, *16*, 4641–4659, doi:10.5194/acp-16-4641-2016.
Luz, B., E. Barkan, M. L. Bender, M. H. Thiemens, and K. A. Boering (1999), Triple-isotope composition of atmospheric oxygen as a tracer of biosphere productivity, *Nature*, *400*, 547–550, doi:10.1038/22987.
Mahlman, J. D., H. I. Levy, and W. J. Moxim (1986), Three-Dimensional Simulations of Stratospheric

N_2O: Predictions for Other Trace Constituents, *J. Geophys. Res.*, *91*(D2), 2687–2707.
Mar, K. A., M. C. McCarthy, P. Connell, and K. A. Boering (2007), Modeling the photochemical origins of the extreme deuterium enrichment in stratospheric H_2, *J. Geophys. Res.*, *112*, D19302, doi:10.1029/2006jd007403.
Mauersberger, K., D. Krankowsky, C. Janssen, and R. Schinke (2005), Assessment of the ozone isotope effect, in *Advances in Atomic, Molecular, and Optical Physics*, vol. 50, edited by B. Bederson and H. Walther, pp. 1–54, Elsevier Academic, San Diego.
McCarthy, M. C., P. Connell, and K. A. Boering (2001), Isotopic fractionation of methane in the stratosphere and its effect on free tropospheric isotopic compositions, *Geophys. Res. Lett.*, *28*(19), 3657–3660, doi:10.1029/2001GL013159.
McCarthy, M. C., K. A. Boering, A. L. Rice, S. C. Tyler, P. Connell, and E. Atlas (2003), Carbon and hydrogen isotopic compositions of stratospheric methane: 2. Two-dimensional model results and implications for kinetic isotope effects, *J. Geophys. Res.*, *108*(D15), 4461, doi:10.1029/2002JD003183.
McElroy, M. B., and D. B. A. Jones (1996), Evidence for an additional source of atmospheric N_2O, *Global Biogeochem. Cycles*, *10*(4), 651–659, doi:10.1029/96GB02346.
McLinden, C. A., M. J. Prather, and M. S. Johnson (2003), Global modeling of the isotopic analogues of N_2O: Stratospheric distributions, budgets, and the ^{17}O–^{18}O mass-independent anomaly, *J. Geophys. Res.*, *108*(D8), 4233, doi:10.1029/2002JD002560.
Meijer, H. A. J., and W. J. Li (1998), The use of electrolysis for accurate $\delta^{17}O$ and $\delta^{18}O$ isotope measurements in water, *Isotopes Environ. Health Stud.*, *34*(4), 349–369, doi:10.1080/10256019808234072.
Minschwaner, K., R. J. Salawitch, and M. B. McElroy (1993), Absorption of solar radiation by O_2 : Implications for O_3 and lifetimes of N_2O, $CFCl_3$, and CF_2Cl_2, *J. Geophys. Res.*, *98*(D6), 10543–10561, doi:10.1029/93JD00223.
Murphy, D. M., and D. W. Fahey (1994), An estimate of the flux of stratospheric reactive nitrogen and ozone into the troposphere, *J. Geophys. Res.*, *99*(D3), 5325–5332, doi:10.1029/93jd03558.
Newman, P. A., D. W. Fahey, W. H. Brune, M. J. Kurylo, and S. R. Kawa (1999), Preface [to special section on Photochemistry of Ozone Loss in the Arctic Region in Summer (POLARIS)], *J. Geophys. Res. Atmos.*, *104*(D21), 26481–26495, doi:10.1029/1999JD900832.
Newman, P. A. et al. (2002), An overview of the SOLVE/THESEO 2000 campaign, *J. Geophys. Res.*, *107*(D20), doi:10.1029/2001jd001303.
NOAA-ESRL, Global Monitoring Division: Global Greenhouse Gas Reference Network, available at http://www.esrl.noaa.gov/gmd/ccgg/, last access: 07 May 2017.
Olsen, M. A., A. R. Douglass, and M. R. Schoeberl (2002), Estimating downward cross-tropopause ozone flux using column ozone and potential vorticity, *J. Geophys. Res. Atmos.*, *107*(D22), 4636, doi:10.1029/2001JD002041.
Orbe, C., M. Holzer, L. M. Polvani, D. W. Waugh, F. Li, L. D. Oman, and P. A. Newman (2014), Seasonal ventilation of the stratosphere: Robust diagnostics from one-way flux distributions, *J. Geophys. Res. Atmos.*, *119*, 293–306, doi:10.1002/2013JD020213.
Park, S. et al. (2012), Trends and seasonal cycles in the isotopic composition of nitrous oxide since 1940, *Nat. Geosci.*, *5*, 261–265, doi:10.1038/ngeo1421.
Park, S. Y., E. L. Atlas, K. A. Boering, P. Sunyoung, E. L. Atlas, K. A. Boering, S. Y. Park, E. L. Atlas, and K. A. Boering (2004), Measurements of N_2O isotopologues in the stratosphere: Influence of transport on the apparent enrichment factors and the isotopologue fluxes to the troposphere, *J. Geophys. Res.*, *109*, D01305, doi:10.1029/2003JD003731.
Pieterse, G., M. C. Krol, A. M. Batenburg, L. P. Steele, P. B. Krummel, R. L. Langenfelds, and T. Röckmann (2011), Global modelling of H_2 mixing ratios and isotopic compositions with the TM5 model, *Atmos. Chem. Phys.*, *11*, 7001–7026, doi:10.5194/acp-11-7001-2011.
Pieterse, G. et al. (2013), Reassessing the variability in atmospheric H_2 using the two-way nested TM5 model, *J. Geophys. Res.*, *118*, 3764–3780, doi:10.1002/jgrd.50204.

Plumb, R. A. (2007), Tracer interrelationships in the stratosphere, *Rev. Geophys.*, *45*, RG4005, doi:10.1029/2005RG000179.

Plumb, R. A., and M. K. W. Ko (1992), Interrelationships between mixing ratios of long lived stratospheric constituents, *J. Geophys. Res.*, *97*(D9), 10145–10156.

Podolske, J., and M. Loewenstein (1993), Airborne tunable diode laser spectrometer for trace-gas measurement in the lower stratosphere, *Appl. Opt.*, *32*(27), 5324–5333.

Prather, M. and D. Ehhalt, Atmospheric Chemistry and Greenhouse Gases, in Climate Change 2001: The Scientific Basis. Contribution of Working Group I to the Third Assessment Report of the Intergovernmental Panel on Climate Change, J.T. Houghton et al. (eds.), Cambridge University Press, New York, NY, pp. 239-287, 2001.

Prather, M. J., C. D. Holmes, and J. Hsu (2012), Reactive greenhouse gas scenarios: Systematic exploration of uncertainties and the role of atmospheric chemistry, *Geophys. Res. Lett.*, *39*(9), 6–10, doi:10.1029/2012GL051440.

Price, H., L. Jaegle, A. Rice, P. Quay, P. C. Novelli, and R. Gammon (2007), Global budget of molecular hydrogen and its deuterium content: Constraints from ground station, cruise, and aircraft observations, *J. Geophys. Res.*, *112*, doi:10.1029/2006jd008152.

Quay, P., J. Stutsman, D. Wilbur, A. Snover, E. Dlugokencky, and T. Brown (1999), The isotopic composition of atmospheric methane, *Global Biogeochem. Cycles*, *13*, 445–461, doi:10.1029/1998gb900006.

Raupach, M.R., Inferring biogeochemical sources and sinks from atmospheric concentrations: General considerations and applications in vegetation canopies. In: *Global Biogeochemical Cycles in the Climate System* [Schulze, E.D., M. Heimann, S. Harrison, E. Holland, J. Llyod, I.C. Prentice, D. Shimel (eds.)], 41-60. Academic Press, San Diego, 2001.

Rahn, T., and M. Wahlen (1997), Stable isotope enrichment in stratospheric nitrous oxide, *Science*, *278*(5344), 1776–1778, doi:10.1126/science.278.5344.1776.

Rahn, T., N. Kitchen, J. Eiler, and P. Sciences (2002), D/H ratios of atmospheric H_2 in urban air : Results using new methods for analysis of nano-molar H_2 samples, *Geochim. Cosmochim. Acta*, *66*(14), 2475–2481, doi:10.1016/S0016-7037(02)00858-X.

Rahn, T., J. M. Eiler, K. A. Boering, P. O. Wennberg, M. C. McCarthy, S. Tyler, S. Schauffler, S. Donnelly, and E. Atlas (2003), Extreme deuterium enrichment in stratospheric hydrogen and the global atmospheric budget of H_2, *Nature*, *424*(6951), 918–921, doi:10.1038/nature01917.

Randerson, J. T., I. G. Enting, E. A. G. Schuur, K. Caldeira, and I. Y. Fung (2002), Seasonal and latitudinal variability of troposphere $\Delta^{14}C$: Post bomb contributions from fossil fuels, oceans, the stratosphere, and the terrestrial biosphere, *Global Biogeochem. Cycles*, *16*(4), 1112, doi:10.1029/2002GB001876.

Rhee, T. S., C. A. M. Brenninkmeijer, M. Brass, and C. Bruehl (2006), Isotopic composition of H-2 from CH_4 oxidation in the stratosphere and the troposphere, *J. Geophys. Res.*, *111*, doi:10.1029/2005jd006760.

Rice, A. L., A. A. Gotoh, H. O. Ajie, and S. C. Tyler (2001), High-precision continuous-flow measurement of $\delta^{13}C$ and δD of atmospheric CH_4, *Anal. Chem.*, *73*(17), 4104–4110, doi:10.1021/ac0155106.

Rice, A. L., S. C. Tyler, M. C. McCarthy, K. A. Boering, and E. Atlas (2003), Carbon and hydrogen isotopic compositions of stratospheric methane: 1. High-precision observations from the NASA ER-2 aircraft, *J. Geophys. Res.*, *108*(D15), 4460, doi:10.1029/2002JD003042.

Rice, A. L., C. L. Butenhoff, D. G. Teama, F. H. Röger, M. A. K. Khalil, and R. A. Rasmussen (2016), Atmospheric methane isotopic record favors fossil sources flat in 1980s and 1990s with recent increase., *PNAS*, *113*(39), 10791–10796, doi:10.1073/pnas.1522923113.

Riley, W. J., D. Y. Hsueh, J. T. Randerson, M. L. Fischer, J. G. Hatch, D. E. Pataki, W. Wang, and M. L. Goulden (2008), Where do fossil fuel carbon dioxide emissions from California go? An analysis based on radiocarbon observations and an atmospheric transport model, *J. Geophys. Res.*, *113*, G04002, doi:10.1029/2007JG000625.

Röckmann, T., C. A. M. Brenninkmeijer, G. Saueressig, P. Bergamaschi, J. N. Crowley, H. Fischer, and P. J. Crutzen (1998), Mass-independent oxygen isotope fractionation in atmospheric CO as a result of the reaction CO+OH, *Science*, *281*, 544–546, doi:10.1126/science.281.5376.544.

Röckmann, T., T. S. Rhee, and A. Engel (2003a), Heavy hydrogen in the stratosphere, *Atmos. Chem. Phys.*, *3*, 2015–2023.

Röckmann, T., J. Kaiser, and C. A. M. Brenninkmeijer (2003b), The isotopic fingerprint of the pre-industrial and the anthropogenic N_2O source, *Atmos. Chem. Phys.*, *3*, 315–323.

Röckmann, T., and I. Levin (2005), High-precision determination of the changing isotopic composition of atmospheric N_2O from 1990 to 2002, *J. Geophys. Res.*, *110*, D21304, doi:10.1029/2005jd006066

Röckmann, T., M. Brass, R. Borchers, and A. Engel (2011), The isotopic composition of methane in the stratosphere: high-altitude balloon sample measurements, *Atmos. Chem. Phys.*, *11*, 13287–13304, doi:10.5194/acp-11-13287-2011.

Saikawa, E. et al. (2014), Global and regional emissions estimates for N_2O, *Atmos. Chem. Phys.*, *14*(9), 4617–4641, doi:10.5194/acp-14-4617-2014.

Saueressig, G., J. N. Crowley, P. Bergamaschi, C. Bruhl, C. A. M. Brenninkmeijer, and H. Fischer (2001), Carbon 13 and D kinetic isotope effects in the reactions of CH_4 with $O(^1D)$ and OH: New laboratory measurements and their implications for the isotopic composition of stratospheric methane, *J. Geophys. Res.*, *106*(D19), 23127–23138, doi:10.1029/2000JD000120.

Saunois, M. et al. (2016a), The global methane budget 2000–2012, *Earth Syst. Sci. Data*, *8*, 697–751, doi:10.5194/essd-8-697-2016.

Saunois, M., R. B. Jackson, P. Bousquet, B. Poulter, and J. G. Canadell (2016b), The growing role of methane in anthropogenic climate change, *Environ. Res. Lett.*, *11*, 120207, doi:10.1088/1748-9326/11/12/120207.

Schaefer, H. et al. (2016), A 21st century shift from fossil-fuel to biogenic methane emissions indicated by $^{13}CH_4$, *Science*, *352*(6281), 80–84, doi:10.1126/science.aad2705.

Schauffler, S. M., E. L. Atlas, S. G. Donnelly, A. Andrews, S. A. Montzka, J. W. Elkins, D. F. Hurst, P. A. Romashkin, G. S. Dutton, and V. Stroud (2003), Chlorine budget and partitioning during the Stratospheric Aerosol and Gas Experiment (SAGE) III Ozone Loss and Validation Experiment (SOLVE), *J. Geophys. Res.*, *108*(D5), 4173, doi:10.1029/2001jd002040.

Schmidt, J. A., M. S. Johnson, and R. Schinke (2011), Isotope effects in N_2O photolysis from first principles, *Atmos. Chem. Phys.*, *11*, 8965–8975, doi:10.5194/acp-11-8965-2011.

Schwietzke, S. et al. (2016), Upward revision of global fossil fuel methane emissions based on isotope database, *Nature*, *538*(7623), 88–91, doi:10.1038/nature19797.

Simmonds, P. G. et al. (2013), Interannual fluctuations in the seasonal cycle of nitrous oxide and chlorofluorocarbons due to the Brewer-Dobson circulation, *J. Geophys. Res. Atmos.*, *118*, 10694–10706, doi:10.1002/jgrd.50832.

Stocker, T. F., D. Qin, G.-K. Plattner, M. Tignor, S. K. Allen, J. Boschung, A. Nauels, Y. Xia, V. Bex, and P. M. Midgley (Eds.) (2013), *IPCC, 2013: Climate Change 2013: The physical science basis. Contribution of Working Group I to the Fifth Assessment Report of the Intergovernmental Panel on Climate Change*, Cambridge University Press, New York, NY, USA.

Stuiver, M., and H. A. Polach (1977), Discussion: Reporting of ^{14}C data, *Radiocarbon*, *19*(3), 355–363.

Sugawara, S., T. Nakazawa, Y. Shirakawa, K. Kawamura, S. Aoki, T. Machida, and H. Honda (1997), Vertical profile of the carbon isotopic ratio of stratospheric methane over Japan, *Geophys. Res. Lett.*, *24*(23), 2989–2992, doi:10.1029/97GL03044.

Talukdar, R. K., T. Gierczak, L. Goldfarb, Y. Rudich, B. S. M. Rao, and A. R. Ravishankara (1996), Kinetics of Hydroxyl Radical Reactions with Isotopically Labeled Hydrogen, *J. Phys. Chem.*, *100*(8), 3037, doi:10.1021/jp9518724.

Thiemens, M. H., T. Jackson, E. C. Zipf, P. W. Erdman, and C. Vanegmond (1995), Carbon-dioxide and oxygen-isotope anomalies in the mesosphere and stratosphere, *Science*, *270*(5238), 969–972, doi:10.1126/science.270.5238.969.

Thiemens, M. H., S. Chakraborty, and T. L. Jackson (2014), Decadal $\Delta^{17}O$ record of tropospheric CO_2:

Verification of a stratospheric component in the troposphere, *J. Geophys. Res. Atmos.*, *119*, 6221–6229, doi:10.1002/2013jd020317.
Thompson, R. L. et al. (2014a), TransCom N_2O model inter-comparison-Part 1: Assessing the influence of transport and surface fluxes on tropospheric N_2O variability, *Atmos. Chem. Phys.*, *14*(8), 4349–4368, doi:10.5194/acp-14-4349-2014.
Thompson, R. L. et al. (2014b), TransCom N_2O model inter-comparison - Part 2: Atmospheric inversion estimates of N_2O emissions, *Atmos. Chem. Phys.*, *14*(12), 6177–6194, doi:10.5194/acp-14-6177-2014.
Toyoda, S., and N. Yoshida (1999), Determination of nitrogen isotopomers of nitrous oxide on a modified isotope ratio mass spectrometer, *Anal. Chem.*, *71*(20), 4711–4718, doi:10.1021/ac9904563.
Toyoda, S., N. Yoshida, T. Urabe, S. Aoki, T. Nakazawa, S. Sugawara, and H. Honda (2001), Fractionation of N_2O isotopomers in the stratosphere, *J. Geophys. Res.*, *106*(D7), 7515, doi:10.1029/2000JD900680.
Toyoda, S., N. Kuroki, N. Yoshida, K. Ishijima, Y. Tohjima, and T. Machida (2013), Decadal time series of tropospheric abundance of N_2O isotopomers and isotopologues in the Northern Hemisphere obtained by the long-term observation at Hateruma Island, Japan, *J. Geophys. Res.*, *118*, 3369–3381, doi:10.1002/jgrd.50221
Tromp, T. K., R.-L. Shia, M. Allen, J. M. Eiler, and Y. L. Yung (2003), Potential Environmental Impact of a Hydrogen Economy on the Stratosphere, *Science*, *300*, 1740–1742.
Turnbull, J., P. Rayner, J. Miller, T. Naegler, P. Ciais, and A. Cozic (2009), On the use of $^{14}CO_2$ as a tracer for fossil fuel CO_2: Quantifying uncertainties using an atmospheric transport model, *J. Geophys. Res.*, *114*, D22302, doi:10.1029/2009JD012308.
Wang, J. S., M. B. McElroy, C. M. Spivakovsky, and D. B. A. Jones (2002), On the contribution of anthropogenic Cl to the increase in $\delta^{13}C$ of atmospheric methane, *Global Biogeochem. Cycles*, *16*(3), 1047, doi:10.1029/2001GB001572.
Warwick, N. J., S. Bekki, E. G. Nisbet, and J. A. Pyle (2004), Impact of a hydrogen economy on the stratosphere and troposphere studied in a 2-D model, *Geophys. Res. Lett.*, *31*, L05107, doi:10.1029/2003GL019224.
Welp, L. R., R. F. Keeling, H. A. J. Meijer, A. F. Bollenbacher, S. C. Piper, K. Yoshimura, R. J. Francey, C. E. Allison, and M. Wahlen (2011), Interannual variability in the oxygen isotopes of atmospheric CO(2) driven by El Nino, *Nature*, *477*, 579–582, doi:10.1038/nature10421.
Wiegel, A. A., A. S. Cole, K. J. Hoag, E. L. Atlas, S. M. Schauffler, and K. A. Boering (2013), Unexpected variations in the triple oxygen isotope composition of stratospheric carbon dioxide, *PNAS*, *110*(44), 17680–17685, doi:10.1073/pnas.1213082110.
Yang, H., G. Chen, Q. Tang, and P. Hess (2016), Quantifying isentropic stratosphere-troposphere exchange of ozone, *J. Geophys. Res. Atmos.*, *121*, 3372–3387, doi:10.1002/2015JD024180.
Yung, Y. L., and C. E. Miller (1997), Isotopic Fractionation of Stratospheric Nitrous Oxide, *Science*, *278*(5344), 1778–1780, doi:10.1126/science.278.5344.1778.
Yung, Y. L., A. Y. T. Lee, F. W. Irion, W. B. DeMore, and J. Wen (1997), Carbon dioxide in the atmosphere: Isotopic exchange with ozone and its use as a tracer in the middle atmosphere, *J. Geophys. Res.*, *102*(D09), 10857–10866, doi:10.1029/97jd00528.
Yung, Y. L., M. C. Liang, G. A. Blake, R. P. Muller, and C. E. Miller (2004), Evidence for O-atom exchange in the $O(^1D)+N_2O$ reaction as the source of mass-independent isotopic fractionation in atmospheric N_2O, *Geophys. Res. Lett.*, *31*, L19106, doi:10.1029/2004GL020950.

Supplementary Materials

Table 3.ST1 Estimates for $\delta_S - \delta_T$, $F(X)_{ST}$, and global annual mean net isotope fluxes

Isotope species	Campaign	Mass Flux = Appenzeller				Mass Flux = Holton			
		$\delta_S - \delta_T$ *	$F(X)_{ST}$ †	Global Annual Mean Net Isotope Flux		$\delta_S - \delta_T$ *	$F(X)_{ST}$ †	Global Annual Mean Net Isotope Flux	
$\delta^{13}C$ of CH_4	STRAT, POLARIS, SOLVE	0.54 ± 0.14	474 ± 6	256 ± 68	‰ TgC yr^{-1}	1.83 ± 0.47	124 ± 6	226 ± 70	‰ TgC yr^{-1}
δD of CH_4	STRAT, POLARIS, SOLVE	3.18 ± 0.96	474 ± 6	1511 ± 480	‰ TgC yr^{-1}	10.83 ± 3.28	124 ± 6	1338 ± 489	‰ TgC yr^{-1}
δD of H_2	SOLVE	18.21 ± 7.96	25	449 ± 196	‰ TgH yr^{-1}	61.91 ± 27.07	7	449 ± 196	‰ TgH yr^{-1}
$\delta^{18}O$ of CO_2	SOLVE	0.32 ± 0.10	104	34 ± 11	‰ PgC yr^{-1}	1.10 ± 0.36	31	34 ± 11	‰ PgC yr^{-1}
$\Delta^{17}O$ of CO_2	SOLVE	0.47 ± 0.19	104	49 ± 20	‰ PgC yr^{-1}	1.60 ± 0.64	31	49 ± 20	‰ PgC yr^{-1}
	POLARIS	0.44 ± 0.11	102	45 ± 11	‰ PgC yr^{-1}	1.48 ± 0.38	30	45 ± 11	‰ PgC yr^{-1}
$\delta^{15}N$ of N_2O	POLARIS, SOLVE	1.00 ± 0.27	194 ± 3	194 ± 56	‰ TgN yr^{-1}	3.39 ± 0.91	48 ± 3	163 ± 58	‰ TgN yr^{-1}
	Balloon 2004/2005	0.96 ± 0.24	197 ± 3	189 ± 50	‰ TgN yr^{-1}	3.26 ± 0.8	49 ± 3	159 ± 52	‰ TgN yr^{-1}
$\delta^{15}N^{\alpha}$ of N_2O	POLARIS, SOLVE	1.77 ± 0.47	194 ± 3	344 ± 98	‰ TgN yr^{-1}	6.02 ± 1.60	48 ± 3	289 ± 101	‰ TgN yr^{-1}
	Balloon 2004/2005	1.38 ± 0.46	197 ± 3	272 ± 97	‰ TgN yr^{-1}	4.70 ± 1.56	49 ± 3	229 ± 100	‰ TgN yr^{-1}
$\delta^{18}O$ of N_2O	POLARIS, SOLVE	0.89 ± 0.22	194 ± 3	174 ± 47	‰ TgN yr^{-1}	3.04 ± 0.76	48 ± 3	146 ± 48	‰ TgN yr^{-1}
	Balloon 2004/2005	0.77 ± 0.20	197 ± 3	152 ± 42	‰ TgN yr^{-1}	2.62 ± 0.67	49 ± 3	128 ± 43	‰ TgN yr^{-1}

* $\delta_S - \delta_T = -m \cdot (L+G_S)/MF$ in units of ‰; 1σ uncertainty in slope and N_2O loss rate

† $F(X)_{ST} = -m' \cdot (L+G_S) + [X]_T \cdot MF$ in units of Tg X yr^{-1} or Pg X yr^{-1}; Uncertainty in slope and N_2O loss rate only. For H_2 and CO_2 for which $m'=0$ or $m' \approx 0$, the uncertainty in $F(X)_{ST}$ is negligible.

Table 3.ST2 Isotopic compositions of CH_4 from *Rice et al., 2003*

Flight Date mm/dd/yyyy	Collection Time Universal, s	Pressure-Altitude, km	Latitude, °N	Longitude, °	$[CH_4]$, ppbv	$\delta^{13}C$-CH_4, ‰ V-PDB	δD-CH_4 ‰ VSMOW	Potential Temperature, K	$[N_2O]$, ppb ATLAS**	$[N_2O]$, ppb ALIAS**	Notes
STRAT											
12/9/1996	86244	20.47	19.96	-158.10	1705	-47.16	-87.6	385	308.2	292.3	
12/9/1996	87401	20.15	19.09	-157.59	1399	-44.8	-66.6	459	242.0	242.1	
12/9/1996	87791	19.89	19.62	-157.75	1372	-44.52	-63.7	472	228.0	230.0	
12/9/1996	88170	17.10	20.16	-158.18	1326	-44.14	-65.0	483	215.6	219.8	
12/11/1996	84198	20.16	1.11	-155.55	1678	-46.72	-87.0	420	299.4	-	
12/11/1996	84922	20.05	0.09	-155.33	1718	-47.21	-84.7	361	308.2	-	troposphere
12/11/1996	85487	19.70	0.85	-155.36	1683	-46.9	-86.5	405	301.9	-	
12/11/1996	87305	18.51	4.07	-155.44	1658	-46.59	-89.8	455	298.7	-	
12/11/1996	89091	18.25	7.23	-155.47	1604	-46.26	-87.0	459	284.5	-	
12/11/1996	91193	15.74	11.08	-155.47	1534	-45.95	-79.1	470	268.0	-	
12/13/1996	71912	19.35	27.89	-145.95	1518	-45.88	-78.4	464	262.7	269.7	
12/13/1996	72860	17.51	28.85	-144.04	1638	-46.71	-85.5	420	294.3	296.4	
12/13/1996	73094	16.73	29.08	-143.55	1691	-47.12	-88.3	397	301.4	300.6	
12/16/1996	72049	15.74	58.46	-117.40	1553	-45.98	-81.2	425	271.2	273.4	
12/18/1996	80778	20.21	46.35	-127.41	1378	-44.56	-63.5	480	224.4	241.6	
POLARIS I											
4/24/1997	65523	20.47	42.56	-127.79	1392	-44.92	-62.0	486	230.8	222.0	
4/24/1997	71551	20.00	50.25	-140.30	1548	-46.31	-80.0	441	-	265.5	
4/24/1997	74472	16.98	55.85	-142.07	1368	-44.48	-60.3	519	224.7	218.1	
4/26/1997	63362	19.14	72.23	-148.01	1129	-41.83	-43.7	502	154.4	159.6	
4/26/1997	66687	19.58	79.03	-148.00	1468	-45.42	-74.9	506	249.2	248.8	

4/26/1997	68367	18.99	82.51	-148.00	1308	-44.03	-60.0	505	204.7	206.3	
4/26/1997	70058	19.17	86.12	-147.97	1018	-40.18	-32.4	502	127.8	132.9	Vortex edge
4/26/1997	71287	17.74	88.73	-147.52	882	-38.18	-11.3	501	96.5	102.2	Vortex edge
4/26/1997	72695	18.36	88.95	-136.27	1319	-43.96	-61.6	421	217.4	222.1	vortex
4/26/1997	72913	19.13	88.56	-140.68	1526	-46.24	-79.6	397	269.5	266.8	vortex
4/26/1997	73593	19.17	87.4	-145.84	1063	-41.03	-31.3	463	140.6	145.6	vortex
4/26/1997	73877	15.63	86.97	-146.63	1068	-41.48	-31.4	479	143.7	149.1	Vortex edge
4/26/1997	74365	19.21	86.14	-147.53	1007	-40.42	-	498	127.3	132.2	Vortex edge
4/26/1997	75270	14.38	84.53	-148.00	996	-40.03	-25.7	513	131.3	137.4	
5/6/1997	76553	19.36	74.24	-105.6	1269	-43.66	-55.6	513	198.4	205.2	
5/6/1997	81046	20.18	71.24	-126.51	1292	-44.08	-55.7	527	205.2	210.1	
5/9/1997	18283	19.42	64.41	-156.4	1363	-44.60	-60.6	498	223.1	226.1	
5/9/1997	25943	19.17	64.52	-153.24	1336	-44.22	-61.7	505	217.9	219.3	
5/11/1997	73375	15.71	64.02	-144.40	1653	-47.00	-84.6	330	-	299.8	
5/11/1997	76707	13.7	62.29	-148.79	1744	-47.23	-87.6	321	-	303.5	troposphere
5/11/1997	82306	11.26	62.94	-147.15	1606	-46.68	-81.4	388	291.7	281.0	
5/11/1997	83455	9.23	64.17	-144.76	1600	-46.46	-82.7	424	291.2	279.6	
5/11/1997	88383	8.65	64.27	-145.63	1633	-46.87	-83.2	357	303.1	298.7	
5/13/1997	77627	17.4	84.57	-113.85	1404	-45.05	-66.7	470	239.6	238.8	
POLARIS II											
6/26/1997	72651	18.55	75.49	-147.69	1245	-43.49	-58.1	488	195.4	190.0	
6/27/1997	74272	16.36	75.93	-147.65	1401	-44.84	-72.5	441	237.	235.5	
6/29/1997	89540	20.82	60.38	-137.61	884	-38.60	-23	527	104.1	102.5	Vortex filament
6/30/1997	78459	20.59	63.66	-147.85	1631	-46.72	-85.4	394	295.8	273.7	
6/30/1997	81592	18.61	66.48	-147.87	1501	-45.74	-82.8	480	260.3	253.7	
6/30/1997	84645	14.47	64.12	-147.85	803	-37.64	-	524	81.8	86.1	Vortex filament

*N_2O mixing ratios from the ATLAS instrument were used in the regressions. If the ATLAS measurement was unavailable, the measurement from the ALIAS instrument was used.

Table 3.ST3 Isotopic compositions of CH_4 from *Rice et al., 2003* and H_2 from *Rahn et al., 2003*

Flight Date mm/dd/yyyy	Collection Time Universal, s	Pressure-Altitude, km	Latitude, °N	Longitude, °	$[CH_4]$, ppbv	$\delta^{13}C$-CH_4, ‰ V-PDB	δD-CH_4 ‰ VSMOW	δD-H_2 ‰ VSMOW	H_2 (MS), ppb	Potential Temperature, K	$[N_2O]$, ppb ATLAS	Notes
SOLVE												
1/6/2000	85004	18.40	21.53	-120.00	1672	-47.08	-80.9	152	500	435	296.62	
1/11/2000	60753	11.40	43.48	-71.67	1726	-47.28	-87.4			358	307.92	
1/27/2000	44072	20.25	54.95	-34.14	1622	-46.47	-80.0			417	285.98	
1/27/2000	47949	16.95	61.39	-27.87	985	-39.81	-22.8			453	119.82	vortex
1/27/2000	52761	11.69	67.04	-21.82	1681	-47.00	-83.1			334	296.46	vortex
1/31/2000	43541	17.87	77.84	-13.36	1252	-43.40	-51.5	250	497	405	195.10	vortex
2/2/2000	42344	20.37	65.83	-63.05	1058	-40.81	-36.0	326	520	436	140.64	vortex
2/2/2000	54542	19.01	76.03	-14.97	1407	-44.82	-68.9	216	523	389	233.62	vortex
2/2/2000	57487	16.69	70.77	-18.90	914	-38.66	-13.2	364	493	451	102.23	vortex
2/3/2000	72462	19.74	72.77	-24.70	1475	-45.58	-77.2	183	587	376	252.27	vortex
2/3/2000	73291	18.60	72.29	-25.35	1366	-44.46	-62.5	226	554	391	224.08	vortex
2/3/2000	75852	16.76	71.59	-26.23	1158	-42.22	-43.9	206	546	420	167.73	vortex
2/3/2000	77896	15.65	71.44	-26.40	1057	-40.73	-30.7	315	515	439	140.27	vortex edge
2/3/2000	79959	13.51	68.39	-24.09	1663	-46.73	-81.0	124	489	349	292.46	
2/3/2000	80211	11.35	68.27	-23.27	1737	-47.23	-90.9	133	468	319	308.20	troposphere
3/5/2000	46199	19.94	74.85	-46.12	985	-39.99	-20.0	399	536	436	120.94	vortex
3/5/2000	51907	19.52	80.48	-12.90	752	-34.78	19.0			460	61.63	vortex
3/7/2000	41808	19.47	80.69	-50.68	888	-37.94	-11.1			444	95.81	vortex
3/7/2000	44309	19.19	82.16	-27.70	945	-39.09	-15.5			442	109.65	vortex
3/7/2000	44892	16.49	81.13	-25.71	1305	-43.94	-	247	459	393	208.25	vortex
3/7/2000	45191	15.95	80.59	-25.20	1453	-45.23	-70.2			384	244.87	vortex

3/11/2000	39893	20.19	59.38	-2.78	1604	-46.41	-80.3			422	281.65	
3/11/2000	41761	20.11	61.97	-1.87	1445	-44.93	-66.8			452	241.58	
3/11/2000	49504	20.36	70.12	-29.28	719	-34.22	22.7	438	508	460	52.99	vortex
3/11/2000	50510	20.24	71.86	-29.75	716	-34.05	26.4	356	531	461	51.77	vortex
3/11/2000	51523	19.07	73.6	-29.75	785	-35.91	15.7			457	69.29	vortex
3/11/2000	53534	17.21	73.45	-27.26	733	-34.30	18.3	403	460	463	56.9	vortex
3/12/2000	50149	19.74	78.91	-41.65	1099	-41.14	-34.0	316	493	421	151.93	vortex
3/12/2000	50600	19.84	79.14	-37.23	999	-39.73	-27.2	336	550	435	125.22	vortex
3/12/2000	51647	19.64	79.44	-26.83	854	-37.12	-4.7	397	608	448	87.18	vortex
3/12/2000	53681	19.13	79.02	-6.83	790	-35.78	12.9	386	418	454	70.11	vortex
3/12/2000	54697	18.32	77.53	-8.27	798	-36.00	11.0	378	563	453	71.9	vortex
3/16/2000	28815	16.77	67.40	-13.57	1614	-46.14	-81.2	161	534	426	283.47	

Table 3.ST4 Isotopic compositions of CO_2 from *Wiegel et al., 2013*

Flight date	UT, s	Altitude (km)	Latitude (°N)	N_2O (ppbv)	CO_2 (ppmv)	$\ln^{13}C$ (‰ VPDB)	$\delta^{17}O$ (‰ VSMOW-CO_2) *	$\delta^{18}O$ (‰ VSMOW-CO_2) *	$\Delta^{17}O$ (‰ VSMOW-CO_2) †
12/11/1999	78452	16.2	31.6	301	366.4	-8.11	21.9	41.43	0.1
12/11/1999	92199	11.2	35.0	315	367.2	-8.10	21.4	41.06	-0.3
1/6/2000	83678	19.6	24.0	281	365.5	-8.15	23.0	42.02	0.8
1/6/2000	90463	19.4	29.4	256	364.1	-8.14	24.1	42.52	1.6
1/9/2000	63083	20.1	40.6	211	362.0	-8.10	24.7	42.58	2.2
1/27/2000	38501	19.4	57.8	228	362.7	-8.13	24.5	42.82	1.9
1/27/2000	42165	19.5	51.7	222	362.5	-8.12	24.5	42.87	1.9
1/27/2000	44072	16.2	54.4	286	365.4	-8.11	22.2	41.72	0.2
1/27/2000	47949	20.2	60.0	120	360.0	-8.13	28.4	44.57	4.9
1/27/2000	52216	19.8	66.2	139	360.5	-8.20	27.7	44.08	4.4
1/27/2000	52761	12.3	67.0	296	366.0	-8.17	22.6	41.68	0.5
1/31/2000	39005	19.2	72.6	175	361.0	-8.15	25.9	43.14	3.2
1/31/2000	42070	19.5	77.9	149	360.5	-8.13	27.2	44.12	3.9
1/31/2000	43541	17.9	77.8	195	361.5	-8.11	25.2	43.12	2.4
1/31/2000	44628	18.3	76.0	180	361.1	-8.12	25.5	43.22	2.7
1/31/2000	46080	19.9	73.4	142	360.5	-8.14	26.8	43.65	3.7
2/2/2000	48616	19.6	73.7	145	360.5	-8.11	26.8	43.74	3.7
2/2/2000	53598	19.7	77.7	129	360.2	-8.16	27.9	44.13	4.6
2/2/2000	55680	19.3	74.0	150	360.5	-8.13	26.0	43.45	3.1
2/3/2000	73606	17.1	71.7	208	361.8	-8.11	25.0	42.97	2.3
2/3/2000	75105	17.6	70.4	193	361.3	-8.12	25.8	43.09	3.1
2/3/2000	77028	18.7	73.0	171	360.9	-8.11	25.9	43.36	3.0
2/3/2000	79886	14.5	68.4	293	366.0	-8.19	21.9	41.71	-0.1
2/3/2000	80167	11.7	68.3	305	366.2	-8.15	21.6	41.35	-0.2
2/26/2000	36727	19.0	73.3	149	360.8	-8.11	27.0	43.96	3.7
2/26/2000	44427	17.1	82.7	221	362.0	-8.13	23.7	42.73	1.1
3/5/2000	40019	16.8	68.2	241	363.6	-8.12	24.0	42.73	1.4
3/5/2000	50946	19.9	79.2	70	359.8	-8.11	29.5	45.26	5.6
3/11/2000	40682	17.2	60.5	279	365.0	-8.11	22.1	41.97	0.0
3/11/2000	46558	19.5	67.5	106	360.1	-8.13	28.1	44.40	4.6
3/12/2000	44489	19.1	70.1	109	360.2	-8.13	27.8	44.21	4.4
3/12/2000	50849	19.3	79.2	112	360.2	-8.17	28.6	44.57	5.1
3/16/2000	36822	18.5	61.9	232	363.1	-8.13	23.4	42.76	0.8
3/16/2000	41327	18.9	59.5	252	364.1	-8.12	23.0	42.00	0.8
3/16/2000	45827	19.2	55.8	216	362.5	-8.13	24.5	42.86	1.9

* The ^{17}O and ^{18}O isotopic compositions have been converted from the "natural log" values reported in Wiegel, et al. [2013] to "delta" values; the relationship between the two is $\ln^{18}O = \ln(\delta^{18}O+1)$.

† $\Delta^{17}O = \delta^{17}O - \lambda_{MD} \cdot \delta^{18}O$; $\lambda_{MD} = 0.528$

Table 3.ST5 Isotopic compositions of CO_2 from *Boering, et al.*, 2004

Flight date	Altitude (km)	Latitude (°N)	Potential Temperature (K)	N_2O (ppbv)	$\delta^{17}O$ (‰ VSMOW-CO_2)	$\delta^{18}O$ (‰ VSMOW-CO_2)	$\Delta^{17}O$ (‰ VSMOW-CO_2) *
970426	19.1	72.2	502	154	25.13	41.52	3.2
970426	19.2	75.6	503	187	23.70	40.27	2.4
970426	19.2	79.0	506	249	22.28	40.15	1.1
970426	19.2	82.5	505	205	22.93	39.78	1.9
970426	19.2	86.1	502	128	24.31	39.14	3.6
970426	19.1	88.7	501	97	26.19	40.76	4.7
970426	15.6	89.0	421	217	23.46	40.74	1.9
970426	17.7	87.4	463	141	26.28	42.71	3.7
970426	19.6	84.5	513	131	25.31	40.41	4.0
970506	16.8	78.2	461	263	22.28	40.63	0.8
970506	19.4	74.2	513	198	23.92	41.03	2.3
970509	19.4	64.5	505	218	23.71	41.40	1.9
970511	13.7	62.9	388	292	20.58	38.57	0.2
970511	11.3	64.3	357	303	21.11	39.78	0.1
970626	18.6	75.5	488	195	22.86	39.05	2.2
970626	16.4	75.9	441	237	21.74	38.54	1.4
970626	18.9	73.7	493	170	23.78	39.51	2.9
970626	18.4	57.4	472	223	23.15	40.84	1.6
970629	19.7	54.5	500	220	23.05	40.38	1.7
970629	20.5	48.4	505	239	23.06	41.03	1.4
970629	20.8	60.4	527	104	28.20	43.75	5.1
970630	14.5	63.7	394	296	19.24	36.43	0.0
970630	18.6	66.5	480	260	22.31	40.67	0.8
970630	20.6	64.1	524	82	28.61	43.57	5.6
970707	19.3	78.6	506	211	23.66	41.16	1.9
970707	19.4	81.6	504	205	23.37	40.34	2.1
970707	19.2	89.6	497	195	24.62	41.83	2.5
970710	15.8	64.0	421	274	21.83	40.38	0.5
970710	20.0	65.9	514	210	22.93	40.05	1.8

* $\delta^{17}O$ and $\delta^{18}O$ values reported in *Boering et al.*, 2004, were used to recalculate $\Delta^{17}O = \delta^{17}O - \lambda_{MD} \cdot \delta^{18}O$ using λ_{MD} =0.528, rather than λ_{MD} =0.516 as presented in *Boering et al*., 2004.

Table 3.ST6 Isotopic compositions of N_2O from balloon flights at 34°N in 2004 and 2005

Flight date	Altitude (km)	Latitude (°N)	Longitude (°)	N_2O (ppbv)	$\delta^{18}O$ (‰ VSMOW)	$\delta^{15}N$ (‰ AIR)	$\delta^{15}N^{\alpha}$ (‰ AIR) *
9/25/2004	33.343	34.55	-103.68	54.0	84.23	53.62	79.99
9/25/2004	32.224	34.56	-103.64	56.7	83.45	51.65	80.46
9/25/2004	31.502	34.56	-103.62	79.6	76.36	43.34	69.17
9/25/2004	30.778	34.58	-103.62	77.8	75.23	42.67	68.06
9/25/2004	29.954	34.59	-103.62	80.2	73.55	39.75	63.35
9/25/2004	29.26	34.59	-103.62	92.1	70.07	36.91	58.67
9/25/2004	28.734	34.59	-103.63	107.9	66.52	32.57	52.18
9/25/2004	28.047	34.59	-103.64	135.2	61.12	25.75	46.15
9/25/2004	27.275	34.59	-103.67	155.9	58.14	22.22	39.25
9/25/2004	15.324	34.69	-103.65	314.4	44.12	6.19	16.10
9/25/2004	26.545	34.58	-103.70	152.4	57.57	21.85	39.80
9/25/2004	25.766	34.56	-103.72	182.6	53.31	17.26	30.84
9/25/2004	24.987	34.57	-103.74	198.1	51.87	15.49	27.02
9/25/2004	24.265	34.58	-103.77	200.9	51.15	14.16	27.98
9/25/2004	23.545	34.57	-103.82	220.7	49.17	12.16	23.82
9/25/2004	22.713	34.56	-103.83	214.2	49.70	12.40	26.10
9/25/2004	21.931	34.58	-103.85	218.4	48.23	11.83	25.35
9/25/2004	21.195	34.57	-103.85	234.2	48.00	10.72	21.91
9/25/2004	20.551	34.58	-103.87	246.0	47.08	9.79	21.56
9/25/2004	19.741	34.60	-103.88	257.9	46.82	8.94	20.56
9/25/2004	18.977	34.60	-103.88	271.3	45.96	8.43	17.87
9/25/2004	18.150	34.62	-103.85	288.6	45.53	7.57	16.02
9/25/2004	17.431	34.64	-103.82	299.2	44.98	6.85	16.11
9/25/2004	15.992	34.67	-103.71	307.5	44.92	6.49	18.16
10/1/2005	32.89	34.85	-118.1	112.90	72.16	38.67	61.40
10/2/2005	31.77	34.89	-118.5	118.44	69.41	35.18	55.87
10/3/2005	30.85	34.93	-119.8	122.33	67.64	34.09	54.45
10/4/2005	29.92	34.95	-119.6	134.94	64.16	29.27	49.02
10/5/2005	29.06	34.97	-120.2	155.42	59.76	24.90	39.80
10/6/2005	27.29	34.98	-122.55	165.81	56.74	19.75	36.03
10/7/2005	26.55	34.99	-123.7	174.12	54.16	18.41	31.85
10/8/2005	24.80	35.03	-125.25	192.62	51.15	14.95	27.84
10/9/2005	24.04	35.05	-126.7	191.64	51.54	14.71	27.18
10/10/2005	23.30	35.06	-127.65	192.45	51.61	14.94	27.08
10/11/2005	22.66	35.08	-127.95	223.78	48.63	11.39	23.56
10/12/2005	21.95	35.1	-127.95	237.95	47.91	10.37	23.32
10/13/2005	21.34	35.11	-128.6	248.67	47.42	9.80	19.88
10/14/2005	20.72	35.12	-129.25	268.63	45.92	8.47	19.10
10/15/2005	20.19	35.13	-129.7	280.03	45.78	7.75	17.49

10/16/2005	19.56	35.12	-129.45	286.86	45.61	7.56	18.56
10/17/2005	18.35	35.14	-128.0	296.50	44.98	6.96	16.33
10/18/2005	17.78	35.15	-126.6	307.11	44.86	6.63	15.59
10/19/2005	17.18	35.17	-125.9	310.37	44.44	6.17	14.52
10/20/2005	15.90	35.19	-121.6	314.14	44.76	6.17	14.64
10/21/2005	15.34	35.20	-118.5	318.81	44.01	6.26	16.60

* $\delta^{15}N^{\alpha}$ are reported on the international air-N_2 scale [*Toyoda and Yoshida*, 1999]

Table 3.ST7 Isotopic compositions of N_2O from *Park et al., 2004*

Flight campaign	Flight date	Latitude (°N)	N_2O (ppbv)	$\delta^{18}O$ (‰ VSMOW)	$\delta^{15}N$ (‰ AIR)	$\delta^{15}N^{\alpha}$ (‰ AIR)*
POLARIS I	4/26/1997	80.8	225.0	49.1	12.1	24.25
	4/26/1997	84.3	139.7	57.1	21.2	38.78
	4/26/1997	87.4	107.9	60.8	25.4	46.19
	4/26/1997	87.9	207.9	50.0	12.9	25.88
POLARIS II	6/29/1997	62.0	83.3	62.6	27.7	46.70
	6/30/1997	64.3	257.4	47.0	9.6	21.61
	6/30/1997	62.9	103.1	60.7	25.1	44.77
	6/30/1997	65.8	104.2	58.2	23	39.59
	7/7/1997	88.5	267.3	46.6	9.3	19.28
	7/7/1997	75.0	78.7	59.8	24.5	40.61
	7/7/1997	73.1	134.4	53.3	16.7	31.47
	7/10/1997	63.6	154.8	53.7	17.5	34.00
POLARIS III	9/15/1997	64.6	226.3	49.3	11.9	24.36
	9/15/1997	65.0	205.8	49.7	12.5	25.37
	9/15/1997	64.7	288.8	45.5	7.7	17.75
	9/15/1997	64.8	313.0	44.6	7.2	16.23
	9/18/1997	78.5	185.9	49.3	13.7	27.71
SOLVE	1/23/2000	63.3	211.0	50.2	12.8	23.75
	1/23/2000	64.0	299.8	44.8	7.2	16.94
	1/23/2000	64.5	313.6	44.4	6.5	15.72
	1/27/2000	62.9	100.0	63.6	29.2	47.92
	1/27/2000	64.3	130.4	58.4	23.2	39.49
	1/27/2000	66.3	138.5	56.3	21.8	38.37
	2/2/2000	64.4	149.3	55.8	19.9	36.85
	2/3/2000	68.8	188.3	52.4	15.2	27.91
	3/5/2000	68.2	241.3	48.4	10.4	21.31
	3/5/2000	70.3	172.0	52.8	16.5	30.75
	3/11/2000	64.4	114.4	60.3	25.9	42.13
	3/11/2000	60.5	279.2	45.8	8.2	18.67
	3/11/2000	68.3	81.8	68.9	35.1	55.33
	3/11/2000	69.1	62.6	74.9	42.3	67.11
	3/11/2000	72.0	51.8	80.0	46.9	76.86

*$\delta^{15}N^{\alpha}$ values have been converted from the tropospheric N_2O scale as they appear in Park et al. [2004] to the international air-N_2 scale [*Toyoda and Yoshida*, 1999]

Chapter 4

Electronic quenching of O(^1D) by Xe: Oscillations in the product angular distribution and their dependence on collision energy

Adapted from an article with the same title, published in
The Journal of Chemical Physics, **143**, 054307 (2015) DOI: 10.1063/1.4927705
authored by Lauren A. Garofalo, Mica C. Smith, Paul J. Dagdigian, Jacek Kłos, Millard H. Alexander, Kristie A. Boering and Jim Jr-Min Lin

Abstract

The dynamics of the O(^1D) + Xe electronic quenching reaction was investigated in a crossed beam experiment at four collision energies. Marked large-scale oscillations in the differential cross sections (DCSs) were observed for the inelastic scattering products, O(^3P) and Xe. The shape and relative phase of the oscillatory structure depend strongly on collision energy. Comparison of the experimental results with time-independent scattering calculations show that this behavior is caused by Stueckelberg interferences, for which the quantum phases of the multiple reaction pathways accessible during electronic quenching constructively and destructively interfere.

4.1 Introduction

The kinetics of collisional quenching of electronically excited oxygen atoms, O(^1D), by rare gases has been extensively studied, motivated in part by its applications to the atmosphere and to chemical laser development.[1-2] The rate coefficients for electronic quenching increase as the atomic number of the rare gas increases, with that for Xe being $(7.2 \pm 1.4) \times 10^{-11}$ cm^3 molecule^{-1} s^{-1} at 298K.[3]

$$O(^1D) + Xe \rightarrow O(^3P) + Xe \qquad \Delta E = -45 \text{ kcal/mol} \qquad \text{(R1)}$$

The magnitude of this rate coefficient, near the gas kinetic collision limit, has been attributed to the strongly attractive potential for the $^1\Sigma^+$ state of XeO and to large nonadiabatic spin-orbit interactions between the singlet and triplet XeO potential energy curves.[4-6] Quenching of O(^1D) by Xe has a small activation energy of 0.10 ± 0.05 kcal/mol (Ref. 7), which is absent for O(^1D) quenching by Ar and Kr. These small or non-existent activation energies suggest that the curve-crossing point lies on the long-range attractive branch of the singlet potential energy curve rather than on the repulsive wall.[7]

Previously, fine-structure branching ratios for the quenching of O(^1D) to O(^3P_j) by Xe have been measured at a collision energy of 15.6 kcal/mol, yielding values of (0.28±0.04):(0.58±0.05):1 for the j=0: j=1: j=2 population ratios.[8] These measurements permit the study of the role of nonadiabaticity and the determination of cross sections of individual curve-crossing pathways in this reaction. To date, however, the dynamics of the quenching of O(^1D) by Xe, which can provide important constraints on the singlet and triplet XeO potential energy surfaces, has not been investigated experimentally.

Here, we report results for the O(^3P) and Xe product angular distributions from the O(^1D) + Xe electronic quenching reaction under single-collision conditions. The measured differential cross sections (DCSs) at several collision energies display pronounced oscillatory structure, revealing the quantum nature of this nonadiabatic process. Experimental and theoretical methods are described in Sec. 4.2; experimental results are presented in Sec. 4.3; and the origin of this quantum behavior is investigated by comparing the experimental results with high-level theoretical calculations (reported in the accompanying paper[9]) in Sec. 4.4.

4.2 Methods

4.2.1 Experimental Methods

The universal crossed molecular beam apparatus used in this study, shown in Fig. 4.1, has been described previously.[10-15] In this experiment, an atomic xenon beam and an atomic oxygen beam consisting of a 50:50 mixture of O(^1D) and O(^3P) were crossed at 90˚, and time-of-flight (TOF) spectra for the scattered Xe and O atoms were measured at a number of laboratory angles by a rotatable detector, as described in detail below.

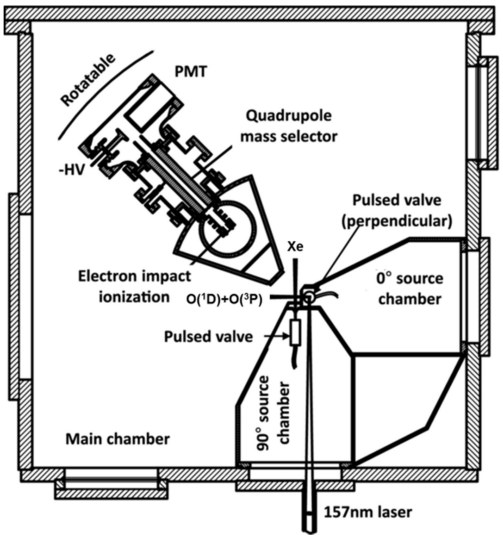

FIG. 4.1 Schematic of the universal crossed beam apparatus, modified with permission from Ref. 11. The angle between the Xe and O atom beams was fixed at 90˚. For the lowest collision energy of 7.3 kcal/mol, the pulsed valve for the O_2 source was rotated so that the O_2 beam was perpendicular to the reaction plane formed by the two crossed beams shown in the schematic. For the higher collision energies, the source valve was rotated toward the reaction plane, so that the photolysis products had a positive velocity vector in the direction of the collision point.

An atomic beam of 50% O(^1D) and 50% O(^3P) was generated by photolysis of a molecular beam of O_2 (Air Products, ≥99.6%) at 157.6 nm with a Lambda Physik LPX 210i F_2 laser (40 mJ/pulse, 50 Hz), a process that has been extensively studied by experimental and theoretical methods.[16-17] The O_2 molecular beam was produced using a pulsed valve (Even-Lavie) operated at a backing pressure of 70 psia. The O_2 beam was skimmed immediately before the laser interaction region, which was 40 mm downstream of the pulsed valve nozzle in the collision-free zone of the supersonic expansion, and the photolysis products were skimmed again before being introduced to the reaction chamber, reducing the width of the beam angular profile.

For the lowest O atom velocity studied, the O_2 beam source valve was oriented so that O_2 molecules escaped the valve in a direction perpendicular to the reaction plane formed by the two atomic beams (which always cross at 90˚ to one another); to achieve higher O atom beam velocities, the O_2 beam source valve was rotated toward the main chamber so that the O atoms produced via photolysis had a positive velocity in the direction of the reaction chamber, as described in previous studies using the same apparatus.[11-12,14] For this study, the average velocities for the O atoms produced in this manner were 2048±83 (half-width at half maximum at detector), 2208±84, 2373±87, and 2697±90 m/s, determined by measuring the TOF spectrum of the O atom beam (at m/z 8 for O^{2+}) at a laboratory angle of 0˚ in each case and calculating the velocity from the TOF delay combined with known electronic delays, laser delay, and distances in the crossed beam apparatus. The O atom beam had an angular divergence of 3.5˚ (cone half-angle at half maximum).

An atomic beam of Xe (Matheson Gas Products, 99.995%) was generated using a pulsed valve (Even-Lavie) operated at a backing pressure of 48 psia. The natural abundances of the most common Xe isotopes ^{128}Xe, ^{129}Xe, ^{130}Xe, ^{131}Xe, ^{132}Xe, ^{134}Xe, and ^{136}Xe are 1.9%, 26.4%, 4.1%, 21.2%, 26.9%, 10.4%, and 8.8% respectively.[18] A mass scan of the scattered products from m/z 120 to 140 showed the strongest signal at m/z 132; therefore, all Xe measurements were taken at m/z 132. The velocity of the Xe beam was 330±37 m/s (half-width at half-maximum at the crossing point), as measured by a movable fast-ionization gauge. The beam had an angular divergence of 2˚ (cone half angle at half maximum).

Upon exiting the source chambers, both atomic beams passed through apertures in a cryocooled copper plate (~25 K) to reduce background from ambient Xe or O_2 in the reaction chamber, thus improving the signal-to-noise ratio. Given the four initial O atom beam velocities noted above and the fixed-velocity Xe beam, the collision energies (E_{coll}) for the crossing beams were 7.3±0.2(1σ), 8.5±0.3, 9.8±0.3, and 12.6±0.4 kcal/mol. After collision, the reaction products traveled 242 mm from the crossing point to an electron impact ionizer. The $^{132}Xe^+$ or $^{16}O^+$ product ions were then selected by a quadrupole mass filter and measured by a Daly detector coupled to a multichannel scalar, which recorded the TOF spectra with a resolution of 1μs. To obtain TOF spectra at different laboratory angles, the detector was rotated about the collision center.

Laboratory angles were chosen to cover almost all center-of-mass (COM) angles at two collision energies of 7.3 and 9.8 kcal/mol and a subset of COM angles for two additional collision energies of 8.5 and 12.6 kcal/mol (as discussed further in Sec. 4.3). For E_{coll} = 7.3 and 9.8 kcal/mol, the TOF spectra for Xe (m/z = 132) were obtained at 21 and 22 laboratory angles, respectively, in the range of 15˚ to 75˚ and of 105˚ to 124˚ in increments of up to 5˚, with the direction of the O atom beam defined as 0˚. Because the TOF spectra peaks for scattered Xe at laboratory angles between 75˚ and 105˚ were obscured by high background from the Xe beam source, the TOF spectra for scattered O atoms (m/z = 16) were measured at a complementary set of laboratory angles between 30˚ and 80˚ in 10˚ increments. For E_{coll} = 8.5 and 12.6 kcal/mol, the TOF spectra for Xe were obtained at 13 and 19 laboratory angles ranging from 15˚ to 75˚.

To derive the DCS of Xe–O scattering from the measured TOF spectra, the peaks in the TOF spectra at each laboratory angle were integrated to obtain a raw scattering intensity in the

laboratory frame. This scattering intensity was then converted to the COM frame through a transformation Jacobian. In detail, the following procedure was used. First, the baseline – calculated as the average of the first 200 points of a Xe TOF spectrum and the first 60 points in an O atom TOF spectrum – was subtracted from each spectrum. Second, the peak(s) in each TOF spectrum for a given laboratory angle was (were) fit with a Gaussian function, and the mean and standard deviation (σ) from the Gaussian fit were then used to determine two sets of limits for integrating the TOF peak; each TOF peak was integrated from $\pm 2\sigma$ and from $\pm 3\sigma$. The peak area using the $\pm 2\sigma$ limits was multiplied by 1.044 and then averaged with the $\pm 3\sigma$ peak area (since for a true Gaussian distribution the area between $\pm 3\sigma$ should be 1.044 times larger than that for $\pm 2\sigma$) in order to obtain the best estimate for the scattering intensity in the laboratory frame that would not be sensitive to the choice of integration limits. We note that the difference between the adjusted $\pm 2\sigma$ area and the $\pm 3\sigma$ area for any given TOF peak varied from 2 to 15% depending on the signal-to-noise ratio and is likely determined by fluctuations in the baseline. We therefore use this difference to represent the experimental uncertainty associated with the peak integration. In addition, shot noise (about 3% for Xe and 10% for O) and fluctuations in laser power or beam intensities (~7%) also contribute to the overall uncertainty in the scattering intensities as a function of laboratory angle. Third, the laboratory-frame scattering intensities were converted to DCS as follows: the measured scattering intensity for a given laboratory angle Θ and laboratory-frame velocity v represents the number density of products in the electron-impact ionization detector, $N_{\text{lab}}(\Theta, \text{v})$, so that the scattered product flux in the laboratory frame, $I_{\text{L}}(\Theta, \text{v})$, is equal to $I_{\text{L}}(\Theta, \text{v}) = \text{v}\, N_{\text{lab}}(\Theta, \text{v})$. The relationship between scattered product intensity measured in the laboratory frame $I_{\text{L}}(\Theta, \text{v})$ and that in the COM frame, $I_{\text{COM}}(\theta, u)$, is given by the transformation Jacobian v^2/u^2, where θ is the COM angle and u is the COM velocity. Thus, conversion of the scattering intensities as a function of laboratory angle to a DCS as a function of COM angle is accomplished using Eq. (1):[19]

$$I_{\text{COM}}(\theta) = \cos\alpha \frac{u^2}{\text{v}} \int N_{lab}(\Theta, \text{v})\, d\,\text{v} \tag{1}$$

where α is the angle between the COM velocity vector u and the laboratory velocity vector v. The effect of the correction term $\cos(\alpha)$ is small in this study because the value of α is small for the highly exothermic quenching process (R1). Fourth, after the DCS angles were obtained for the scattered O and Xe atoms at a particular energy, the entire DCS for the scattered O atoms was multiplied by a single scale factor so that the DCSs for scattered Xe atoms and scattered O atoms at the three overlapping COM angles were comparable. The error estimates from the scattering intensities including baseline fluctuations, shot noise, and laser and beam fluctuations noted above were propagated through the COM conversion calculations and are given as 1σ error bars in figures showing the experimental DCSs in Sec. 4.3 below.

4.2.2 Theoretical Methods

Dagdigian *et. al.*[9] present full details of the calculation of the DCSs for $O(^1D) \rightarrow O(^3P)$ electronic quenching in the accompanying paper; a brief summary is provided here. Electronic structure calculations were carried out to obtain the potential energy surfaces for the $^1\Sigma^+$, $^1\Pi$, and $^1\Delta$ electronic states correlating with the $O(^1D)$ + Xe asymptote and the $^3\Sigma^-$ and $^3\Pi$ electronic states correlating with $O(^3P)$ + Xe. Two sets of calculations of these potential energy surfaces were performed: one using an internally contracted multi-reference configuration interaction

method [MRCISD+Q] and one using an unrestricted coupled cluster calculation [UCCSD(T)]. Because the $^1\Pi$ state cannot be described by a single restricted-Hartree-Fock reference, it was not possible to carry out a UCCSD(T) calculation for the $^1\Pi$ state. Therefore, the MRCISD+Q potential energy curve for the $^1\Pi$ state was used with the UCCSD(T) potential energy curves in the scattering calculations labeled "UCCSD(T)" in Figs. 4.10 and 4.11 shown below.

The potential energy curves for these two sets of calculations are shown in Fig. 1 of the accompanying paper[9] and are shown here in Fig. 4.2 for convenience. The $^1\Sigma^+$ state was found to have a deep potential well, while all the other states are primarily repulsive with much smaller van der Waals wells. The computed dissociation energy D_e of the $^1\Sigma^+$ state is strongly affected by the degree of electron correlation recovered in the calculation: 10227 cm^{-1} for MRCISD+Q and 13366 cm^{-1} for UCCSD(T). The spin-orbit matrix elements within the triplet manifold and between the singlet and triplet states were computed using MRCI wave functions and the MRCISD+Q energies. These matrix elements increase strongly from their asymptotic values for internuclear separations $R < 4$ bohr.

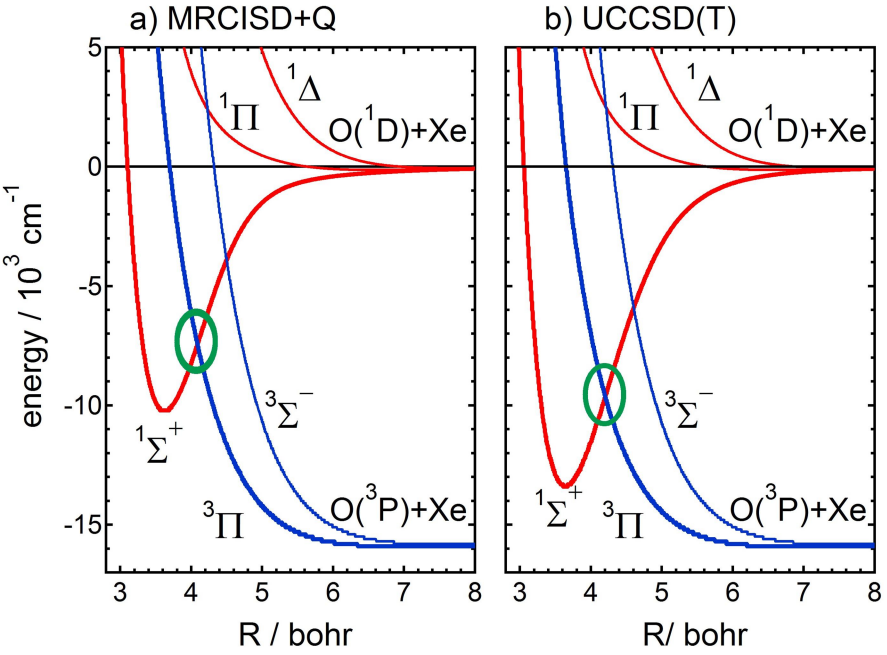

FIG. 4.2 Potential energy curves for the O-Xe system calculated using the (a) MRCISD+Q and (b) UCCSD(T) methods, identical to those shown in Fig. 1 of the accompanying theory paper (Ref. 9). The green circle indicates the most relevant curve crossing.

Quantum scattering calculations employing the UCCSD(T) and MRCISD+Q potential energy curves and spin-orbit matrix elements were carried out in a space-fixed basis. Integral and differential cross sections for O(^1D,^3P) + Xe collisions were performed as a function of the collision energy. By averaging the energy-dependent quenching cross sections over a Boltzmann distribution of collision velocities, and summing over all O(^3P_j) fine-structure levels, we determined a quenching rate coefficient of 2.20×10^{-11} cm^3 molecule^{-1} s^{-1} at 298 K.[9] This value is the same order of magnitude but lower than measurements at 298 K, which range from (5.0 ± 0.5) to (7.2 ± 1.4) × 10^{-11} cm^3 molecule^{-1} s^{-1} (Refs. 20 and 3, respectively).

4.3 Experimental Results

Time-of-flight spectra measured for Xe atoms at a collision energy of 9.8 kcal/mol are shown in Fig. 4.3 for 8 of the 22 laboratory angles measured, and TOF spectra for O atoms at the same collision energy are shown in Fig. 4.4 for all 6 laboratory angles measured. TOF spectra at laboratory angles not shown in Fig. 4.3 appear in supplementary material.[21] Two peaks are observed in both the Xe and O atom TOF spectra for most laboratory angles. The fast Xe and O atom peaks in the TOF spectra correspond to scattered products with kinetic energies far above the collision energy limit of 9.8 kcal/mol, resulting from electronic quenching of $O(^1D)$ to $O(^3P)$ in reaction (R1), which releases 45 kcal/mol that is then partitioned into the kinetic energies of the scattered atoms. The slow Xe and O atom peaks in the TOF spectra correspond to products from a combination of reactions (R2) and (R3), in which the O atom remains in the same electronic state after the collision:

$$O(^1D) + Xe \rightarrow O(^1D) + Xe \quad \text{(R2)}$$
$$O(^3P) + Xe \rightarrow O(^3P) + Xe \quad \text{(R3)}$$

We will refer to the combination of reactions (R2) and (R3) as 'elastic scattering', and to (R1) as 'inelastic scattering'. Because mass spectrometry cannot discern the electronic state of the O atom, the $O(^1D)$ and $O(^3P)$ products of elastic scattering in (R2) and (R3) are indistinguishable and the branching ratio for reactions (R2) versus (R3) cannot be determined in this experiment.

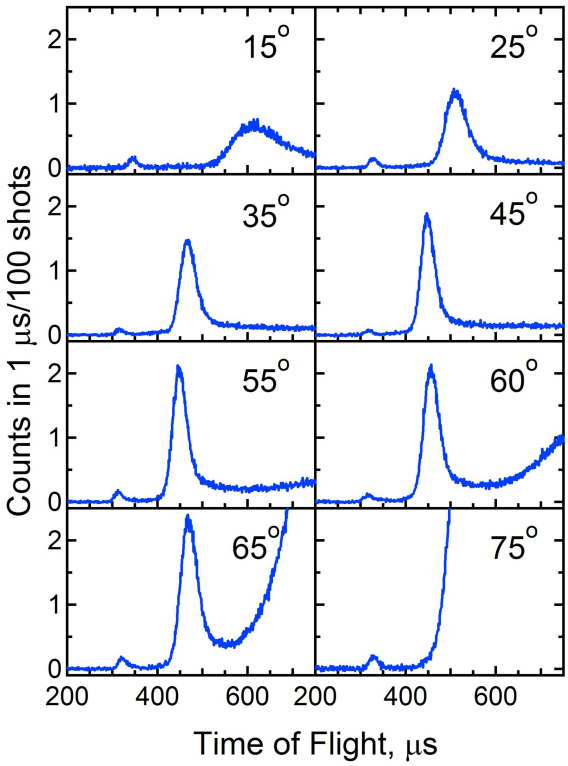

FIG. 4.3 Baseline-subtracted time-of-flight spectra for m/z=132 (Xe atoms) at a collision energy of 9.8 kcal/mol for 8 of the 22 laboratory angles measured. The fast peak at ~ 325 μs corresponds to high kinetic energy Xe produced by the inelastic scattering reaction (R1) [$O(^1D)$ + Xe → $O(^3P)$ + Xe]. The slow peak, for which the time of flight varies with angle, corresponds to elastically scattered Xe from a combination of reactions (R2) [$O(^1D)$ + Xe → $O(^1D)$ + Xe] and (R3) [$O(^3P)$ + Xe → $O(^1D)$ + Xe]. The background due to unscattered Xe increases as laboratory angle increases toward 90° (see Sec. 4.3).

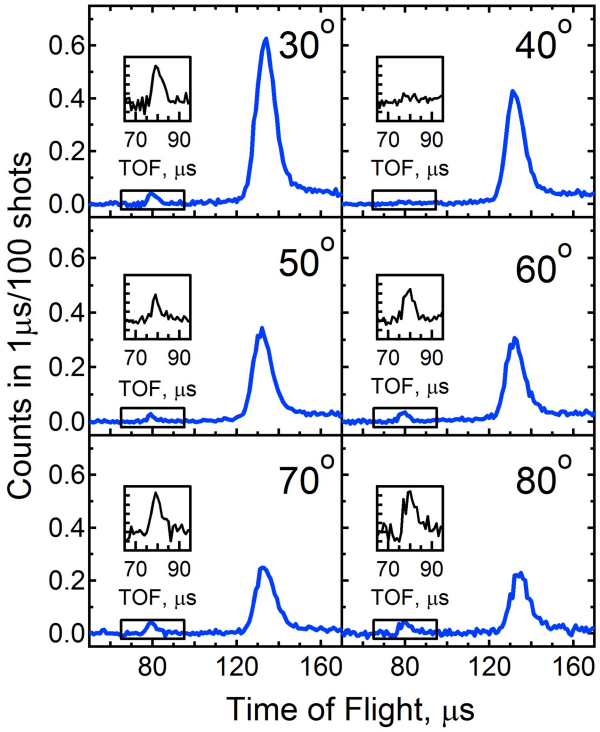

FIG. 4.4 Baseline-subtracted TOF spectra for m/z =16 (O atoms) at a collision energy of 9.8 kcal/mol for all six laboratory angles measured. The fast peak at ~ 80 μs, enlarged in the inset, corresponds to the inelastically scattered O(^3P) atoms from reaction (R1). The slow peak at ~135 μs corresponds to a combination of the elastically scattered O(^1D) and O(^3P) atoms from reactions (R2) + (R3).

Examination of Fig. 4.3 shows that the Xe background increases as the laboratory angle increases toward Θ=90˚, obscuring the slow Xe peak for Θ > 70˚ and the fast Xe peak for 75˚ < Θ < 105˚. The higher background is caused by divergence of the Xe beam and Xe atoms escaping from the cold plate in this direction, as discussed for previous experiments on other systems using this apparatus.[12-15] The Newton diagram for inelastic scattering at a collision energy of 9.8 kcal/mol, shown in Fig. 4.5, demonstrates that the O atom TOF data measured at the angles selected for this study complement those missing due to high background in the Xe TOF data. Specifically, the laboratory angles between 75˚ and 105˚ at which background Xe obscures the scattered Xe peaks correspond to COM angles of 40˚ to 80˚, while this COM range corresponds to scattered O atoms at laboratory angles between 33˚ and 72˚. Therefore, measuring TOF spectra for O atoms at lab angles from 30˚ to 80˚ (which are not affected by high O atom background since they are far from the O atom beam at 0˚) provide the COM scattering information missing from the Xe data set due to high Xe background near 90˚. Thus, for a collision energy of 9.8 kcal/mol, the combination of Xe and O atom TOF spectra the angles measured result in near-complete COM-frame angular coverage of 10˚ to 180˚ for inelastic scattering (R1) and 35˚ to 175˚ for elastic scattering [(R2) + (R3)]. This near-complete angular coverage in the COM frame at 9.8 kcal/mol is evident in Fig. 4.6 for elastic scattering [(R2) + (R3)] and in Fig. 4.7 for inelastic scattering (R1), in which the relative integrated peak intensities for scattered Xe and O atoms in the laboratory frame are shown and compared with the DCSs in the COM frame using the transformation described in Sec. 4.2.

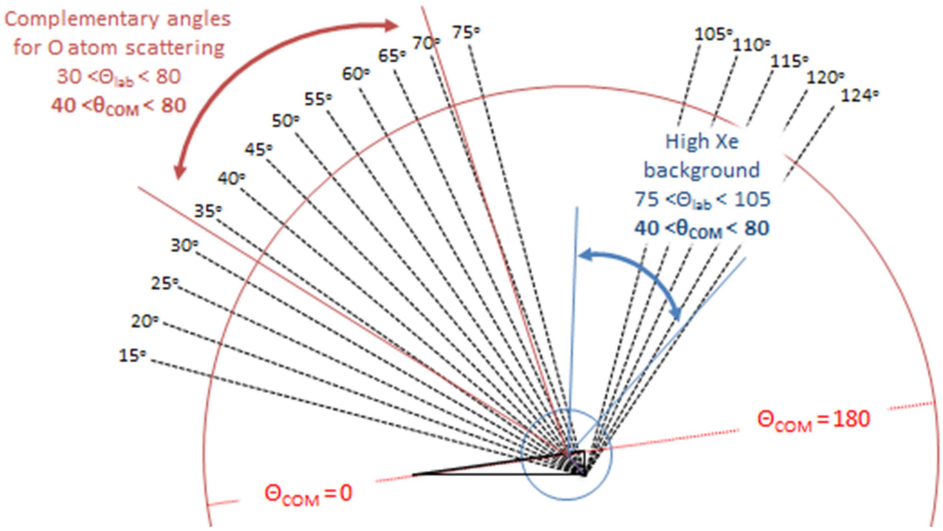

FIG. 4.5 A Newton diagram for O + Xe interactions at a collision energy of 9.8 kcal/mol. The circles indicate the speeds for O (red) and Xe (blue) atoms resulting from the electronic quenching of O(^1D) by Xe (R1). The black dotted lines indicate the 22 laboratory angles at which the Xe scattering spectra were measured. The blue curved arrow indicates the laboratory and COM angles at which the Xe background is high; the red curved arrow shows the laboratory and COM angles for the scattered O atom that are complementary to the high background Xe angles in blue.

Comparison of the DCSs for the elastic and inelastic scattering processes reveals unusual behavior in the dynamics of the electronic quenching reaction. Figure 4.6(c) shows that the DCS for the combination of products from elastic scattering reactions [(R2) + (R3)] has a forward scattering bias and a smooth monotonic decay toward larger scattering angles, consistent with the dynamics expected for classical or semiclassical scattering of two atoms. In contrast, Fig. 7(c) shows that the DCS for the products of inelastic scattering (R1) exhibits broad, large-angle oscillations as a function of the COM scattering angle θ. The magnitude of these broad oscillations far exceeds the 1σ error bars of the data (discussed in Sec. 4.2.1). The fact that these oscillations are present in the DCS for inelastic scattering but absent in the DCS for elastic scattering indicates that these oscillations are not likely to be artifacts caused by the experimental set-up (*e.g.*, by blocked signals at some angles or a significant contribution from the Xe dimer) but, rather, represent a real phenomenon resulting from the collision dynamics of electronic quenching of O(^1D) by Xe.

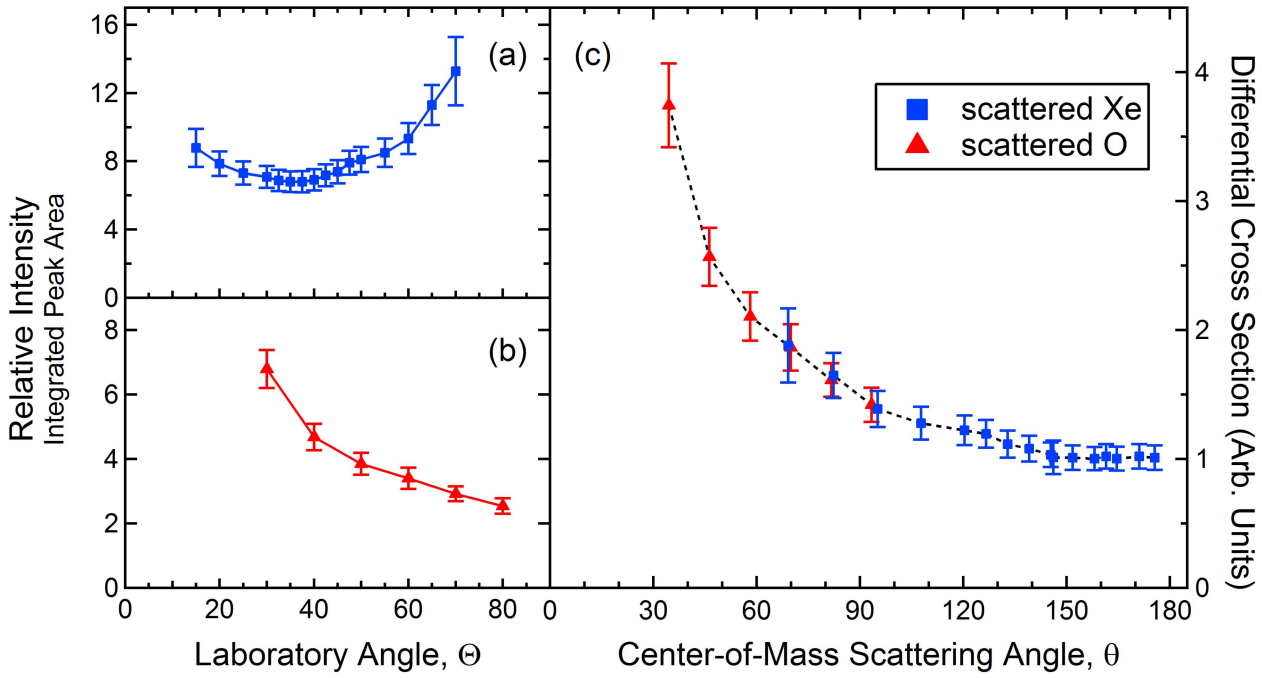

FIG. 4.6 Integrated peak areas (see Sec. 4.2.1) at a collision energy of 9.8 kcal/mol for the combination of elastically scattered products from $O(^1D)$ + Xe → $O(^1D)$ + Xe (R2) and $O(^3P)$ + Xe → $O(^3P)$ + Xe (R3). These were determined from the TOF spectra as a function of laboratory angle for (a) the Xe peaks and (b) the O atom peaks. (c) The COM frame intensities for Xe atoms (blue squares) and O atoms (red triangles) from the transformation of the laboratory-frame peak areas shown in (a) and (b). The 1σ error bars shown are estimated from uncertainties due to peak integration limits, as well as shot noise and fluctuations in laser power and beam intensity (see Sec. 4.2.1).

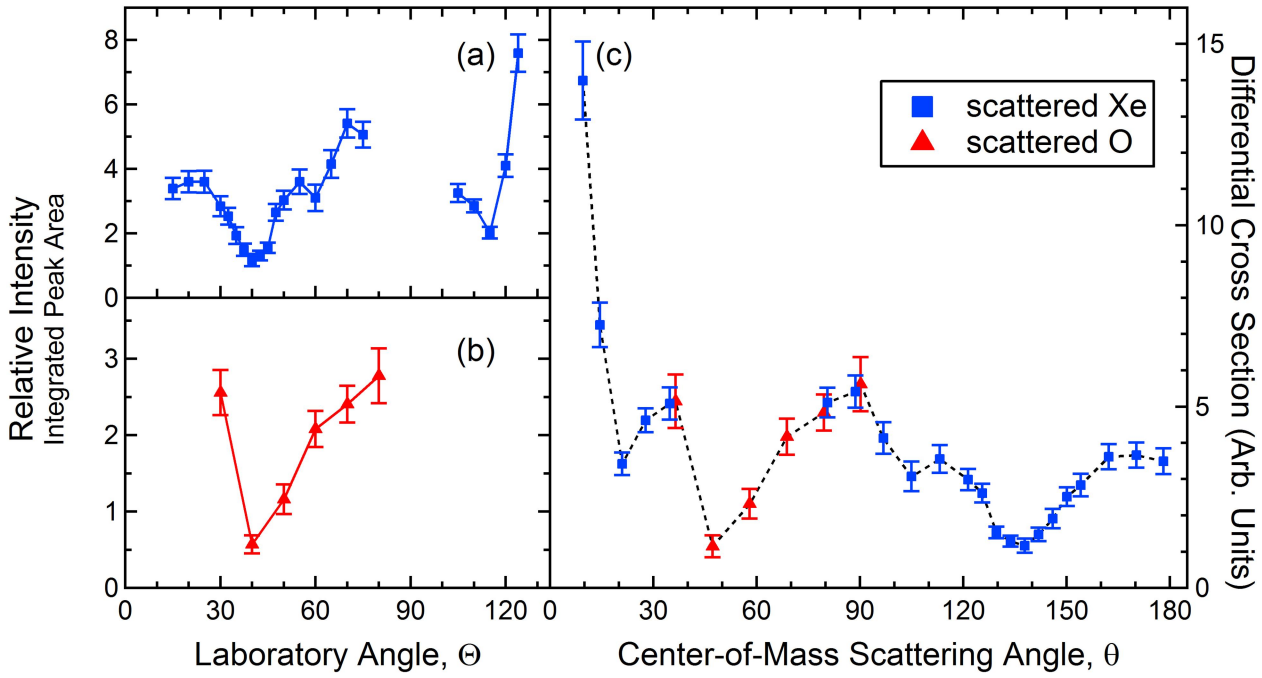

FIG. 4.7 Integrated peak areas, similar to those in Figure 4.6, for the products of the quenching reaction O(^1D) + Xe → O(^3P) + Xe (R1) at a collision energy of 9.8 kcal/mol. As in Fig 4.6, these were determined from the TOF spectra as a function of laboratory angle for (a) the Xe peaks and (b) the O atom peaks. (c) The COM frame intensities for Xe atoms (blue squares) and O atoms (red triangles) from the transformation of the laboratory-frame peak areas from (a) and (b). The 1σ error bars are shown.

In addition to the results at E_{coll} = 9.8 kcal/mol presented above, the DCS for products of inelastic scattering of O(^1D) by Xe [(R1)] was also determined for a near-complete COM angular distribution at a collision energy of 7.3 kcal/mol, as well as for COM angles between 80˚ and 180˚ at collision energies of 8.5 and 12.6 kcal/mol. TOF spectra and integrated peak intensities as a function of laboratory angle at these additional collision energies are shown in supplementary figures.[21] Figure 4.8 shows the DCS for inelastic scattering at 7.3 kcal/mol relative to that at 9.8 kcal/mol [shown also in Fig. 7(c)]. Figure 4.9 shows the DCS for inelastic scattering from 75˚ to 180˚ at four collision energies: 7.3, 8.5, 9.8, and 12.6 kcal/mol. Comparison of the DCSs at the different collision energies in Figs. 4.8 and 4.9 reveals that both the shape and the phase of the oscillations in the COM angular distribution for the inelastic scattering of O(^1D) by Xe change significantly with collision energy.

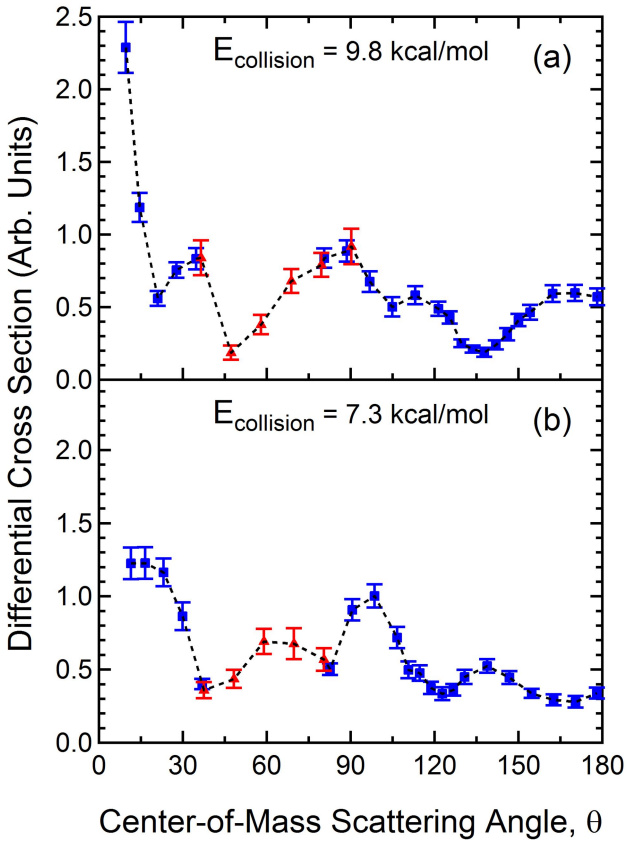

FIG. 4.8 Differential cross section (DCS) for scattered Xe (blue squares) and O (red triangles) atoms from $O(^1D)$ + Xe → $O(^3P)$ + Xe [reaction (R1)] as a function of COM angle at a collision energy of (a) 9.8 kcal/mol and (b) 7.3 kcal/mol.

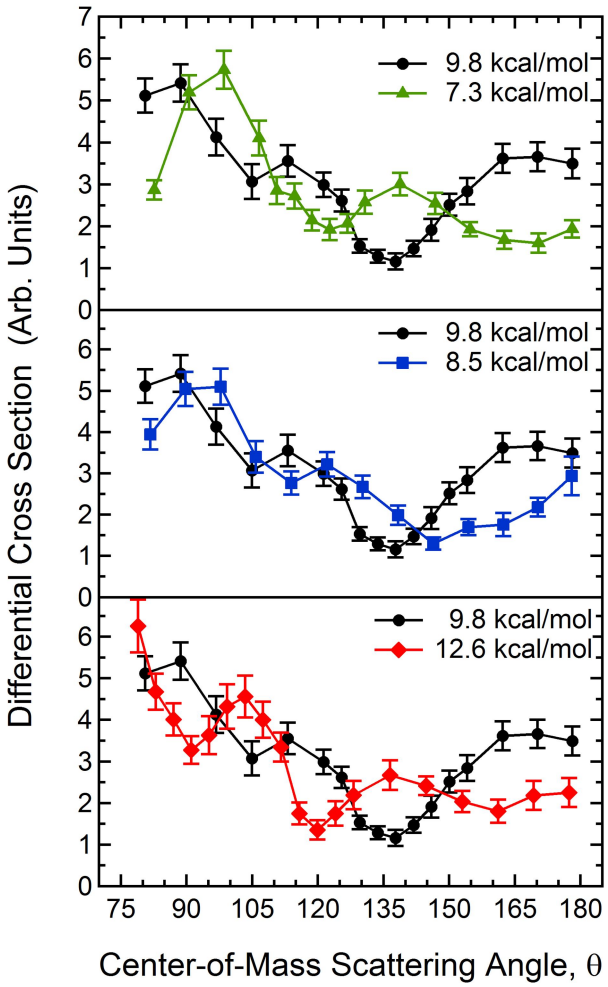

FIG. 4.9 The differential cross sections (DCSs) for scattered Xe from the electronic quenching reaction (R1) as a function of COM angle between 75˚ and 180˚ at four collision energies, showing significant changes as a function of collision energy. For clarity and to better illustrate how the oscillations in the angular distribution change with collision energy, the DCS at a collision energy 9.8 kcal/mol has been plotted in each panel along with the DCS at a second collision energy. Note the nearly 180˚ 'phase' shift when collision energies change by 2.6 kcal/mol.

4.4 Discussion and Comparison with Theory

The broad, large-scale oscillations of the measured DCSs at several collision energies are reminiscent of Stueckelberg oscillations. First described in the 1930s,[22] these oscillations, a consequence of quantum interference, have been observed for systems in which two distinct curve crossing pathways exist. Stueckelberg oscillations have been detected and identified in collisions of electronically excited alkali atoms with rare gases,[23-24] in the inelastic relaxation of Ba $6s6p$ ($^1P_1 \rightarrow {}^3P_2$) in collisions with argon,[25] and in double-electron capture in collisions of slow $C^{4+}(1s^2\ {}^1S)$ with He.[26] In calculating the probabilities for charge transfer in collisions of He^{2+} with H atoms Stolterfoht *et al.* [27] draw an analogy between the quantum interferences that cause Stueckelberg oscillations and the interferences which characterize Young's double-slit diffraction experiment.[28-29]

To investigate the origin of the slow, large-scale oscillations measured in this experiment, we used fully-quantum time-independent scattering calculations to determine DCSs using two sets of potential energy curves [MRCISD+Q and UCCSD(T)], as described in Sec. 4.2.2. and in the accompanying paper.[9] For both sets of potential energy curves, slow, large-scale oscillations in the calculated DCSs are predicted at the collision energies of the experiment, as shown in Fig. 4.10(a) and 4.10(b), on which smaller magnitude, fast oscillations are superimposed. The slow oscillations can be attributed to quantum interference between multiple classical reaction pathways, as demonstrated for the Xe–O system by a simplified two-state model in the accompanying paper.[9] (The fast, small-angle oscillations are caused by interference between attractive and repulsive trajectories that lead to the same laboratory scattering angle, are known as "diffraction" oscillations, and are not unusual.)[9] Even though electronic quenching of O(^1D) to O(^3P) can occur by several distinct spin-orbit couplings (e.g., $^1\Sigma^+ \rightarrow {}^3\Pi$, $^1\Sigma^+ \rightarrow {}^3\Sigma^-$, $^1\Pi \rightarrow {}^3\Sigma^-$; see Fig. 2 and Fig. 1 of Ref. 9), the two-state model indicates that slow oscillations similar to those in the experiment result from interferences associated with just the $^1\Sigma^+ \rightarrow {}^3\Pi$ curve crossing, which accounts for 90% of the spin-orbit quenching in this system at thermal collision energies.[9] This singlet-to-triplet transition can occur either as the atoms approach or as they separate. Each pathway accumulates a unique quantum phase, and constructive or destructive interference between these phases gives rise to the broad oscillatory variation with angle. As detailed in Sec VI.A. of the accompanying theory paper,[9] these slow, large-scale oscillations disappear when the interferences are artificially removed from the calculation, providing additional evidence that the slow oscillations in the DCSs are due to Stueckelberg interferences. The calculated DCSs are clearly extremely sensitive to the potentials used – a point we will return to in the discussion below – but both sets of DCSs exhibit Stueckelberg oscillations.

For comparison, the experimental DCSs are shown below the calculated DCSs in Fig. 4.10(c) and 4.10(d). Several key qualitative features of the experimental results are captured by theory – in particular the broad, slow oscillations with scattering angle whose phases depend on collision energy. (Note that the angular resolution of the apparatus cannot resolve the predicted fast oscillations.) A more quantitative comparison between the experimental and calculated results reveals notable similarities as well as differences. The magnitudes of the change in collision energy for which the oscillations shift to being 180˚ out of phase are comparable. For example, the experimental DCS shifts phase by ~180˚ when the collision energy changes by ~2.6 kcal/mol (*i.e.,* from 7.3 to 9.8 kcal/mol and from 9.8 to 12.6 kcal/mol), while the calculated DCS shifts phase by ~180˚ when the collision energy changes by ~ 2.9 kcal/mol. A notable difference, however, is the deep minimum near $\theta = 90^\circ$ which is present in the calculated DCSs for both sets of potential curves, but is absent in the experimental DCSs. In other words, the theoretical results show a deep minimum in 'sideways scattering' near 90˚ that is quite invariant over a range of collision energies while the experimental results near 90˚ exhibit a shift in phase with collision energy but not a minimum.

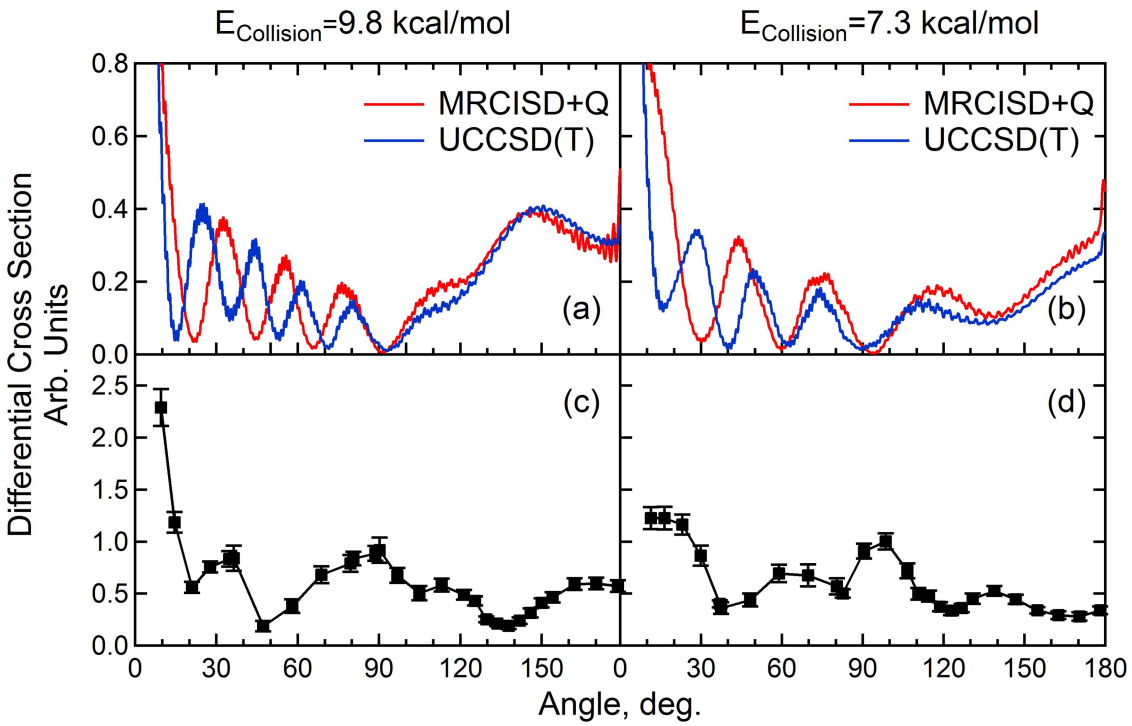

FIG. 4.10 Computed differential cross sections (DCSs) for the O($^1D \rightarrow {}^3P$) transition, summed over the fine-structure levels of the ^3P_j product, induced by collision with Xe at collision energies of (a) 9.8 and (b) 7.3 kcal/mol. The cross sections displayed in red and blue were computed with the MRCISD+Q and UCCSD(T) potential energy curves (see Sec. 4.2.2.). The experimental results for collision energies 9.8 kcal/mol – Fig. 4.8(a) – and 7.3 kcal/mol –Fig. 4.8(b) – are shown here for comparison.

A number of other differences are also evident in Fig. 4.10, both between theory and experiment and between calculations using the two different sets of potential energy curves. Indeed, the lack of quantitative agreement between experiment and theory in the angular dependence of the DCSs may be due to the system's great sensitivity to details of the potential energy curves. Figure 4.10, for example, shows that calculations using the two levels of theory [MRCISD+Q and UCCSD(T)] for the potential energy curves produce DCSs with large-scale oscillations that are nearly 180˚ out-of-phase and have different spacings between peaks and valleys. A major difference between the PES calculated with MRCISD+Q and UCCSD(T) is that UCCSD(T) PES has a significantly deeper well. The DCS calculated with UCCSD(T) PES has smaller spacings (i.e., more cycles over a given range of angles) and may indicate that a larger phase difference between the classical reaction pathways has accumulated.

We have also considered other possibilities that may account for some of the differences between the experimental and calculated DCSs. Since the theoretical DCSs presented here show that the shape and phase of the oscillations are extremely sensitive to the collision energy, we considered whether the small spread in the collision energy in the experiment, due to the spreads in velocity and angle of the incident beams, might affect the results. Van Wyngarden *et al.*[11] recently showed, for example, that using the experimental distribution of collision energies instead of a fixed average collision energy in both quantum statistical and trajectory calculations vastly improved agreement between experimental and calculated results for the dynamics of the

$O(^3P)$ + O_2 isotope exchange reaction. Figure 4.11 displays the DCSs computed with the UCCSD(T) potential energy surfaces at collision energies of 9.8 and 7.3 kcal/mol (as in Fig. 4.10) and at $+2\sigma$ and -2σ of these mean collision energies. The extrema in the theoretical DCSs change with collision energies about the mean values, but the minimum near $\theta = 90^\circ$ appears at all energies in this range. Thus, the spread in experimental collision energies does not explain the theory-measurement discrepancy in sideways scattering.

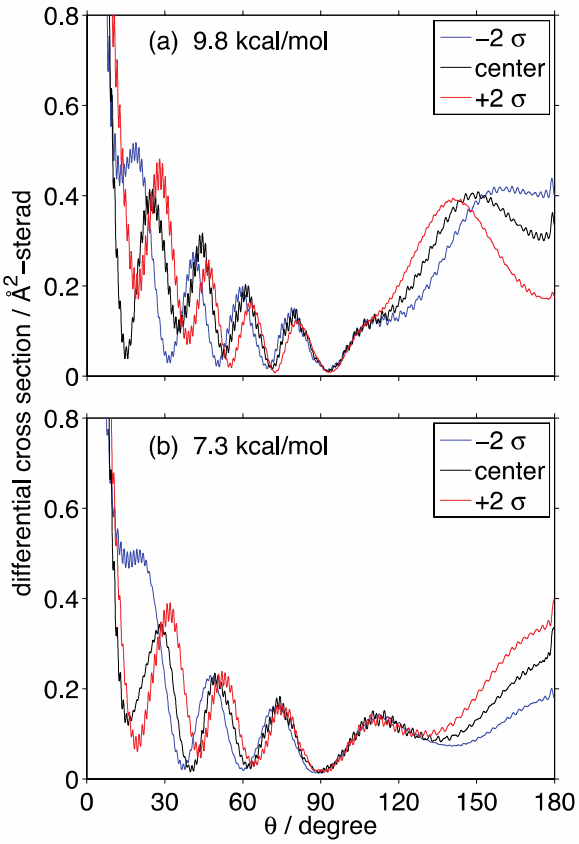

FIG. 4.11 Computed differential cross sections (DCSs) for the $O(^1D \rightarrow {}^3P)$ transition using the UCCSD(T) potential energy curves calculated at the mean experimental collision energy of (a) 9.8 and (b) 7.3 kcal/mol from Figure 4.10 (black lines), compared with computed DCSs calculated at a collision energy of the experimental mean$+2\sigma$ (red lines) and the experimental mean-2σ (blue lines).

Another possible source of the discrepancies between the experimental and theoretical results that we considered is a stronger contribution of the $^1\Pi \rightarrow {}^3\Sigma^-$ curve-crossing pathway that may be accessed at the non-thermal energies of the experiment than is represented in the DCS calculations shown in Fig. 4.10. A way to test this hypothesis and provide additional benchmarks for theory is given by the theoretical results in Ref. 9. The calculations show that coupling between the $^1\Sigma^+$ and $^3\Pi$ states, which dominates at thermal energies, preferentially yields $O(^3P_j)$ products in the j=0 and j=2 fine-structure levels. At collision energies greater than ~5.7 kcal/mol, the $^1\Pi \rightarrow {}^3\Sigma^-$ crossing becomes energetically accessible, allowing formation of $O(^3P_{j=1})$. Thus, measurement of fine-structure-resolved DCSs – not possible in this study since the ^3P_j state

cannot be distinguished with mass spectrometry – would yield insight into the importance of the $^1\Pi \rightarrow {}^3\Sigma^-$ crossing that uniquely produces O($^3P_1$).

Finally, we considered the possible impact of (1) polarization of the O(^1D) atoms, (2) a contribution of fast O(^{3}P) atoms from the minor (0.5%) O_2 photolysis channel at 157 nm producing two O(^{3}P) atoms,[16] and (3) the formation of Xe dimers on the experimental DCSs. We do not believe that any of these processes affect the overall shape of the DCSs under our experimental conditions. For the case of O(^1D) polarization, we note that O(^1D) atoms produced by the photolysis of O_2 at λ=157 nm are known to exhibit significant polarization for which the m_j=0 state dominates.[30] Because the time between O_2 photolysis and the O–Xe collision in this experiment (about 16 μs) is longer than the period of the Larmor precession in Earth's magnetic field (about 1 μs), it is likely that polarization of the O(^1D) atoms is scrambled but perhaps not fully randomized before the O(^1D) atoms collide with the Xe. The DCS calculations shown in Fig. 4.10 assumed that O(^1D) is not polarized. To test the sensitivity of the oscillatory behavior to possible polarization in the extreme case, the scattering calculations for reaction (R1) were modified so that m_j=0 in the O(^1D) atom. The resulting DCS (not shown) contained large-scale oscillations that closely match those in the full DCS. Thus, since the theoretical DCS for polarized O(^1D) and non-polarized O(^1D) were similar, it is unlikely that polarization of O(^1D) produced from O_2 photolysis affected the experimental DCS or caused a significant difference between the experimental and theoretical DCSs. For (2), we detected no TOF peaks that would correspond kinematically to elastic scattering between Xe and any O(^{3}P) produced by the minor O_2 photolysis channel, consistent with our assumption that this channel is too small to affect our results. For the case of Xe dimer formation, the Xe beam was operated under conditions in which Xe dimers could have formed; however, it is unlikely that collisions of O(^1D) with Xe dimers contributed to the scattering signals ascribed to (R1) or to (R2) + (R3). First, upon collision, the Xe dimer would likely dissociate, and the products of this three-body process – i.e., Xe_2 + O(^{1}D) $\rightarrow$ Xe + Xe + O(^{3}P) – would appear as broad features in the TOF spectra due to their broad velocity distributions. Because a baseline is subtracted from each spectrum before its peak areas are determined, contributions from any Xe dimer collision products in the signal intensities reported are likely minimal. Second, in the improbable case that a Xe dimer survives collision, the energy and momentum partitioning for the Xe_2 + O scattering system would be significantly different from that for the Xe + O scattering system because the much larger mass of the Xe dimer results in a large shift in the system's center of mass. The expected differences in the COM- and laboratory-frame velocities of the products are large and detectable; at 9.8 kcal/mol, for example, the difference in COM velocities for Xe vs Xe_2 is 122 m s^{-1}. Thus, this two-body process with rigid energy and momentum constraints should result in an additional peak, which was not detected. In either the 3-body or 2-body case, then, the presence of any Xe dimer is not expected to interfere significantly with our determination of the angular distribution of the products of Xe+O scattering.

Despite the quantitative differences, the DCSs from theory and experiment point to Stueckelberg oscillations as the origin of the slow, large-scale oscillations in the angular distributions of the products of inelastic scattering between O(^{1}D) and Xe (R1) – a manifestation of quantum interference between the two pathways in which quenching occurs either as the atoms approach or as they separate. Stueckelberg oscillations in other systems are known to be extremely sensitive to small variations in collision energy, as well as to the subtle details of the

underlying potential energy curves, especially in the curve-crossing region. Thus, we expect that further comparison and analysis of the measurements and calculations shown here for O(^1D) + Xe will provide additional insight and constraints on the XeO potential energy curves and their couplings.

4.5 Conclusion

The angular distributions of the inelastically scattered products from crossed atomic beams of O(^1D) and Xe (R1) were investigated at collision energies of 7.3 ± 0.2 (1σ), 8.5 ± 0.3, 9.8 ± 0.3, and 12.6 ± 0.4 kcal/mol. The DCSs for elastic scattering (R2+R3) showed the expected forward bias with a monotonic decay in scattering intensity with angle. In contrast, the DCSs for inelastic scattering (R1) displayed slow, broad oscillations as a function of scattering angle whose phase and shape changed with collision energy. A comparison of the experimental results for DCSs for (R1) with scattering calculations reported here and in the accompanying paper[9] demonstrates that theory captures the most salient features of the experimental results: large, slow oscillations with respect to scattering angle and a remarkable sensitivity to collision energy. The theoretical calculations confirm that the oscillations result from interference between the quantum phases associated with at least two curve-crossing pathways.[9]

These calculations further show that the modulation depth and shape of these Stueckelberg oscillations depend strongly on the shape of the potential energy curves. This sensitivity possibly explains the lack of complete quantitative agreement between the experimental angular distributions and the theoretical DCSs. Notwithstanding, the overall similarity between experiment and theory presented here provides motivation for additional experiments and calculations to further investigate the quantum nature of O(^1D)→O(^3P) quenching by Xe.

Acknowledgements

The experimental work reported in this paper was supported by the Institute of Atomic and Molecular Sciences, Academia Sinica, Taiwan and the Liselotte and David Templeton endowed chair funds at the University of California, Berkeley. The theoretical work was supported by the National Science Foundation under Grant No. CHE-1213332. We thank Professor Kopin Liu for helpful discussions.

References

[1]J. R. Murray and C. K. Rhodes, J. Appl. Phys. **47**, 5041 (1976).
[2]M. C. Lin, M. E. Umstead, and N. Djeu, Annu. Rev. Phys. Chem. **34**, 557 (1983).
[3]K. Schofield, J. Photochem. **9**, 55 (1978).
[4]S. R. Kinnersly, J. N. Murrell, and W. R. Rodwell, J. Chem. Soc., Faraday Trans. 2 **74**, 600 (1978).
[5]S. R. Langhoff, J. Chem. Phys. **73**, 2379 (1980).
[6]T. H. Dunning and P. J. Hay, J. Chem. Phys. **66**, 3767 (1977).
[7]J. A. Davidson, H. I. Schiff, T. J. Brown, G. E. Streit, and C. J. Howard, J.Chem. Phys. **69**, 1213 (1978).
[8]Y. Matsumi, Y. Inagaki, G. P. Morley, and M. Kawasaki, J. Chem. Phys.**100**, 315 (1994).
[9]P. J. Dagdigian, J. Klos, and M. H. Alexander, "Theoretical investigation of the dynamics of O O($^1D \rightarrow {}^3P$) electronic quenching by collision with Xe," J. Chem. Phys. **143,** 54306 (2015).
[10]J. J. Lin, D. W. Hwang, S. Harich, Y. T. Lee, and X. M. Yang, Rev.Sci. Instrum. **69**, 1642 (1998).
[11] A. L. Van Wyngarden, et al., J. Chem. Phys. **141** (2014).
[12] K. A. Mar, A. L. Van Wyngarden, C.-W. Liang, Y. T. Lee, J. J. Lin, and K. A. Boering, J. Chem. Phys. **137** (2012).
[13]A. L. Van Wyngarden, K. A. Mar, K. A. Boering, J. J. Lin, Y. T. Lee, S.-Y. Lin, H. Guo, and G. Lendvay, J. Am. Chem. Soc. **129**, 2866 (2007).
[14]M. J. Perri, A. L. Van Wyngarden, J. J. Lin, Y. T. Lee, and K. A. Boering, J. Phys. Chem. A **108**, 7995 (2004).
[15]M. J. Perri, A. L. Van Wyngarden, K. A. Boering, J. J. Lin, and Y. T. Lee, J.Chem. Phys. **119**, 8213 (2003).
[16]J. J. Lin, D. W. Hwang, Y. T. Lee, and X. M. Yang, J. Chem. Phys. **109**, 1758 (1998).
[17]N. Balakrishnan, M. J. Jamieson, A. Dalgarno, Y. Li, and R. J. Buenker, J. Chem. Phys. **112**, 1255 (2000).
[18]M. Berglund and M. E. Wieser, Pure Appl. Chem. **83**, 397 (2011).
[19]G. L. Catchen, J. Husain, and R. N. Zare, J.Chem. Phys. **69**, 1737 (1978).
[20]J. C. Shi and J. R. Barker, Int. J. Chem. Kinet. **22**, 1283 (1990).
[21]See supplementary materials for plots of the TOF spectra of the O and Xe atoms.
[22]E. C. G. Stueckelberg, Helv. Phys. Acta **5**, 369 (1932).
[23]G. M. Carter, D. E. Pritchard, M. Kaplan, and T. W. Ducas, Phys. Rev. Lett. **35**, 1144 (1975).
[24]R. Duren, W. Groger, E. Hasselbrink, and R. Liedtke, J. Chem. Phys. **74**, 6806 (1981).
[25]J. P. Visticot, et al., Phys. Rev. A **45**, 6371 (1992).
[26]M. Hoshino, et al., Phys. Rev. A **75** (2007).
[27]N. Stolterfoht, R. Cabrera-Trujillo, P. S. Krstic, Y. Oehrn, E. Deumens, and J. R. Sabin, Int. J. Quantum Chem. **109**, 3063 (2009).
[28]T. Young, Phil. Trans. R. Soc. Lond. **94**, 1 (1804).
[29]T. Young, *A course of lectures on natural philosophy and the mechanical arts* (J. Johnson, London, 1807).
[30]S.-M. Wu, D. Chestakov, G. C. Groenenboom, W. J. van der Zande, D. H. Parker, G. Wu, X. Yang, and C. Vallance, Mol. Phys. **108**, 1145 (2010).

Supplementary materials

Additional Time of Flight Spectra

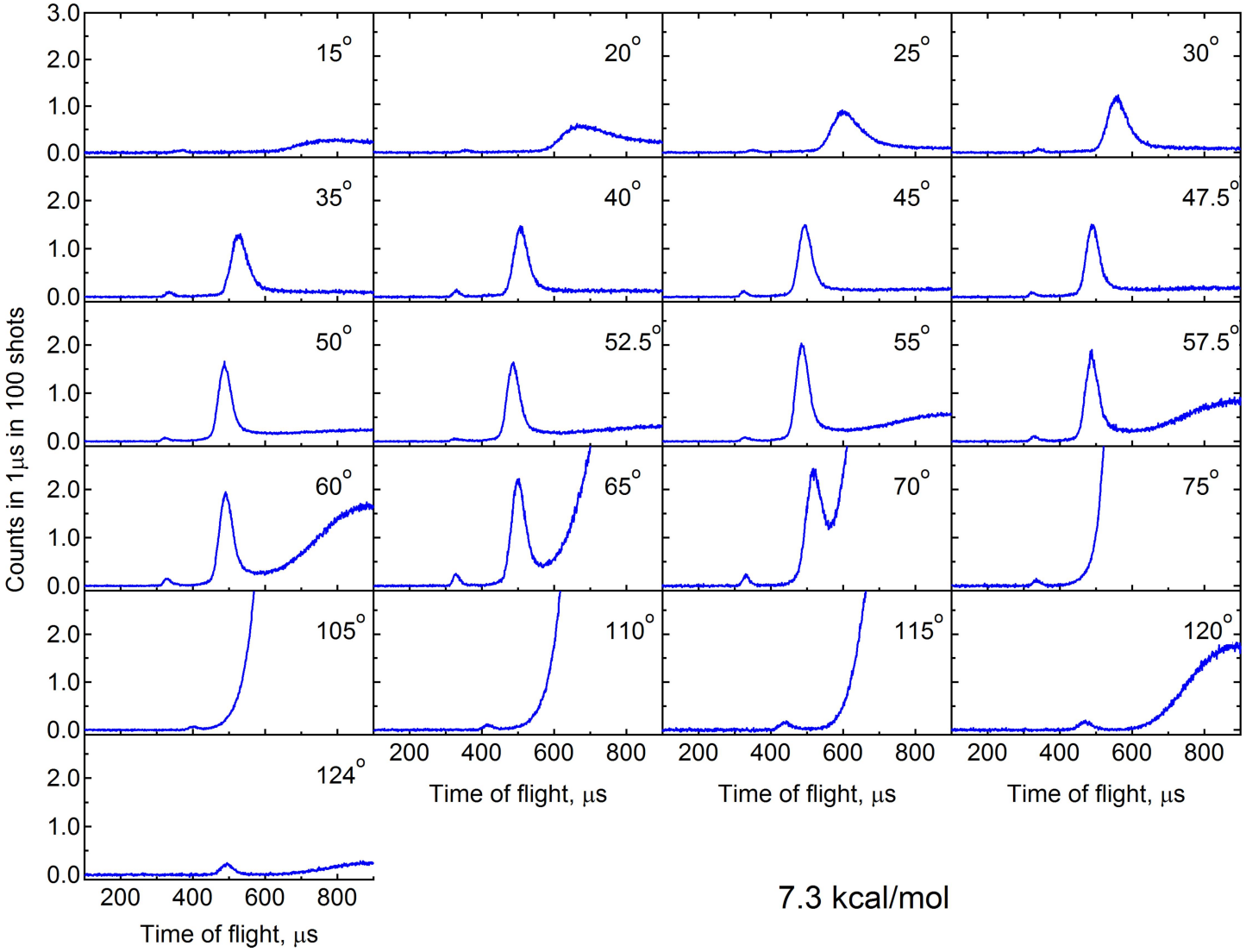

FIG. 4.S1 The baseline-subtracted, time-of-flight spectra for scattered Xe atoms at collision energy of 7.3 kcal/mol.

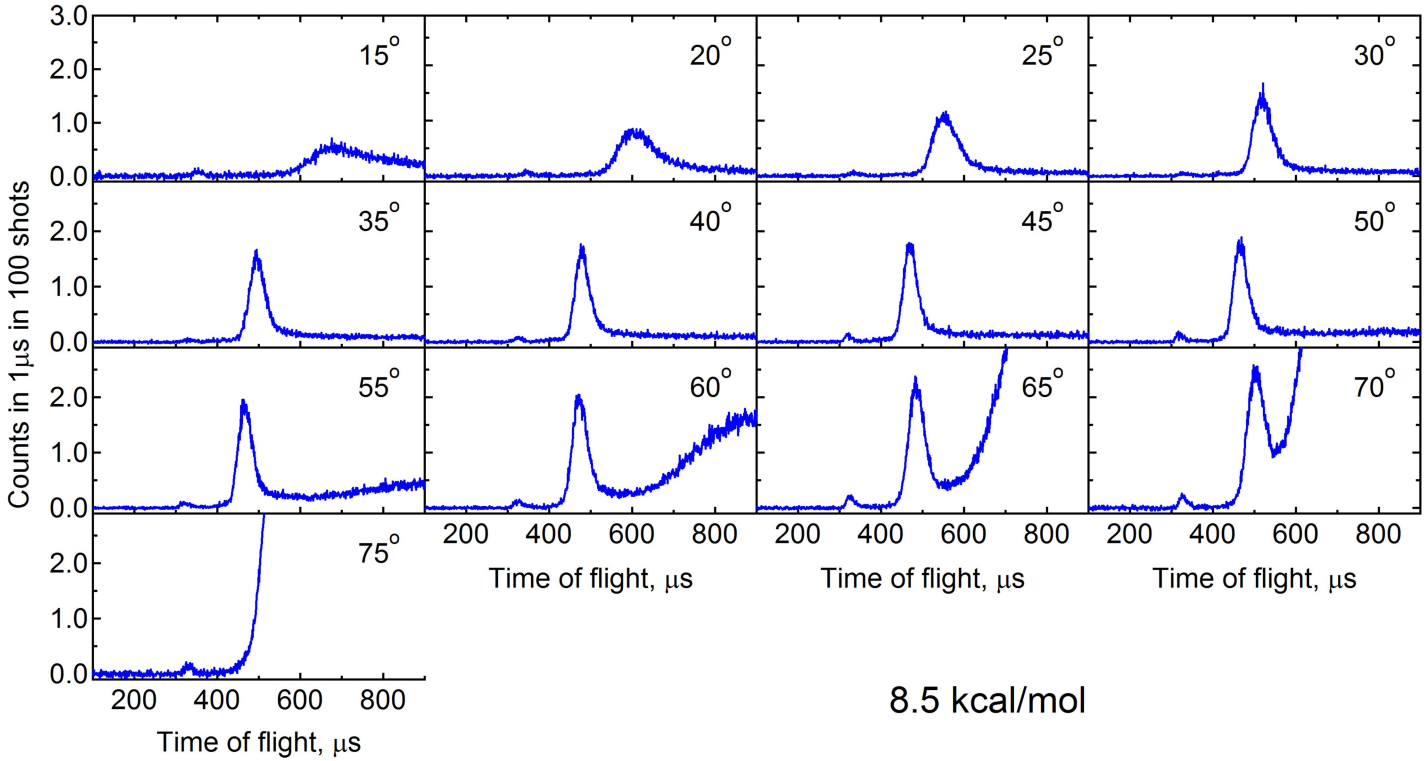

FIG. 4.S2 The baseline-subtracted, time-of-flight spectra for scattered Xe atoms at collision energy of 8.5 kcal/mol.

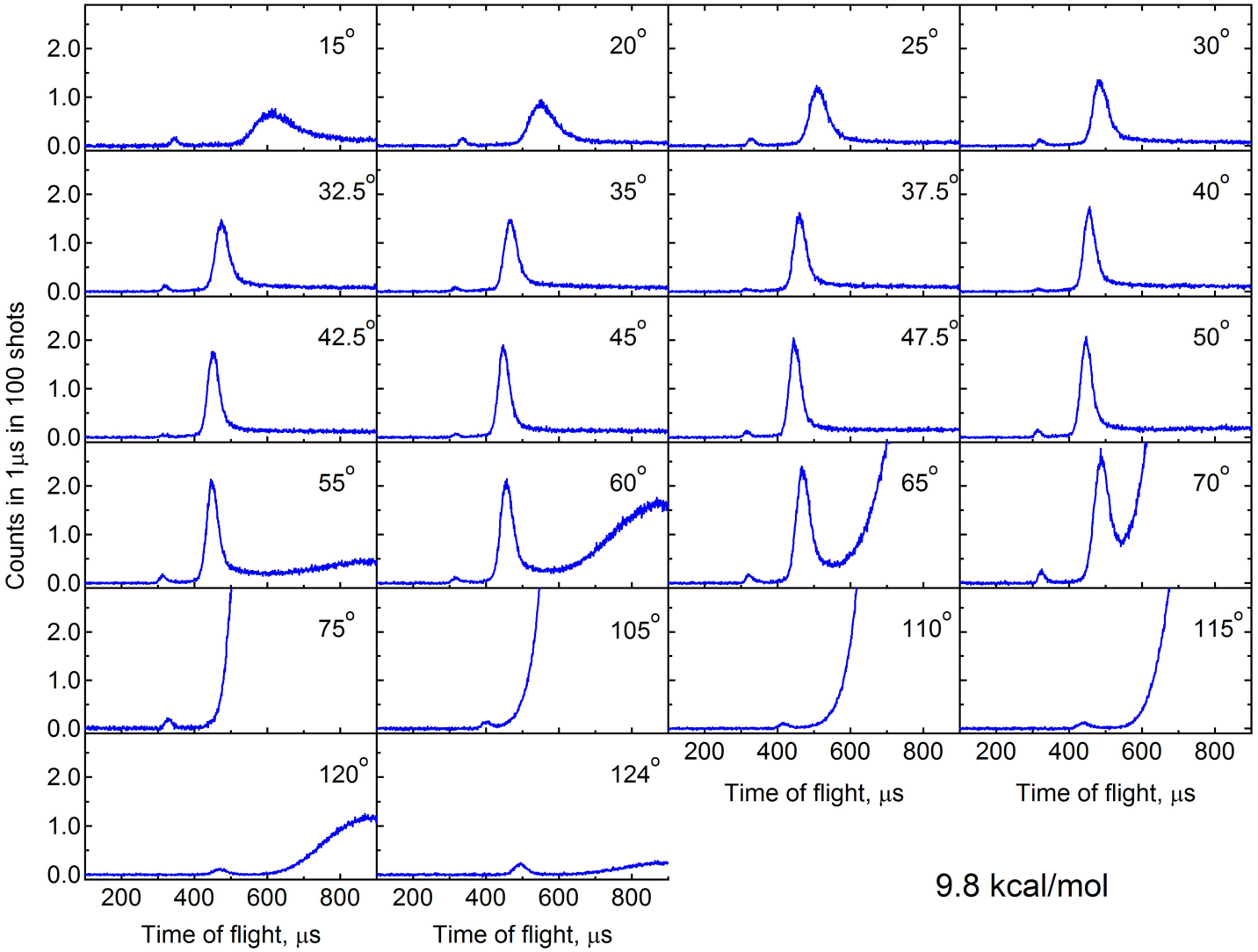

FIG. 4.S3 The baseline-subtracted, time-of-flight spectra for scattered Xe atoms at collision energy of 9.8 kcal/mol.

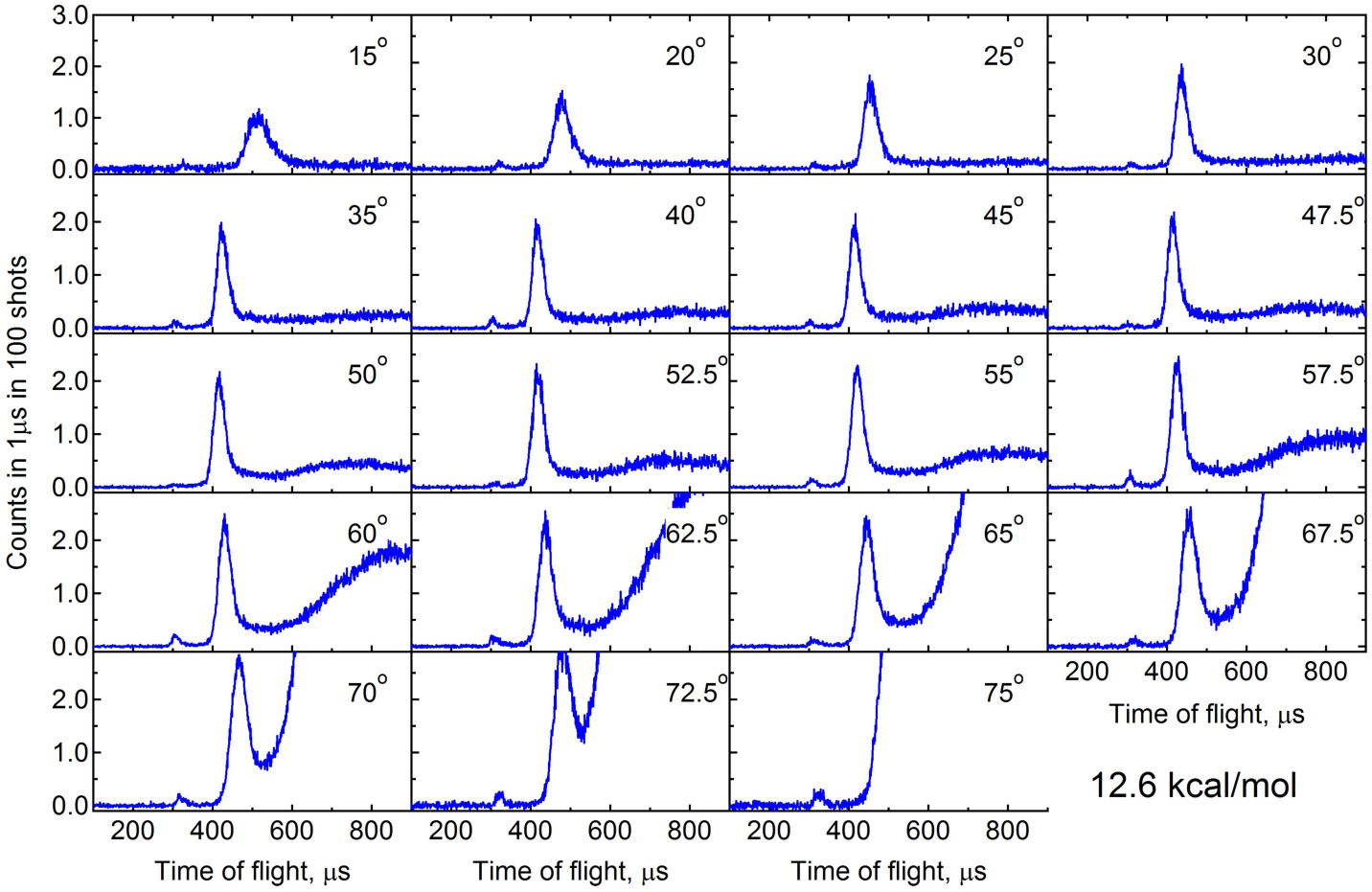

FIG. 4.S4 The baseline-subtracted, time-of-flight spectra for scattered Xe atoms at collision energy of 12.6 kcal/mol.

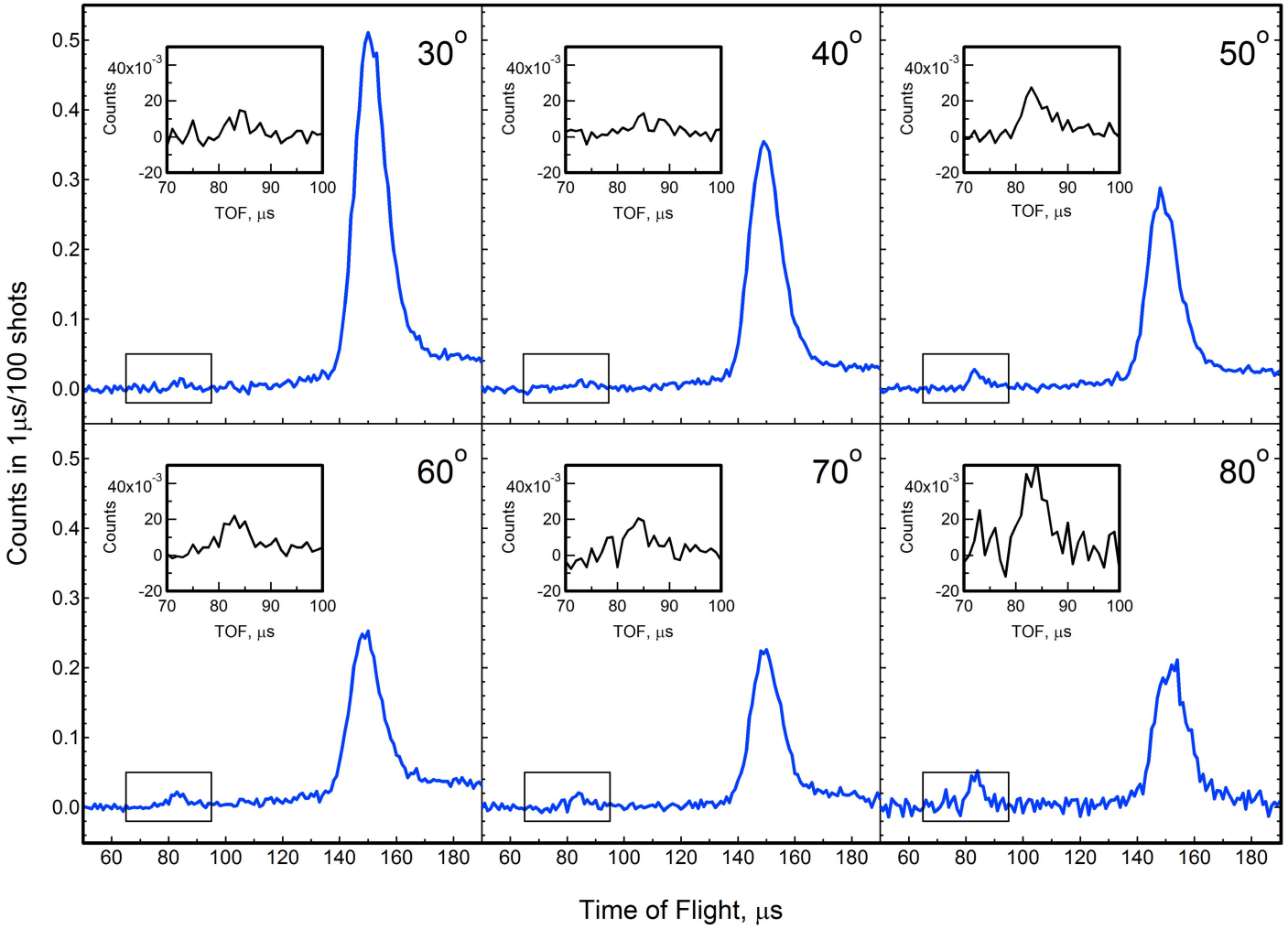

FIG. 4.S5 The baseline-subtracted, time-of-flight spectra for scattered O atoms at collision energy of 7.3 kcal/mol. [Similar to Figure 4.3]

Additional Integrated Peak Intensities in Laboratory and Center-of-Mass Frames

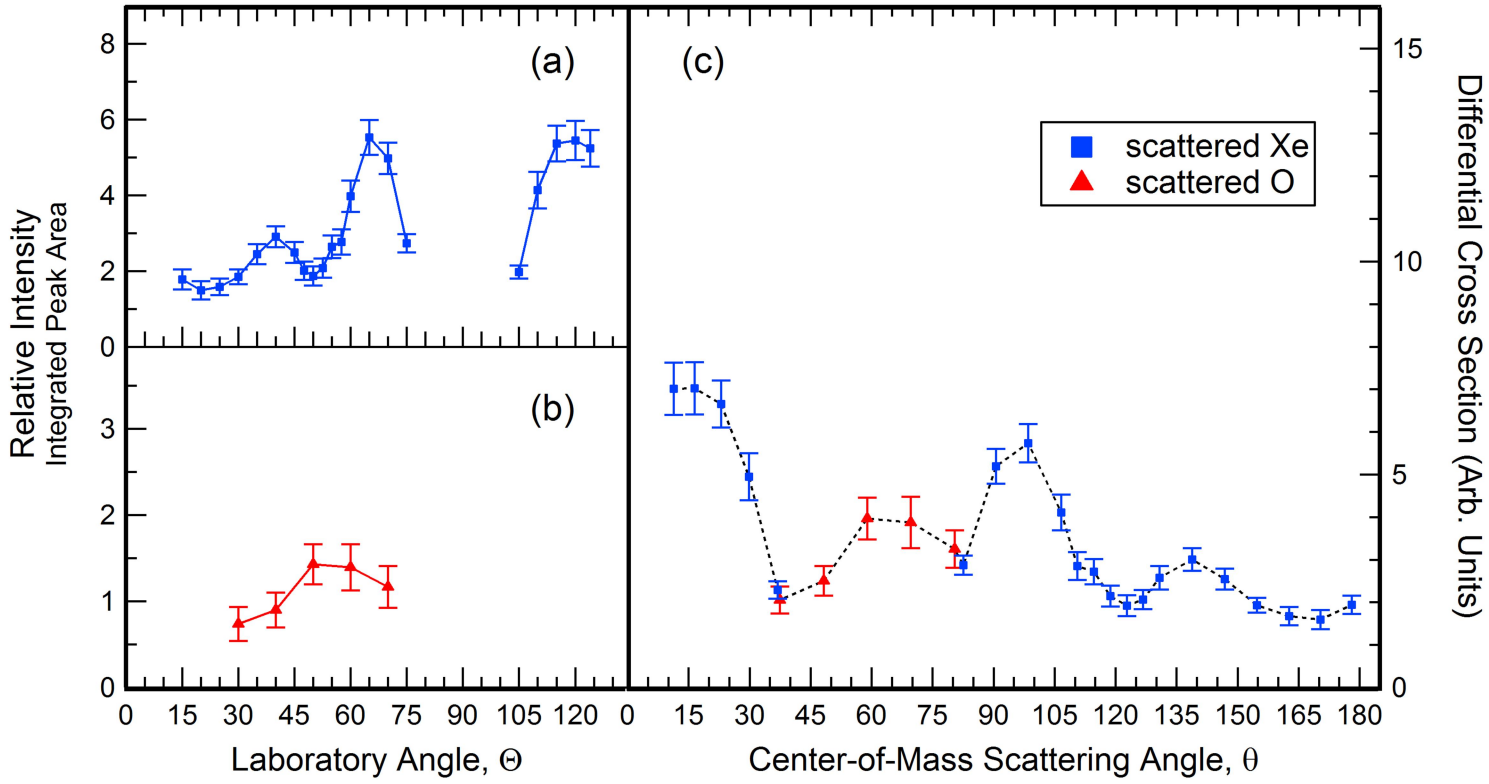

FIG. 4.S6 Same as Figure 4.6 for collision energy of 7.3 kcal/mol